UNIVERSITY OF MODENA AND REGGIO EMILIA

Department of Engineering “Enzo Ferrari”
PhD course in Industrial and Environmental Engineering

PhD Cycle XXXVI

Mechanics of membrane structures in nonlinear elasticity

Candidate: Stefano Sirotti

Tutor: Prof. Angelo Marcello Tarantino

Co-tutor: Prof. Bruno Briseghella

PhD School Coordinator: Prof. Alberto Muscio

Abstract

Elastic membranes find numerous applications in several technological fields. These structures are typically made of elastomers, due to their capability to withstand large elastic deformations. A consistent analysis of the mechanics of membranes must necessarily consider geometrical and material nonlinearities. Due to the resulting mathematical complexity, membrane problems are usually studied with numerical approaches and simple incompressible material models. This thesis investigates deeply the mechanics of elastic membranes to fill the lack of reliable analytical solutions and refined material models involving material compressibility.

Firstly, a simplified model to derive the analytical response of inflated circular flat membranes is proposed. Spherical deformed configurations are assumed as simplifying assumption. The membrane is regarded as a homogeneous, isotropic, hyperelastic solid described by a compressible Mooney-Rivlin constitutive law. The equilibrium at the pole of the membrane gives the analytical relation between the pressure and the deflection of the pole. Being approximate, this solution lacks of accuracy at very large deformations. A corrective function based on the numerical solution of the problem is calibrated, leading to a closed-form formula valid regardless of geometry, material parameters and range of deformation.

Subsequently, the formulation is extended to pre-stretched circular flat membranes and it is validated by means of finite element simulations. Bulge tests are performed on three elastomeric membranes, both unstretched and pre-stretched, and the proposed formulas are used to identify the material parameters. At very large deformations the compressible Mooney-Rivlin model suffers major limitations, especially regarding material hardening and volume changes. Therefore, an accurate strain energy function (SED) for the response of elastomers at very large deformations is proposed. In particular, the volumetric part of the SED is calibrated on experimental tests reflecting the real volumetric response of the material.

Finally, the proposed SED is applied to study the effect of compressibility in three benchmark membrane problems: inflation of a circular flat membrane, inflation of a thin-walled cylindrical tube, and inflation of a thin-walled spherical balloon. Four different materials with increasing degree of compressibility are considered. As compressibility increases, significant differences are observed in the pressure curve as well as in the deformed shapes.

On one hand, the models proposed in this thesis provide a reliable and ready-to-use analytical tool for practical applications of inflated membranes. On the other hand, the proposed solutions for compressible materials lay the foundation for applications of membranes made of innovative materials as foams, gels, metamaterials, which exhibit significant compressibility even at small deformations.

Sommario

Le membrane elastiche trovano numerose applicazioni in vari ambiti tecnologici. Queste strutture sono tipicamente realizzate in materiali elastomerici, grazie alla loro capacità di sostenere grandi deformazioni elastiche. Un'adeguata analisi della meccanica delle membrane deve necessariamente considerare le non linearità geometriche e materiali. A causa della complessità matematica, i problemi riguardanti le membrane sono solitamente studiati con approcci numerici e assumendo semplici modelli di materiale incomprimibile. Questa tesi studia approfonditamente la meccanica delle membrane elastiche per colmare la mancanza di affidabili soluzioni analitiche e di accurati modelli materiali che considerino la comprimibilità.

Innanzitutto viene proposto un modello semplificato per ottenere la risposta analitica di membrane piane circolari soggette a pressione laterale. Come ipotesi semplificativa, la configurazione deformata viene assunta sferica. La membrana è considerata come un solido omogeneo, isotropo e iperelastico descritto da un legame Mooney-Rivlin comprimibile. L'equilibrio al polo della membrana fornisce la relazione analitica tra la pressione e lo spostamento del polo stesso. Essendo approssimata, questa soluzione perde accuratezza in grandi deformazioni. Perciò viene calibrata una funzione correttiva basata sulla soluzione numerica del problema, ottenendo una formula chiusa e valida indipendentemente dalla geometria, dai valori dei parametri del materiale e dal livello di deformazione.

Successivamente, la formulazione è estesa alle membrane circolari piane dotate di pre-stretch ed è validata attraverso simulazioni agli elementi finiti. Dei bulge test sono condotti su tre membrane elastomeriche, sia senza che con pre-stretch, e le formule proposte sono utilizzate per determinare i parametri dei materiali. A deformazioni molto elevate il modello di Mooney-Rivlin comprimibile riscontra importanti limiti, specialmente dovuti all'hardening del materiale e alle variazioni di volume. Perciò viene proposta un'energia di deformazione accurata per la risposta di elastomeri in grandi deformazioni. In particolare, la parte volumetrica dell'energia è calibrata sulla base di prove sperimentali e riflette la reale risposta volumetrica del materiale.

Infine, la forma di energia proposta è usata per studiare l'effetto della comprimibilità in tre problemi di riferimento: una membrana circolare soggetta a pressione laterale, un tubo cilindrico a parete sottile in pressione, e una sfera a parete sottile in pressione. Vengono considerati quattro differenti materiali con grado di comprimibilità crescente. Al crescere della comprimibilità, si osservano differenze significative sia nella curva della pressione sia nelle deformate.

Da un lato, i modelli proposti forniscono uno strumento analitico affidabile e di immediato utilizzo per le applicazioni pratiche. Dall'altro, le soluzioni proposte per materiali comprimibili gettano le basi per applicazioni di membrane realizzate in materiali innovativi come schiume, gel e metamateriali, i quali mostrano una comprimibilità significativa anche a piccole deformazioni.

Contents

List of Figures

List of Tables

Dedicated to Mauro and Raffaella

"La cosa più bella che noi possiamo provare è il senso del mistero: esso è la sorgente di tutta l'arte e di tutta la scienza"

Albert Einstein

1 Introduction

Inflatable elastic membranes find applications across various fields of engineering, due to their unique combination of flexibility, durability, and adaptability. In architecture, these membranes are utilized for temporary structures, such as event pavilions and exhibition spaces, as well as for permanent installations like retractable roofs and pneumatic structures. In the field of robotics, inflatable membranes serve as actuators for soft robots, providing compliant and versatile motion capabilities ideal for applications in healthcare, exploration, and human-robot interaction. Additionally, elastic membranes play a crucial role in biomedical devices, where they are employed in tissue engineering scaffolds, drug delivery systems, and wearable medical devices. Moreover, these membranes are utilized in aerospace for deployable structures and airbags and in automotive engineering for impact mitigation systems and inflatable seals. The versatility and reliability of inflatable elastic membranes continue to drive innovation and enable advancements across a wide range of industries, demonstrating their indispensable role in modern technology and design.

Since membranes are designed to sustain large deformations, geometrical and mechanical nonlinearities must be necessarily taken into account. The arising mathematical complexity does not allow to obtain closed-form solutions even to problems of simple geometry. For this reason, problems involving inflatable membranes have typically been approached numerically. Early works by Treloar [1], Adkins and Rivlin [2], Green and Adkins [3], Corneliussen et al. [4] provided the foundation of the theory of elastic membranes. Successively, numerical approaches have been employed to address increasingly complex problems of inflated membranes, but analytical solutions remain scarce. However, analytical solutions are of significant relevance in both advancing the understanding and developing applications of elastic membranes across various fields. Unlike numerical simulations, which can be computationally intensive and time-consuming, analytical solutions offer an efficient and accessible means of analyzing the response of membrane structures under different conditions. This is helpful in the design and optimization of inflatable structures, enabling engineers and researchers to explore a wide range of design parameters and material properties. Furthermore, analytical solutions serve as valuable tools for gaining insights into the underlying mechanics of inflated membranes, aiding in the development of more accurate mathematical models.

In addition, the high nonlinearities and the large strains involved in the response of elastic membranes make the choice of accurate nonlinear models crucial to provide reliable predictions of the behavior of these structures. However, most problems involving inflatable elastic membranes have been studied assuming simple hyperelastic models. In particular, the analyses of elastic membranes have usually been developed under the assumption of material incompressibility, due to the consideration that the bulk modulus of elastomers is much larger than their shear modulus. However, on one hand it has already been demonstrated that some class of elas-

tomers can experience significant volume changes at large deformations [5, 6]. On the other hand, membranes made of soft materials like foams and gels find increasing applications in modern technologies [7, 8]. These materials are characterized by large volume changes even at small strains, and their modeling requires material compressibility to be taken into account.

This thesis aims to bridge these gaps by investigating deeply the mechanics of elastic membranes, with a specific focus on developing reliable analytical solutions and refined material models that incorporate compressibility. In the first part of the thesis, an analytical solution to the problem of the inflation of a circular membrane described by a Mooney-Rivlin model is proposed. The proposed solution relies on a simplified model based on the assumption of spherical deformed configurations. At large deformations, the simplified model loses accuracy and the proposed solution is adjusted by a refined polynomial function calibrated on the numerical solution of the problem. As a result, the adjusted solution accurately predicts the pressure vs. deflection curve of circular membranes regardless of geometrical parameters, material parameters and magnitude of deformation. The proposed solution is then extended to the case of initially pre-stretched circular membranes and validated by finite element simulations. Comparison with simplified analytical models from the literature proves the wide range of validity of the proposed formulas. Experimental bulge tests on both unstretched and pre-stretched membranes are carried out, and the proposed formula is used as an efficient and accessible tool to the characterization of material parameters.

Successively, an accurate strain energy function (SED) is proposed to overcome the limitations exhibited by the Mooney-Rivlin model. Particular attention is given to material compressibility. Experimental simple tension and bulk tests are carried out on four different types of elastomers. The complete volumetric curve is derived by means of digital image correlation techniques, showing that some kind of elastomers experience significative volume changes when the deformations are large. Following the split of the energy into the deviatoric and volumetric parts, a volumetric SED is then proposed. The proposed function is specifically designed for elastomers and overcomes the limitations of the current formulations available in the literature. The Yeoh-Fleming model is selected among the most commons incompressible models and assumed as deviatoric part of the proposed SED.

The proposed SED is then adopted to study the effect of compressibility on the mechanical response of inflated membranes. To this purpose, four classes of materials with increasing degree of compressibility are investigated, involving foams, gels and auxetic foams. Three benchmark membrane problems are examinated, including circular flat membrane inflation, thin-walled cylindrical tube inflation, and thin-walled spherical balloon inflation. The observed differences in pressure curves and deformed shapes underscore the significant impact of compressibility on the response of membranes.

In summary, this thesis contributes a two-fold advancement to the field: firstly, by offering reliable analytical tools for practical applications of inflated circular membranes, and secondly, by proposing a refined strain energy function for the large deformations of compressible materials, laying the groundwork for the exploration of

membranes composed of advanced materials exhibiting significant compressibility, such as foams, gels, and metamaterials.

The thesis is organized as follows. In Chapter 2 the numerical solution to the benchmark problem of the inflation of a circular flat membrane is presented and discussed. In Chapter 3 the simplified model for inflated circular membranes is presented. The approximate analytical pressure curves are derived and refined on the basis of the numerical solution. The proposed solution is validated by finite element simulations and a comparison with other simplified models in literature is given. Experimental bulge tests are carried out and the proposed formula is used for the material characterization. The proposed solution is then extended to the case of initially stretched circular membranes in Chapter 4, and another series of bulge tests are carried out on pre-stretched membranes. In Chapter 5, an original volumetric strain energy function based on the real volumetric response of elastomers is developed and proposed. The proposed SED is adopted in Chapter 6 to investigate the effect of compressibility on the mechanics of membranes. Conclusions are drawn in Chapter 7.

2 Numerical solution for the inflation of circular membranes

The inflation of a circular, flat membrane is a benchmark problem in nonlinear elasticity. Despite the simple geometry, the high material and geometrical nonlinearities involved do not allow for closed-form solutions. Therefore, researchers typically resorted to numerical approaches to provide solution and further insights into this problem. In this chapter, the numerical solution for the inflation of a flat, circular membrane is presented. The membrane is made of an homogeneous, isotropic, hyperelastic material. Subjected to a uniform lateral pressure, the membrane inflates preserving axialsimmetry. The equilibrium equations of a material element in the radial and normal directions lead to the governing system of first order ordinary differential equations, which represents a two-point boundary value problem (TPBVP). The TPBVP is converted into an initial value problem and solved following the procedure proposed by Yang & Feng [9]. The procedure allows to solve the TPBVP without the need of repeated iterations, resulting in a significant computational convenience. In Section 2.4, the equations are specialized for an incompressible Mooney-Rivlin material model, and successively extended for the first time to consider material compressibility. The solution is reported in terms of pressure vs. deflection curve and deformed shapes, and two typical behaviours based on material parameters are discussed. The numerical solution presented in this chapter has a two-fold purpose: firstly, to illustrate the basic features of this problem, and secondly to serve as reference for the development of the analytical model in the following chapters.

2.1 Preliminaries

The problem of a circular flat membrane inflated by a uniform lateral pressure was first investigated in the pioneering works by Treloar [1], Adkins and Rivlin [2] and Green and Adkins [3]. Later on, the scientific interest towards this topic increased considerably, driven by the variety of its applications in different engineering fields. Thanks to their capability of sustaining large deformations, circular membranes made of elastomers are used for instance in soft robotics [10–12], dielectric systems [13–17], nano-devices [18, 19], biomechanics [20, 21] and structural engineering [22, 23].

When subjected to inflation, rubber membranes undergo large deformations. For this reason, material and geometrical nonlinearities must necessarily taken into account, leading to complex mechanical behaviours. Indeed, an exact closed-form solution to this problem does not exist, even for the simplest case of lineraly elastic material. Therefore, the problem has been investigated mostly from a numerical point of view. Initially, the problem was formulated in terms of eight equation in

eight unknowns. The numerical methods were based on changing the two-point boundary value problem into an initial value problem, according to the Cauchy-Kowalewski theorem [24]. The integration started from one boundary with part of boundary conditions given and part assumed. The conditions at the other boundary were met with a trial and error method. The breakthrough work by Yang and Feng [9] managed to greatly simplify the system of equations into three differential equations with explicit derivatives. In addition, Yang and Feng noticed an invariance property of the governing equations which allows to avoid the trial and error procedure. Successively, many authors adopted this approach to solve more complex problems. For instance, Liu et al. [25] and Patil et al. [26] studied the contact mechanics of inflated membranes under different interface conditions.

In the following, the benchmark problem of the inflation of a circular flat membrane is presented and the procedure proposed by Yang and Feng is used to solve the two-point boundary value problem. Besides providing insights on the main features of the mechanics of inflatable membranes, this numerical solution is assumed as reference solution for the development of the approximate analytical solution in the following chapters.

2.2 Kinematics and constitutive relations

A membrane is modelled as a two-dimensional body with thickness much smaller than the in-plane dimensions. As a consequence, the bending stiffness and the compressive stiffness of a membrane are negligible and it can only withstand tensile stresses. Consider a circular flat membrane of radius L and thickness H, represented in Fig. 2.1(a-b). In the reference configuration, a generic point P has coordinates (R, Θ, Z) with respect to a cylindrical coordinate system with origin in O. A uniform lateral pressure p is applied and the membrane is inflated into the deformed configuration. Here and in the rest of the work we assume axysimmetric deformations, ignoring more complex instability phenomena that trigger asymmetric deformed shapes. After the deformation, point P moves to point P' with coordinates (r, Θ, z). As shown in Fig.2.1(c), the principal directions of strain $(1, 2, 3)$ correspond to the meridians, the latitudinal lines and the normal to the deformed surface. The principal stretches read respectively [9]

$$\lambda_1 = \sqrt{r'^2 + z'^2}, \quad \lambda_2 = \frac{r}{R}, \quad \lambda_3 = \frac{h}{H}, \tag{2.1}$$

where h is the thickness of the membrane in the deformed configuration and the prime denotes differentiation with respect to the radial coordinate R. The principal curvatures in the meridian and circumferential direction are given by

$$K_1 = \frac{\lambda_1' r' - \lambda_1 r''}{\lambda_1^2 \sqrt{\lambda_1^2 - r'^2}}, \quad K_2 = \frac{\sqrt{\lambda_1^2 - r'^2}}{\lambda_1 \lambda_2 R}. \tag{2.2}$$

The membrane is made of a homogeneous, isotropic and hyperelastic material. In the framework of hyperelasticity, the mechanical properties of the material are described by the strain energy function W. Under the assumption of frame-indifference

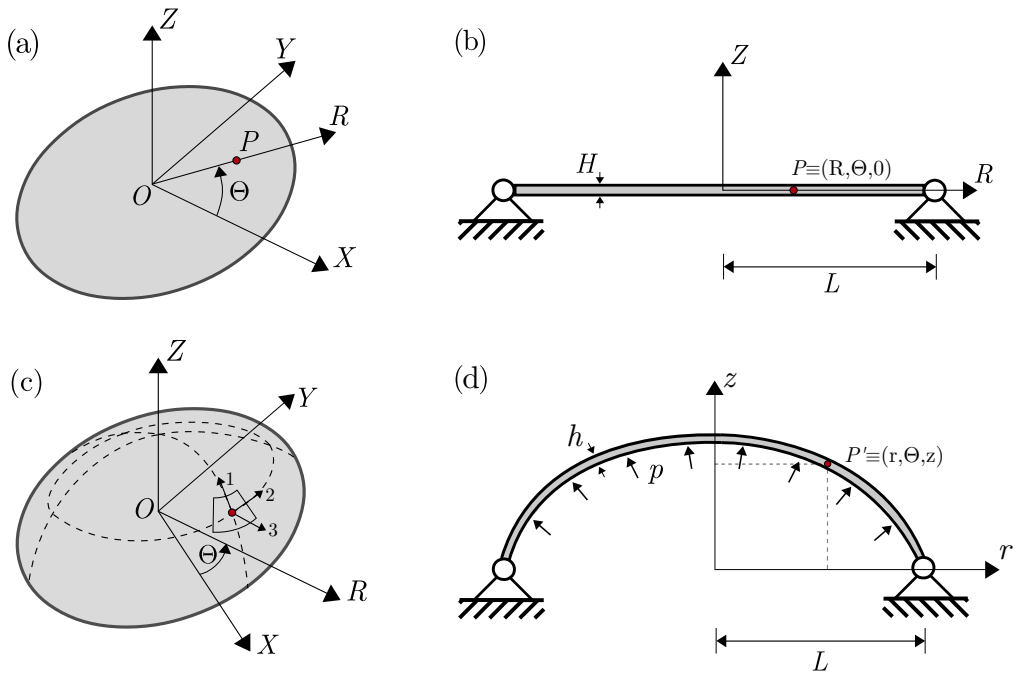

Figure 2.1: Circular flat membrane subjected to uniform lateral pressure p: (a) membrane in the reference configuration; (b) view in the R-Z plane; (c) membrane in the deformed configuration; (d) view in the r-z plane. The principal directions 1,2,3 coincide with the meridians, the latitudinal lines and normal to the deformed surface. A generic material point P with coordinates $(R, \Theta, 0)$ in a cylindrical reference frame moves to P', with coordinates (r, Θ, z). The deformation is axisymmetrical.

and isotropy, W can be written as a symmetric function of the principal strain invariants or the principal stretches [27], namely

$$W = W(I_1, I_2, I_3) = \tilde{W}(\lambda_1, \lambda_2, \lambda_3), \tag{2.3}$$

where I_1, I_2 and I_3 are the principal strain invariants defined as

$$\begin{aligned} I_1 &= \mathrm{tr}\mathbf{C} = \lambda_1^2 + \lambda_2^2 + \lambda_3^2, \\ I_2 &= \frac{1}{2}\left[(\mathrm{tr}\mathbf{C})^2 - \mathrm{tr}\left(\mathbf{C}^2\right)\right] = \lambda_1^2\lambda_2^2 + \lambda_1^2\lambda_3^2 + \lambda_2^2\lambda_3^2, \\ I_3 &= \det\mathbf{C} = \lambda_1^2\lambda_2^2\lambda_3^2, \end{aligned} \tag{2.4}$$

being $\mathbf{C} = \mathbf{F}^T\mathbf{F}$ the right Cauchy-Green deformation tensor and $\mathbf{F}$ the deformation gradient. In the following, the strain energy function is written as a function of the principal strain invariants, $W = W(I_1, I_2, I_3)$, since this is the case for most hyperelastic models in the literature. The derivatives with respect to the principal stretches can be computed with the chain rule and read

$$\frac{\partial W}{\partial \lambda_i} = 2\lambda_i\left(w_1 + \left(\lambda_j^2 + \lambda_k^2\right)w_2 + \lambda_j^2\lambda_k^2 w_3\right), \qquad i,j,k = 1,2,3 \tag{2.5}$$

where $w_j = \partial W/\partial I_j$, with $j = 1,2,3$. The principal Cauchy stresses are given by

$$\sigma_i = \frac{1}{\lambda_j \lambda_k} \frac{\partial W}{\partial \lambda_i}, \quad i,j,k = 1,2,3. \tag{2.6}$$

Material incompressibility is a common assumption in the study of elastomers. This is based on the observation that their bulk modulus is much larger than their shear modulus. Under the assumption of incompressibility, the material can not experience volume changes during deformation, namely every deformation is isochoric. The mathematical constraint $J = \det \mathbf{F} = \lambda_1 \lambda_2 \lambda_3 = 1$ determines the expression for the transversal stretch

$$\lambda_3 = \frac{1}{\lambda_1 \lambda_2}. \tag{2.7}$$

The strain energy function depends on I_1 and I_2 only, $W = W(I_1, I_2)$, and the derivatives with respect to the principal stretches reduce to

$$\partial W/\partial \lambda_i = 2\lambda_i \left(w_1 + \left(\lambda_j^2 + \lambda_k^2 \right) w_2 \right), \quad i,j,k = 1,2,3. \tag{2.8}$$

The principal Cauchy stresses are given by

$$\sigma_i = \lambda_i \frac{\partial W}{\partial \lambda_i} - p, \quad i,j,k = 1,2,3. \tag{2.9}$$

where p is the internal pressure associated with the incompressibility constraint.

A thourough discussion and investigation on the compressibility of elastomers is carried out in Chapter 5. In the following section, as always done in the literature, the numerical solution of the problem is presented assuming incompressibility. In Section 2.4 the governing equations are specialised to the Mooney-Rivlin material model and extended to the case of compressible Mooney-Rivlin material. The governing equations in case of a generic compressible material are introduced in Chapter 6.

2.3 Boundary value problem and numerical integration

Being the thickness much smaller than the in-plane dimensions, it is reasonable to assume that the normal stress along the thickness is negligible, resulting in a plane stress condition. From this condition, $\sigma_3 = 0$, the internal pressure p in Eq.(2.9) can be determined. The principal stress resultants for unit edge length of the membrane are given by

$$T_i = \sigma_i h = 2H \left(\frac{\lambda_i}{\lambda_j} - \frac{1}{\lambda_i^3 \lambda_j^3} \right) \left(w_1 + \lambda_j^2 w_2 \right), \quad i,j = 1,2. \tag{2.10}$$

The equilibrium equations in the meridian and normal directions read

$$\frac{dT_1}{dr} + \frac{1}{r}(T_1 - T_2) = 0, \tag{2.11}$$

$$K_1 T_1 + K_2 T_2 = p. \tag{2.12}$$

Susbstituting Eq.(2.10) and Eq.(2.2) into the equilibrium equations, and with the position $\eta = r'$, the following system of differential equations is obtained:

$$\begin{aligned}
\lambda_1' &= \frac{w_1\psi_1 + w_2\psi_2 + \frac{\partial w_1}{\partial \lambda_2}\psi_3 + \frac{\partial w_2}{\partial \lambda_2}\psi_4}{R\lambda_2\left(3w_1 - \frac{\partial w_1}{\partial \lambda_1}\lambda_1 + \left(3w_2 - \frac{\partial w_2}{\partial \lambda_1}\lambda_1 + \lambda_1^4\left(w_1 + \frac{\partial w_1}{\partial \lambda_1}\lambda_1\right)\right)\lambda_2^2 + \lambda_1^4\left(w_2 + \frac{\partial w_2}{\partial \lambda_1}\lambda_1\right)\lambda_2^4\right)}, \\
\lambda_2' &= \frac{\eta - \lambda_2}{R}, \\
\eta' &= \frac{\eta\lambda_1'}{\lambda_1} - \frac{\phi\lambda_1^5\lambda_2^4\sqrt{-\eta^2 + \lambda_1^2} + 2\lambda_1\left(\eta^2 - \lambda_1^2\right)\left(w_1 + w_2\lambda_1^2\right)\left(\lambda_1^2\lambda_2^4 - 1\right)}{2R\lambda_1\lambda_2\left(w_1 + w_2\lambda_2^2\right)\left(\lambda_1^4\lambda_2^2 - 1\right)},
\end{aligned} \tag{2.13}$$

where $\phi = pR/H$ and, for the sake of clarity, the following quantities were defined:

$$\begin{aligned}
\psi_1 &= \eta\lambda_2^4\lambda_1^3 - 3\eta\lambda_1 - \lambda_2^3\lambda_1^5 + 3\lambda_2\lambda_1, \\
\psi_2 &= -\eta\lambda_2^4\lambda_1^5 - \eta\lambda_1^3 + \lambda_2^5\lambda_1^5 + \lambda_2^3\lambda_1, \\
\psi_3 &= -\eta\lambda_2^3\lambda_1^5 + \eta\lambda_2\lambda_1 + \lambda_2^4\lambda_1^5 - \lambda_2^2\lambda_1, \\
\psi_4 &= -\eta\lambda_1^5\lambda_2^5 + \eta\lambda_1\lambda_2^3 + \lambda_1^5\lambda_2^6 - \lambda_1\lambda_2^4.
\end{aligned} \tag{2.14}$$

Eqs.(2.13) compose a system of three nonlinear first order ordinary differential equations in the indipendent variables λ_1, λ_2 and η. These governing equations specify a two-point boundary value problem (TPBVP), since boundary conditions for the indipendent variables are prescribed at both boundaries of the domain. At the pole, the principal stretches λ_1 and λ_2 are equal by symmetry and $z' = 0$. Thus we have

$$\lambda_1 = \lambda_2 = \eta = \lambda_0 \quad \text{at} \quad R = 0, \tag{2.15}$$

with $\lambda_0 > 1$. At the outer boundary the membrane is fixed, namely

$$\lambda_2 = 1 \quad \text{at} \quad R = L/2. \tag{2.16}$$

The integration of a TPBVP requires iterative procedures, fixing an initial condition λ_0 and integrating the equation with different values for the pressure p until the condition at the outer boundary is met. However, Yang & Feng [9] noticed that system (2.13) remains unchanged when a generic scaling factor γ is multiplied to R. This invariance property greatly simplifies the integration, avoiding iterations. Ultimately, the integration reduces to the following steps:

1. set an initial condition λ_0 at the pole;
2. guess a value p_0 for the pressure;
3. integrate system (2.13) using a Runge-Kutta method for increasing values of R, until $\lambda_2 = 1$;
4. the value of R at which $\lambda_2 = 1$ is denoted by R^* and it will generally differ from L, since the guessed value p_0 for the pressure is not likely to be corrected. However, now the invariance property of system (2.13) allows to define a scaling factor $\gamma = L/R^*$. The correct pressure p, which satisfies the equilibrum equations and the boundary conditions, is given by

$$p = p_0 L/\gamma a H. \tag{2.17}$$

5. integrate again system (2.13) with the correct pressure p to obtain the stretches profiles. The deformed coordinates, r and z, are determined using Eq.(2.1).

6. repeat the procedure for different initial conditions λ_0 to determine the corresponding pressures and stretches profiles.

In case of an initial homogeneous pre-stretch $\bar{\lambda}$, before inflation the membrane is already deformed and the principal stretches are equal to $\lambda_1 = \lambda_2 = \bar{\lambda}$. For this reason, the outer boundary condition during inflation reads

$$\lambda_2 = \bar{\lambda} \quad \text{at} \quad R = L/2. \tag{2.18}$$

Other than that, there are no difference between the unstretched and pre-stretched case and the numerical integration follows the steps listed above.

2.4 Application to Mooney-Rivlin materials

In this section, the governing equations presented above are specialised to a membrane made of a Mooney-Rivlin material. The Mooney-Rivlin model is one of the most common strain energy functions adopted to model elastomers in hyperelasticity, since it combines a mathematical simplicity with a good ability in reproducing the main features of the response of elastomers under large deformations. In the following, the cases of both incompressible and compressible material are considered.

2.4.1 Incompressible materials

An incompressible Mooney-Rivlin material is described by the strain energy function [28, 29]

$$W(I_1, I_2) = a(I_1 - 3) + b(I_2 - 3), \tag{2.19}$$

where a and b are material parameters. The derivatives with respect to I_1, I_2 read

$$w_1 = a, \quad w_2 = b. \tag{2.20}$$

Defining the ratio $\beta = b/a$, the principal stress resultants specialise to

$$\begin{aligned} T_1 &= 2aH\left(1+\beta\lambda_2^2\right)\left(\frac{\lambda_1}{\lambda_2} - \frac{1}{\lambda_1^3\lambda_2^3}\right), \\ T_2 &= 2aH\left(1+\beta\lambda_1^2\right)\left(\frac{\lambda_2}{\lambda_1} - \frac{1}{\lambda_1^3\lambda_2^3}\right), \end{aligned} \tag{2.21}$$

which substituted in Eqs.(2.11), (2.12) give the governing system of differential equations

$$\begin{aligned} \lambda_1' &= \frac{\lambda_1\left[3\lambda_2 + \lambda_2^3\left(\beta - \lambda_1^4\right) + \lambda_2^4\lambda_1^2\eta\left(1-\beta\lambda_1^2\right) + \beta\lambda_2^5\lambda_1^4 - \eta\left(\beta\lambda_1^2+3\right)\right]}{R\lambda_2\left(\beta\lambda_2^2+1\right)\left(\lambda_2^2\lambda_1^4+3\right)}, \\ \lambda_2' &= \frac{\eta - \lambda_2}{R}, \\ \eta' &= \frac{\eta\lambda_1'}{\lambda_1} - \frac{\phi\lambda_2^3\lambda_1^4\sqrt{\lambda_1^2-\eta^2}}{2R\left(\beta\lambda_2^2+1\right)\left(\lambda_2^2\lambda_1^4-1\right)} + \frac{\left(\beta\lambda_1^2+1\right)\left(\lambda_2^4\lambda_1^2-1\right)\left(\lambda_1^2-\eta^2\right)}{R\lambda_2\left(\beta\lambda_2^2+1\right)\left(\lambda_2^2\lambda_1^4-1\right)}, \end{aligned} \tag{2.22}$$

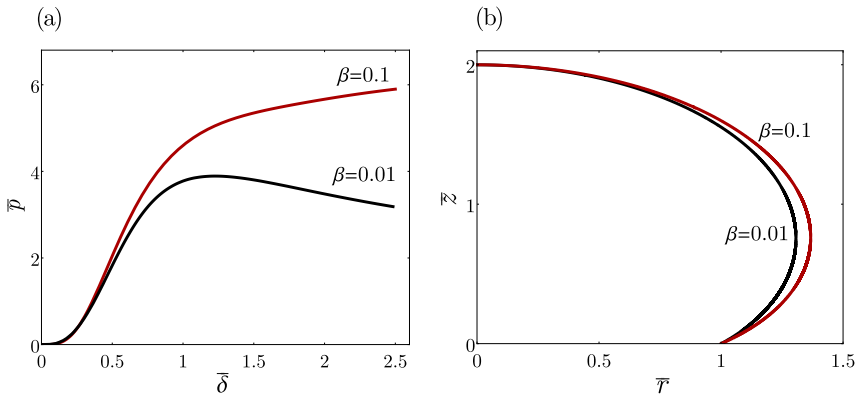

Figure 2.2: Inflation of an incompressible Mooney-Rivlin circular membrane: (a) normalized pressure $\bar{p} = pL/(aH)$ vs. normalized deflection of the pole $\bar{\delta} = \delta/L$ and (b) normalized deformed shape ($\bar{r} = r/L$, $\bar{z} = z/L$) corresponding to $\bar{\delta} = 2$.

with $\phi = pR/aH$. The numerical integration of system (2.22) is perfomed on MATLAB using function *ode23* with an integration step $\Delta R = 0.001$. It is important to note that the governing equations depend only on the ratio β. Therefore, β is the only parameter which affects qualitatively the response of the membrane, whereas a variation of a only implies a scaling in the pressure. This makes the study of the influence of material properties on the membrane response particularly convenient in the case of a Mooney-Rivlin material. Figure 2.2(a) shows the response of a Mooney-Rivlin membrane with $\beta = 0.01$ and $\beta = 0.1$ in terms of normalized pressure, $\bar{p} = pL/aH$, as a function of the normalized deflection of the pole, $\bar{\delta} = \delta/L$. Two typical behaviour are found, depending on the value of material parameter β. For $\beta = 0.01$, the pressure reaches a limit point where a maximum value is attained. After the limit point, instability is triggered and a softening branch starts. In case of more complex material models, the pressure may increase again at larger values of deformation. For $\beta = 0.1$, the pressure vs. deflection curve is monotonic. Note that the membrane has no out-of-plane stiffness in the undeformed configuration. Figure 2.2(b) represents the deformed shapes corresponding to $\bar{\delta} = 2$ for both values of β. The higher value of pressure for the case of $\beta = 0.01$ results in a larger volume in the deformed shape.

2.4.2 Compressible materials

A classic stored energy function for a compressible Mooney-Rivlin material is [30–35]

$$W(I_1, I_2, I_3) = a(I_1 - 3) + b(I_2 - 3) + \Gamma(I_3), \tag{2.23}$$

where Γ is a convex function which satisfies a growth condition for both $I_3 \to 0^+$ and $I_3 \to \infty^+$. Ciarlet and Geymonat [36] proposed the following expression:

$$\Gamma(I_3) = c(I_3 - 1) - q \ln I_3. \tag{2.24}$$

Constants a, b, c and q are positive scalars. They are not indipendent. Indeed, to guarantee a stress free condition in the reference configuration, constant q must

satisfy

$$q = (a + 2b + c). \tag{2.25}$$

With this position and substituting (2.24) into (2.23), the expression of the stored energy function turns into

$$W(I_1, I_2, I_3) = a(I_1 - 3) + b(I_2 - 3) + c(I_3 - 1) - (a + 2b + c)\ln I_3. \tag{2.26}$$

The derivatives with respect to the principal strain invariants are

$$w_1 = a, \quad w_2 = b, \quad w_3 = c - \frac{a + 2b + c}{I_3}. \tag{2.27}$$

Imposing the membrane assumption $\sigma_3 = 0$, a closed relation between the transversal stretch λ_3 and λ_1, λ_2 is found

$$\lambda_3 = \sqrt{\frac{a + 2b + c}{a + \lambda_2^2(b + c\lambda_1^2) + b\lambda_1^2}} = g(\lambda_1, \lambda_2). \tag{2.28}$$

Note that when $c \to \infty$ Eq. (2.28) reduces to $\lambda_3 = 1/(\lambda_1\lambda_2)$, retrieving the relation for incompressible materials. The matematical simplicity of the Mooney-Rivlin model allows to obtain an explicit expression for the transversal stretch λ_3. Under this circumstance, the solution for a compressible material is formally equivalent to the solution for an incompressible material, provided the strain energy function

$$W(I_1, I_2, I_3) = \bar{W}(\lambda_1, \lambda_2, \lambda_3) = \bar{W}(\lambda_1, \lambda_2, g(\lambda_1, \lambda_2)) = \tilde{W}(\lambda_1, \lambda_2) \tag{2.29}$$

is assumed. When more complex strain energy function are used, the transversal stretch is linked to λ_1, λ_2 by an implicit relation and its computation requires numerical methods. This general circumstance will be treated in Chapter 6.

The principal Cauchy stresses σ_1 and σ_2 are computed by Eq.(2.6) with the use of Eq.(2.28)

$$\sigma_i = \frac{2a\left(\beta\lambda_j^2 + 1\right)\left(\lambda_i^4(\beta + \eta\lambda_2^2) + \lambda_i^2\left(\beta\lambda_j^2 + 1\right) - 2\beta - \eta - 1\right)}{\lambda_i\lambda_j\sqrt{2\beta + \eta + 1}\sqrt{\lambda_i^2\left(\beta + \eta\lambda_j^2\right) + \beta\lambda_j^2 + 1}}, \quad i, j = 1, 2 \tag{2.30}$$

where $\gamma = c/a$. The stress resultants per unit length T_1 and T_2 are computed as

$$T_i = \sigma_i\lambda_3 H = \frac{2aH\left(\beta\lambda_j^2 + 1\right)\left[\lambda_i^4\left(\beta + \gamma\lambda_j^2\right) + \lambda_i^2\left(\beta\lambda_j^2 + 1\right) - 2\beta - \gamma - 1\right]}{\lambda_i\lambda_j\left[\beta\lambda_j^2 + \lambda_i^2\left(\beta + \gamma\lambda_j^2\right) + 1\right]}, \quad i, j = 1, 2 \tag{2.31}$$

and the system of governing equations becomes

$$\begin{aligned}
\lambda_1' &= \frac{\xi_0 + \xi_1\lambda_2 + \xi_2\lambda_2^2 + \xi_3\lambda_2^3 + \xi_4\lambda_2^4 + \xi_5\lambda_2^5 + \xi_6\lambda_2^6 + \xi_7\lambda_2^7}{R\lambda_2(\beta\lambda_2^2 + 1)\left[\zeta\lambda_1^2 + 2\lambda_1^4(\beta\lambda_2^2 + 1)(\beta + \gamma\lambda_2^2) + \lambda_1^6(\beta + \gamma\lambda_2^2)^2 + (2\beta + \eta + 1)(\beta\lambda_2^2 + 1)\right]}, \\
\lambda_2' &= \frac{\eta - \lambda_2}{R}, \\
\eta' &= \frac{\kappa_1\lambda_1' + \kappa_3\left[\lambda_1 + \lambda_2^2\lambda_1(\beta + \gamma\lambda_1^2) + \beta\lambda_1^3\right] - 2\lambda_1(2\beta + \gamma + 1)(\beta\lambda_1^2 + 1)(\lambda_1^2 - \eta^2)}{2R\lambda_1\lambda_2(\beta\lambda_2^2 + 1)\left[\kappa_2 + \lambda_1^2\lambda_2^2(\beta + \gamma\lambda_1^2)\right]},
\end{aligned} \tag{2.32}$$

where, for the sake of clarity, the following quantities were defined

$$
\begin{aligned}
\xi_0 &= -\lambda_1^5\left(2\beta^3\eta+\beta^2\gamma\eta+\beta^2\eta\right)-\lambda_1^3\left(4\beta^2\eta+2\beta\gamma\eta+2\beta\eta\right)-\lambda_1\left(2\beta\eta+\gamma\eta+\eta\right),\\
\xi_1 &= -\beta^2\lambda_1^7-2\beta\lambda_1^5+\lambda_1^3\left(2\beta^2+\beta\gamma+\beta-1\right)+\lambda_1\left(2\beta+\gamma+1\right),\\
\xi_2 &= -\eta\beta^3\lambda_1^7-\lambda_1^5\left(2\beta^2\gamma\eta+\beta^2\eta+\beta\gamma^2\eta+\beta\gamma\eta\right)-\lambda_1\left(2\beta^2\eta+\beta\gamma\eta+\beta\eta-\eta\right)\\
&\quad+\lambda_1^3\left(2\beta^3\eta+\beta^2\gamma\eta+\beta^2\eta-6\beta\gamma\eta+\beta\eta-3\gamma^2\eta-3\gamma\eta\right),\\
\xi_3 &= \lambda_1^7\left(\beta^3-2\beta\gamma\right)-2\gamma\lambda_1^5-\lambda_1^3\left(2\beta^3+\beta^2\gamma+\beta^2-6\beta\gamma+\beta-3\gamma^2-3\gamma\right)\\
&\quad+\lambda_1\left(4\beta^2+2\beta\gamma+2\beta\right),\\
\xi_4 &= -2\beta^2\gamma\eta\lambda_1^7-2\beta^3\eta\lambda_1^5+2\gamma\eta\lambda_1^3+2\beta\eta\lambda_1,\\
\xi_5 &= \lambda_1^7\left(2\beta^2\gamma-\gamma^2\right)+2\beta^3\lambda_1^5+\lambda_1^3\left(2\beta^2\gamma+\beta^2+\beta\gamma^2+\beta\gamma\right)\\
&\quad+\lambda_1\left(2\beta^3+\beta^2\gamma+\beta^2\right),\\
\xi_6 &= -\eta\beta\gamma^2\lambda_1^7-\lambda_1^5\left(2\beta^2\gamma\eta-\gamma^2\eta\right)-\lambda_1^3\left(\beta^3\eta-2\beta\gamma\eta\right)+\beta^2\eta\lambda_1,\\
\xi_7 &= \beta\gamma^2\lambda_1^7+2\beta^2\gamma\lambda_1^5+\beta^3\lambda_1^3,\\
\zeta &= \beta^2\lambda_2^4+\lambda_2^2\left[\beta\left(6\gamma+2\right)+3\gamma\left(\gamma+1\right)\right]+3\beta\left(2\beta+\gamma+1\right)+1,\\
\kappa_1 &= 2\beta R\eta\lambda_1^2\lambda_2^5\left(\beta+\gamma\lambda_1^2\right)+2R\eta\lambda_2^3\left[\beta^2\left(\lambda_1^4-2\right)+\gamma\lambda_1^4+\beta\left(2\lambda_1^2-\gamma-1\right)\right]\\
&\quad+2\kappa_2 R\eta\lambda_2,\\
\kappa_2 &= \beta\lambda_1^4+\lambda_1^2-2\beta-\gamma-1,\\
\kappa_3 &= \lambda_2^2\left[2\beta\lambda_1^4-\lambda_1^2\left(\beta\sqrt{\lambda_1^2-\eta^2}+2\beta\eta^2-2\right)-2\eta^2\right].
\end{aligned}
\tag{2.33}
$$

3 Approximate analytical solution for inflated circular membranes

In Chapter 2 the numerical solution for the benchmark problem of the inflation of circular membranes was presented. The mathematical complexity arising from the equilibrium equations, as well as from geometrical and material nonlinearities, has forced researchers to analyse this problem by means numerical approaches. Only a few simplified analytical models are available in the literature. However, each of these models suffers from limitations and it results valid only for particular values of material parameters and magnitude of deformation. As a result, there is still a lack of analytical solutions available as immediate and efficient tool for broad practical applications.

In this chapter, a simplified model for the inflation of circular, initially unstretched membranes is presented. The components of both displacement field and displacement gradient are considered large. The simplifying assumption consists in considering spherical caps as deformed configurations for the membrane. A compressible Mooney-Rivlin material model is assumed as constitutive law. The equilibrium at the pole of the membrane allows to derive the approximate response of the membrane in terms of pressure-deflection curve.

Being based on a simplifying assumption, this approximate solution loses accuracy in corrispondence of some values of material parameters and some range of deformation, when the actual deformed configuration of the membrane is far from being spherical. For this reason, the approximate solution needs an adjustment. The correction is performed by fitting the exact numerical solution of the problem by means of a polynomial corrective function. The corrective function is calibrated for a wide range of material parameters, covering all the range of practical interest. As a result, the adjusted pressure-deflection formula is valid regardless of geometrical parameters, material parameters and magnitude of deformation. Despite being calibrated for the simpler case of incompressible materials, the adjusted formula is proved to be valid also for compressible materials. The linearization of the proposed model is then performed, showing how it reduces to the linearized theory of elasticity provided that the components of both displacement field and displacement gradient are considered small.

The proposed solution is further validated by finite element simulations. Successively, it is compared with the simplified analytical models found in literature, demonstrating how it overcomes their limitations and it results reliable for every range of material parameters and deformation. Finally, experimental bulge tests on three different kind of elastomers are carried out. The adjusted formula is used to fit the experimental data and to calibrate the material parameters, proving to be a powerful tool for material characterization under biaxial stress state.

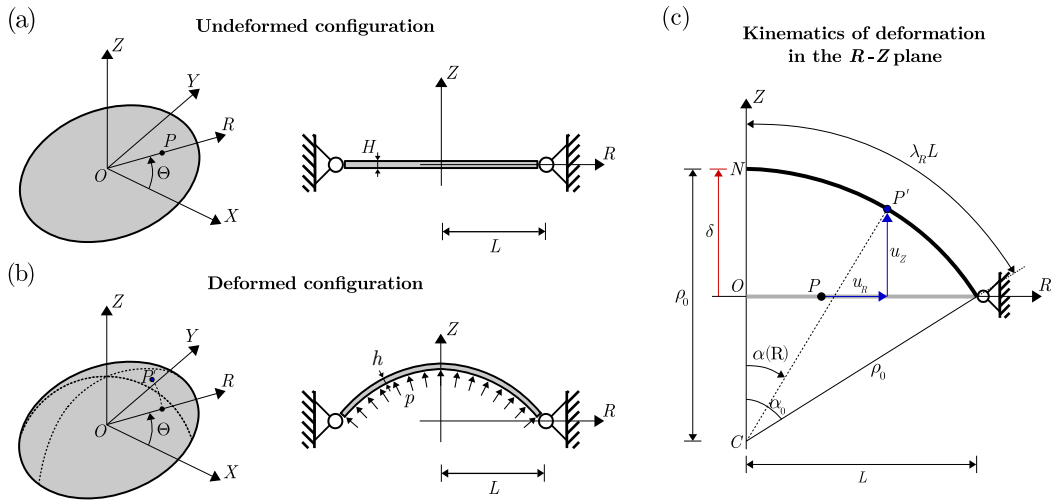

Figure 3.1: Circular flat membrane subjected to uniform lateral pressure p. Representation of (a) undeformed and (b) deformed configurations. The membrane is axisymmetric and therefore the kinematics of deformation is described in the R-Z plane, as shown in (c). It is assumed that the membrane transforms into a spherical cap with central angle $2\alpha_0$ and radius ρ_0. The deflection of the central point of the membrane is denoted with δ. The kinematics of deformation is completely described as a function of single parameter.

3.1 Analytical model

Consider again a circular flat membranes with radius L and thickness H, shown in Fig. 3.1(a-b). The membrane is subjected to an uniform lateral pressure p. It is assumed that, under the action of pressure p, the membrane deforms into spherical caps. The kinematics of deformation derived by this assumption is described in Fig. 3.1(c). Note that, contrary to the general case where the deformed shape is described by two indipendent functions, the simplifying assumption allows to describe completely the deformed shape with a single degree of freedom. A generic material point P with coordinates $(R, \Theta, 0)$ in a cylindrical reference frame moves to P', with coordinates (r, Θ, z). The displacement field of point P reads

$$\begin{cases} u_R(P) = \rho_0 \sin\alpha(R) - R, \\ u_\Theta(P) = 0, \\ u_Z(P) = \rho_0 \left[\cos\alpha(R) - \cos\alpha_0\right], \end{cases} \tag{3.1}$$

with $\alpha_0 \in (0, \pi)$ and

$$\rho_0 = \frac{L}{\sin\alpha_0}, \qquad \alpha(R) = \frac{\alpha_0 R}{L}. \tag{3.2}$$

Hereinafter, the dependence of angle α on the radial coordinate R will be omitted for the sake of simplicity. The deformation of point P is defined as

$$\boldsymbol{\varphi}(P) = \mathbf{id}(P) + \mathbf{u}(P), \tag{3.3}$$

whose representation in cylindrical components is

$$\begin{cases} \varphi_R(P) = r = \rho_0 \sin\alpha, \\ \varphi_\Theta(P) = \theta = \Theta, \\ \varphi_Z(P) = z = \rho_0 \left(\cos\alpha - \cos\alpha_0\right). \end{cases} \tag{3.4}$$

The gradient of the deformation vector expressed in cylindrical coordinates is

$$[\nabla\boldsymbol{\varphi}] = \begin{bmatrix} \dfrac{\partial r}{\partial R} & \dfrac{1}{R}\dfrac{\partial r}{\partial \Theta} & \dfrac{\partial r}{\partial Z} \\ r\dfrac{\partial \theta}{\partial R} & \dfrac{r}{R}\dfrac{\partial \theta}{\partial \Theta} & r\dfrac{\partial \theta}{\partial Z} \\ \dfrac{\partial z}{\partial R} & \dfrac{1}{R}\dfrac{\partial z}{\partial \Theta} & \dfrac{\partial z}{\partial Z} \end{bmatrix} = \begin{bmatrix} \rho_0 \dfrac{\partial \alpha}{\partial R}\cos\alpha & 0 & 0 \\ 0 & \dfrac{\rho_0 \sin\alpha}{R} & 0 \\ -\rho_0 \dfrac{\partial \alpha}{\partial R}\sin\alpha & 0 & 0 \end{bmatrix}. \tag{3.5}$$

The third column of the matrix representation of $\nabla\boldsymbol{\varphi}$ is empty because it is assumed that the membrane is a two-dimensional body. In order to consider a deformation along the thickness of the membrane, the stretch λ_Z along Z direction is introduced. Thus, the deformation gradient is defined as

$$[\mathbf{F}] = \begin{bmatrix} \rho_0 \dfrac{\partial \alpha}{\partial R}\cos\alpha & 0 & \lambda_Z \sin\alpha \\ 0 & \dfrac{\rho_0 \sin\alpha}{R} & 0 \\ -\rho_0 \dfrac{\partial \alpha}{\partial R}\sin\alpha & 0 & \lambda_Z \cos\alpha \end{bmatrix}. \tag{3.6}$$

In this way, the thickness H in the undeformed configuration transforms into $h = \lambda_Z H$ in deformed configuration. The polar decomposition of the deformation gradient, $\mathbf{F} = \mathbf{R}\mathbf{U}$, allows to write the rotation tensor $\mathbf{R}$ and the pure deformation tensor $\mathbf{U}$:

$$[\mathbf{R}] = \begin{bmatrix} \cos\alpha & 0 & \sin\alpha \\ 0 & 1 & 0 \\ -\sin\alpha & 0 & \cos\alpha \end{bmatrix}, \qquad [\mathbf{U}] = \begin{bmatrix} \lambda_R & 0 & 0 \\ 0 & \lambda_\Theta & 0 \\ 0 & 0 & \lambda_Z \end{bmatrix}, \tag{3.7}$$

where

$$\lambda_R = \rho_0 \frac{\partial \alpha}{\partial R} = \frac{\alpha_0 \rho_0}{L}, \qquad \lambda_\Theta = \frac{\rho_0 \sin\alpha}{R}. \tag{3.8}$$

The radial stretch λ_R is constant, as a consequence of assuming spherical deformed configurations for the membrane. Tensor $\mathbf{U}$ is diagonal, meaning that reference system (R, Θ, Z) is principal in the undeformed configuration and λ_R, λ_Θ and λ_Z are the principal stretches. The right Cauchy-Green deformation tensor $\mathbf{C} = \mathbf{F}^T\mathbf{F}$ reads

$$[\mathbf{C}] = \begin{bmatrix} \lambda_R^2 & 0 & 0 \\ 0 & \lambda_\Theta^2 & 0 \\ 0 & 0 & \lambda_Z^2 \end{bmatrix}. \tag{3.9}$$

The first Piola-Kirchhoff stress tensor is expressed by the constitutive equation

$$\mathbf{T}_R(\mathbf{F}) = \frac{\partial W}{\partial \mathbf{F}} = 2\left[\left(\frac{\partial W}{\partial I_1} + I_1 \frac{\partial W}{\partial I_2}\right)\mathbf{F} - \frac{\partial W}{\partial I_2}\mathbf{R}\mathbf{U}^3 + I_3 \frac{\partial W}{\partial I_3}\mathbf{R}\mathbf{U}^{-1}\right]. \tag{3.10}$$

This equation can be rewritten as [37]

$$\mathbf{T}_R = \mathbf{RS}, \tag{3.11}$$

where diagonal tensor $\mathbf{S}$ is the Biot stress tensor and is defined as

$$[\mathbf{S}] = \begin{bmatrix} S_R & 0 & 0 \\ 0 & S_\Theta & 0 \\ 0 & 0 & S_Z \end{bmatrix}, \tag{3.12}$$

with

$$S_i = 2\left[\left(\frac{\partial W}{\partial I_1} + I_1\frac{\partial W}{\partial I_2}\right)\lambda_i - \frac{\partial W}{\partial I_2}\lambda_i^3 + I_3\frac{\partial W}{\partial I_3}\lambda_i^{-1}\right], \quad \text{for} \quad i = R, \Theta, Z. \tag{3.13}$$

The membrane is assumed to be made of the compressible Mooney-Rivlin material model introduced in Eq. (2.26). The derivatives with respect to the principal invariants are given by Eq. (2.27), and the components of the Biot stress tensor specialise to

$$\begin{aligned} S_R &= 2\lambda_R\left[a - \frac{a+2b+c}{\lambda_R^2} + \lambda_\Theta^2\left(b + c\lambda_Z^2\right) + b\lambda_Z^2\right], \\ S_\Theta &= 2\lambda_\Theta\left[a - \frac{a+2b+c}{\lambda_\Theta^2} + \lambda_Z^2\left(b + c\lambda_R^2\right) + b\lambda_R^2\right], \\ S_Z &= 2\lambda_Z\left[a - \frac{a+2b+c}{\lambda_Z^2} + \lambda_R^2\left(b + c\lambda_\Theta^2\right) + b\lambda_\Theta^2\right]. \end{aligned} \tag{3.14}$$

Imposing the plane stress condition, $S_Z = 0$, the relation for the transversal stretch is determined

$$\lambda_Z = \sqrt{\frac{a+2b+c}{a + \lambda_\Theta^2\left(b + c\lambda_R^2\right) + b\lambda_R^2}} = g\left(\lambda_R, \lambda_\Theta\right), \tag{3.15}$$

which coincides with Eq. (2.28). Again, for $c \to \infty$ the relation for incompressible materials $\lambda_Z = 1/\left(\lambda_R\lambda_\Theta\right)$ is retrieved.

The Cauchy stress tensor is defined as $\mathbf{T} = (\det\mathbf{F})^{-1}\,\mathbf{T_R}\mathbf{F}^T$ [38]. The principal directions (r, θ, z) for the Cauchy stress tensor are identified by applying the rotation given by tensor $\mathbf{R}$ to the material reference system (R, Θ, Z). The principal directions (r, θ, z) coincide with the meridians, the circumferential lines and the normal direction to thickness, and pedices 1,2,3 respectively will be used hereinafter for consistency with Chapter 2. The diagonal form of the Cauchy stress tensor in the principal reference system is $\mathbf{T} = (\det\mathbf{F})^{-1}\,\mathbf{R}^T\mathbf{T_R}\mathbf{F}^T\mathbf{R}$, which gives the following result:

$$\begin{aligned} \sigma_1 &= \frac{2}{\lambda_R\lambda_\Theta\lambda_Z}\left[a\left(\lambda_R^2 - 1\right) + b\left(\lambda_R^2\lambda_Z^2 - 2\right) + \lambda_R^2\lambda_\Theta^2\left(b + c\lambda_Z^2\right) - c\right], \\ \sigma_2 &= \frac{2}{\lambda_R\lambda_\Theta\lambda_Z}\left[a\left(\lambda_\Theta^2 - 1\right) + b\left(\lambda_R^2\lambda_\Theta^2 - 2\right) + \lambda_\Theta^2\lambda_Z^2\left(b + c\lambda_R^2\right) - c\right], \\ \sigma_3 &= \frac{2}{\lambda_R\lambda_\Theta\lambda_Z}\left[a\left(\lambda_Z^2 - 1\right) + b\left(\lambda_R^2\lambda_Z^2 - 2\right) + \lambda_\Theta^2\lambda_Z^2\left(b + c\lambda_R^2\right) - c\right]. \end{aligned} \tag{3.16}$$

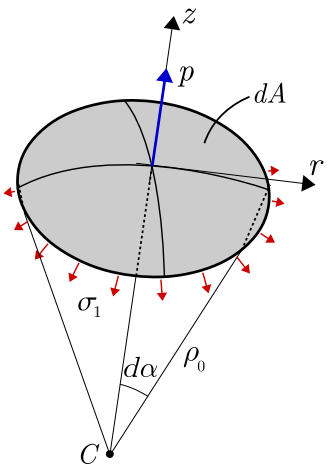

Figure 3.2: Local equilibrium in z direction written in the neighborhood of the central point of the circular membrane. The applied pressure p is balanced by the radial stress component σ_1.

Substitution of Eq. (3.15) into Eq. (3.16) gives $\sigma_3 = 0$. This result is consistent with the plane stress condition along the thickness of the membrane.

After having derived the stress components, the equilibrium equations can be written. Since the kinematics of deformation was restrained a priori to spherical deformed configuration, it is not possible to satisfy the equilibrium equations locally at every point of the membrane. However, an approximate solution can be derived imposing the local equilibrium in the neighborhood of the most representative point of the inflated membrane, namely the central point. To this aim, the equilibrium equation in z direction for $R \to 0$ is written. Fig. 3.2 shows the external force generated by pressure p acting on area $dA = \pi\rho_0^2 d\alpha^2$. This force is balanced by the projection of the meridian stress σ_1 along z direction, which acts on area $2h\pi\rho_0 d\alpha$. With the approximation $\sin d\alpha \cong d\alpha$, the local equilibrium for $R \to 0$ reads

$$p\left(\pi\rho_0^2 d\alpha^2\right) = d\alpha\,(2h\pi\rho_0 d\alpha)\,\sigma_1\big|_{R\to 0}, \tag{3.17}$$

from which the following expression for the applied pressure is derived:

$$p = \frac{2\,(\sigma_1 h)\,\big|_{R\to 0}}{\rho_0}, \tag{3.18}$$

with $h = \lambda_Z H$ and λ_Z given by Eq. (3.15).

The meridian stress σ_1 for the case of $R \to 0$ reads

$$\sigma_1\big|_{R\to 0} = \frac{2\sin^2\alpha_0\left(\alpha_0^2\csc^2\alpha_0 - 1\right)\left(a+b\alpha_0^2\csc^2\alpha_0\right)\left[a+2b+\alpha_0^2\csc^2\alpha_0\,(2b+c)+c\left(1+\alpha_0^4\csc^4\alpha_0\right)\right]}{\alpha_0^2\sqrt{(a+2b+c)\left(a+2b\alpha_0^2\csc^2\alpha_0+c\alpha_0^4\csc^4\alpha_0\right)}}. \tag{3.19}$$

Transversal stretch λ_Z assumes the following form with $R \to 0$:

$$\lambda_Z\big|_{R\to 0} = \sqrt{\frac{a+2b+c}{a+2b\alpha_0^2\csc^2\alpha_0+c\alpha_0^4\csc^4\alpha_0}}. \tag{3.20}$$

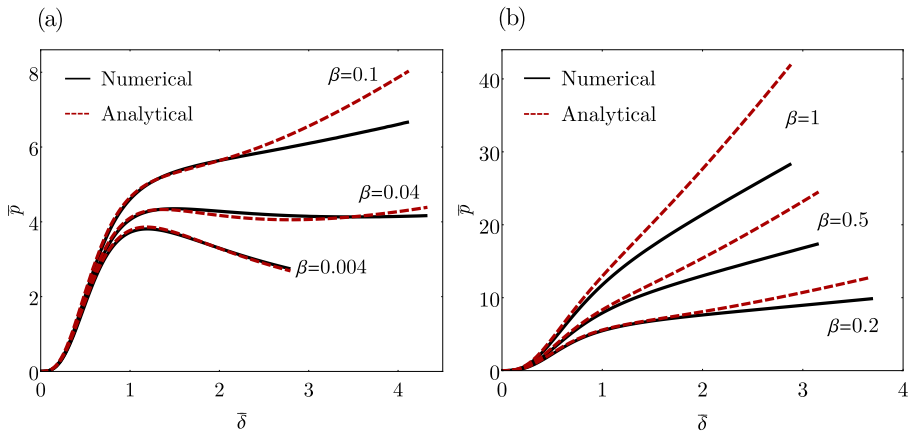

Figure 3.3: Normalized pressure $\bar{p} = pL/(aH)$ vs. normalized deflection at the pole $\bar{\delta} = \delta/L$ for different values of β. The analytical curves are given by Eq. (3.22). For low values of β (a) the approximate analytical solution results accurate, whereas for higher values of β (b) it exhibits significant errors. The errors increase as the deformation increases.

Introducing the normalized pressure as $\bar{p} = pL/(aH)$, the expression that links $\bar{p}$ to the kinematic parameter α_0 is finally derived by substituting Eqs. (3.1) and (3.20) into Eq. (3.18), obtaining [39]

$$\bar{p} = \frac{4\sin^3\alpha_0\left(\alpha_0^2\csc^2\alpha_0-1\right)\left(1+\beta\,\alpha_0^2\csc^2\alpha_0\right)\left[1+2\beta+\alpha_0^2\csc^2\alpha_0(2\beta+\gamma)+\gamma\left(1+\alpha_0^4\csc^4\alpha_0\right)\right]}{\alpha_0^2\left(1+2\beta\,\alpha_0^2\csc^2\alpha_0+\gamma\,\alpha_0^4\csc^4\alpha_0\right)}. \quad (3.21)$$

The kinematics is governed by parameter α_0 (see Fig. 3.1(c)), which is related to displacement δ of the central node of the membrane through the relation $\alpha_0 = 2\tan^{-1}\bar{\delta}$. The expression of pressure $\bar{p}$ given by Eq. (3.21) can be thus written directly as a function of deflection $\bar{\delta}$. This provides the equilibrium path of the inflated membrane in terms of pressure-deflection curve. In case of incompressible materials, computing the limit of Eq. (3.21) for $\gamma \to \infty$, the normalized pressure reads

$$\bar{p}\big|_{\gamma\to\infty} = \frac{4\sin^7\alpha_0}{\alpha_0^6}\left(1+\beta\,\alpha_0^2\csc^2\alpha_0\right)\left(\alpha_0^6\csc^6\alpha_0-1\right). \quad (3.22)$$

Note that the normalized pressure is indipendent from the geometrical parameters of the membrane. Indeed, variations on geometrical parameters, H and L, have the only effect of scaling the dimensional value of the external pressure. Regarding the effect of Mooney-Rivlin parameters, in case of incompressible materials the only dependence is on parameter β. In case of compressible materials there is a further dependence on parameter γ, which takes into account volume changes. In both cases, parameter a only causes a scaling in the dimensional pressure.

Figures 3.3 compares the analytical pressure provided by Eq. (3.22) with the pressure given by the numerical solution for different values of β. It is evident how the approximate analytical curve is accurate for low values of β, whereas it exhibits significant discrepancies as β increases. These discrepancies increase with

the deformation. For low values of β, the actual deformed shape is close to a spherical cap, therefore the error made by the assumption of the model is modest and the analytical pressure results accurate. For high values of β, the deformed shapes turn away from spherical caps, thus leading to important errors in the pressure curve.

The limited validity of the approximate analytical pressure to small values of β and small deformations makes necessary an adjustment of the proposed formula. This adjustment is performed in the following section by calibrating a corrective polynomial function based on the numerical solution of the problem. The corrective polynomial is calibrated for the case of incompressible materials, since in this case the dependence on material parameters is reduced only to parameter β. Successively, the calibrated formula is proved to be valid also for compressible materials.

3.2 Adjustment of the pressure curves

The approximate analytical formula for the pressure is adjusted by introducing an additional polynomial function. The coefficients of the polynomial function are calibrated by fitting the pressure vs. deflection curves given by the numerical solution for incompressible materials.

In case of incompressible materials, the governing equations depend on the Mooney-Rivlin parameters only through ratio β. Once fixed this parameter, variations of a cause only a scaling in the value of pressure. For this reason, it is straightforward to study the influence of the constitutive parameters on the solution of the problem. A set of values for β ranging from 0 to 1 is defined. The choice of this range aims to address all the typical values of β that can be found in the literature for real rubber materials [40–43]. All the rubbers employed in technological applications are characterized by a value of β included in such range and therefore the numerical simulations cover all the possible material behaviors. Overall, 70 values for β are considered. From 0.04 to 1 parameter β varies with a step of 0.02. In the range 0–0.04 the step decreases to 0.002. Indeed, in this range small variations of β are more significant, since they determine the transition from softening to hardening behavior at large deformations.

For each value of β, the numerical solution is obtained following the procedure described in Section 2.3. For each value of β, the analysis is limited to a maximum stretch that does not exceed 7 at any point of the membrane. This choice is consistent with physical evidence, since most rubbers subjected to uniaxial tensile test reach failure for stretches lower than 7 [44]. Note that the circumferential stretch λ_Θ always decreases moving from the pole to the outer boundary, due to the boundary condition $\lambda_\Theta(L) = 1$. Instead, the radial stretch λ_R increases or decreases along the radius depending on constitutive parameter β and on the magnitude of deformation. Therefore, λ_R does not always assume its maximum value at the central node of the membrane.

The proposed expression for the adjusted pressure is the following

$$\bar{p}_{adj} = \bar{p} \sum_{j=1}^{10} f_j(\beta)\, \phi^j, \tag{3.23}$$

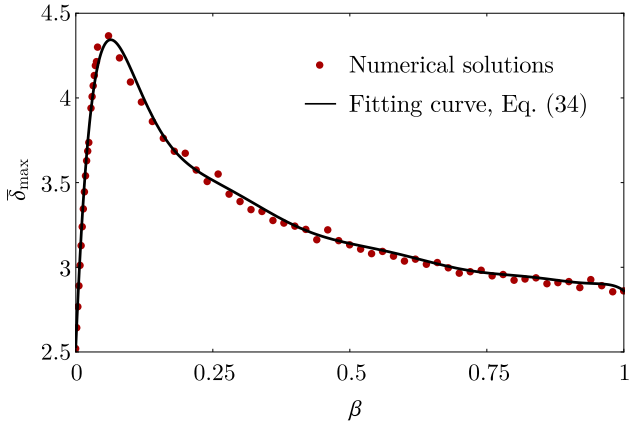

Figure 3.4: Discrete values of normalized maximum deflection $\bar{\delta}_{\max,\mathrm{i}} = \delta_{\max,\mathrm{i}}/L$ obtained from the numerical solution for different material parameters β (red dots) and fitting curve (continuous line), expressed by Eq. (3.25). The maximum deflection $\delta_{\max}$ refers to the deflection of the pole corresponding to the achievement of a radial stretch equal to 7 somewhere in the membrane.

where $\bar{p}$ is the approximate pressure given by Eq.(3.22) and

$$f_j(\beta) = \sum_{k=0}^{10} d_{jk}\beta^k, \quad \phi = \frac{\bar{\delta}}{\bar{\delta}_{\max}(\beta)}. \tag{3.24}$$

In the following, $\bar{\delta}_{\max}$ indicates the normalized vertical displacement at the pole that produces a radial stretch equal to 7 somewhere in the membrane. The variables ϕ has the advantage of varying in the range $[0,1]$, simplifying the fitting procedure. The values $\bar{\delta}_{\max,i}$ obtained from the numerical simulations are displayed as a function of β in Fig. 3.4. As expected, different values of β correspond to different values of maximum deflection $\bar{\delta}_{\max}$ at the pole, at which a radial stretch equal to 7 is reached somewhere in the membrane. A regression law for $\bar{\delta}_{\max}$ as a function of β is estimated by using the *NonlinearModelFit* function of software Wolfram Mathematica. *NonlinearModelFit* uses a least-square approach to find the set of parameters for the regression law which best fit the discrete values $\bar{\delta}_{\max,i}$. The following polynomial regression is derived:

$$\bar{\delta}_{\max}(\beta) = \sum_{i=0}^{12} c_i\beta^i, \tag{3.25}$$

with coefficients c_i, $i = 0,...,12$, listed in Tab. 3.1. The regression is displayed in Fig. 3.4, showing that it provides an accurate fit for the discrete values of maximum displacement obtained from the numerical simulations.

Functions $f_j(\beta)$, $j = 1,...,10$, assume different values for each of the values of β considered in the numerical simulations. The values of f_j were again estimated by using the *NonlinearModelFit* function of software Wolfram Mathematica. The best fitting coefficients d_{jk}, with $j = 1,...,10$ and $k = 0,...,12$, are listed in Tab. 3.2.

Table 3.1: Coefficients of the polynomial regression for $\bar{\delta}_{\max}$ that fits the discrete values $\bar{\delta}_{\max,i}$ of maximum deflection obtained from the numerical solutions of the TPBVP.

c_0	c_1	c_2	c_3	c_4	c_5	c_6
c_7	c_8	c_9	c_{10}	c_{11}	c_{12}	
2.53	74.33	-973.79	3790.21	1.56×10^{4}	-2.20×10^{5}	1.02×10^{6}
-2.72×10^{6}	4.56×10^{6}	-4.92×10^{6}	3.31×10^{6}	-1.27×10^{6}	2.13×10^{5}	

Table 3.2: Coefficients $d_{j,k}$ estimated to fit the adjusted analytical expression of pressure, Eq. (3.26), to the numerical solutions of the TPBVP.

	d_{j0}	d_{j1}	d_{j2}	d_{j3}	d_{j4}	d_{j5}	d_{j6}
	d_{j7}	d_{j8}	d_{j9}	d_{j10}	d_{j11}	d_{j12}	
$j=1$	25.13	53.33	132.47	-18829.3	2.37×10^{5}	-1.46×10^{6}	5.37×10^{6}
	-1.27×10^{7}	1.99×10^{7}	-2.05×10^{7}	1.33×10^{7}	-4.98×10^{6}	8.14×10^{5}	
$j=2$	-290.11	-1159.72	8012.55	1.75×10^{5}	-2.93×10^{6}	1.96×10^{7}	-7.55×10^{7}
	1.83×10^{8}	-2.90×10^{8}	3.01×10^{8}	-1.97×10^{8}	7.38×10^{7}	-1.21×10^{7}	
$j=3$	1894.3	13452.8	-2.21×10^{5}	8.86×10^{5}	5.24×10^{6}	-6.82×10^{7}	3.18×10^{8}
	-8.45×10^{8}	1.41×10^{9}	-1.51×10^{9}	1.0×10^{9}	-3.81×10^{8}	6.26×10^{7}	
$j=4$	-7648.76	-86636.6	1.88×10^{6}	-1.65×10^{7}	7.40×10^{7}	-1.66×10^{8}	8.08×10^{7}
	5.39×10^{8}	-1.55×10^{9}	2.06×10^{9}	-1.54×10^{9}	6.20×10^{8}	-1.05×10^{8}	
$j=5$	19981.7	3.24×10^{5}	-7.94×10^{6}	8.29×10^{7}	-4.92×10^{8}	1.84×10^{9}	-4.62×10^{9}
	7.96×10^{9}	-9.58×10^{9}	7.95×10^{9}	-4.37×10^{9}	1.44×10^{9}	-2.19×10^{8}	
$j=6$	-34385.5	-7.37×10^{5}	1.91×10^{7}	-2.15×10^{8}	1.39×10^{9}	-5.77×10^{9}	1.61×10^{10}
	-3.13×10^{10}	4.22×10^{10}	-3.89×10^{10}	2.35×10^{10}	-8.35×10^{9}	1.32×10^{9}	
$j=7$	38714.9	1.03×10^{6}	-2.76×10^{7}	3.25×10^{8}	-2.19×10^{9}	9.52×10^{9}	-2.78×10^{10}
	5.59×10^{10}	-7.80×10^{10}	7.39×10^{10}	-4.55×10^{10}	1.64×10^{10}	-2.62×10^{9}	
$j=8$	-27441.4	-8.73×10^{5}	2.39×10^{7}	-2.88×10^{8}	2.01×10^{9}	-8.92×10^{9}	2.66×10^{10}
	-5.48×10^{10}	7.76×10^{10}	-7.45×10^{10}	4.63×10^{10}	-1.68×10^{10}	2.70×10^{9}	
$j=9$	11109	4.08×10^{5}	-1.14×10^{7}	1.40×10^{8}	-9.93×10^{8}	4.50×10^{9}	-1.36×10^{10}
	2.84×10^{10}	-4.07×10^{10}	3.94×10^{10}	-2.46×10^{10}	8.97×10^{9}	-1.44×10^{9}	
$j=10$	-1958.21	-81261.5	2.29×10^{6}	-2.87×10^{7}	2.07×10^{8}	-9.51×10^{8}	2.92×10^{9}
	-6.14×10^{9}	8.86×10^{9}	-8.63×10^{9}	5.41×10^{9}	-1.98×10^{9}	3.19×10^{8}	

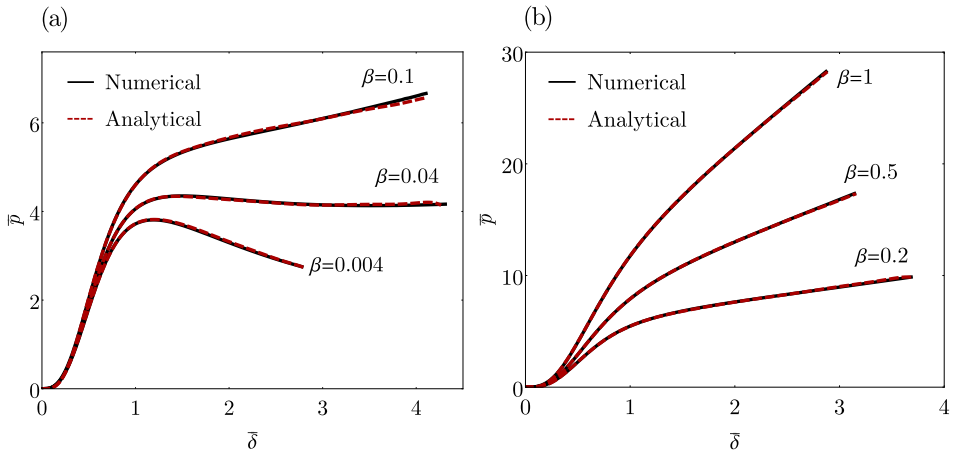

Figure 3.5: Normalized pressure $\bar{p} = pL/(aH)$ vs. normalized deflection at the pole $\bar{\delta} = \delta/L$ for different values of β. Comparison between the numerical solution and the adjusted analytical pressure, computed from Eq. (3.26). The analytical formula results accurate for every value of material parameter β and every magnitude of deformation.

The final adjusted expression for the pressure as a function of the deflection of the membrane is

$$\bar{p}_{adj}\left(\beta,\bar{\delta}\right) = \bar{p}\big|_{\gamma\to\infty} \sum_{j=1}^{10} \left(\frac{\bar{\delta}}{\bar{\delta}_{\max}}\right)^{j} \sum_{k=0}^{12} d_{jk}\beta^{k} = \bar{p}\big|_{\gamma\to\infty} F\left(\beta,\bar{\delta}\right), \tag{3.26}$$

with $\bar{p}\big|_{\gamma\to\infty}$ given by Eq. (3.22) and $\bar{\delta}_{\max}$ given by Eq. (3.25).

Figures 3.5(a) and (b) show the comparison between the numerical solution and the adjusted analytical pressure, computed from Eq. (3.26). The plots are given for $\beta = 0.004, 0.04, 0.1, 0.2, 0.5, 1$. The adjusted formula now provides values of pressure accurate for every value of parameter β and for every magnitude of deformation. It is worth stressing that the definition of the analytical model has been an important step to derive a final accurate formula, even if the model was based on a simplified assumption. Having already available an expression for $\bar{p}$ based on the physics of the problem simplified considerably the fitting procedure, which could have been otherwise very complex or even unfeasible.

On the other hand, the proposed model renounces to an accurate description of the kinematics of the membrane. From a theoretical point of view, adjusting the kinematics by fitting the deformed configurations of the numerical solution could be another possible approach. Once determined the kinematics, the pressure could then be obtained from the equilibrium equation (3.18). However, due to the high nonlinearity of the problem, small discrepancies in the deformed configurations lead to considerable errors in the pressure-deflection curve, making this approach unpracticable. In light of this consideration, a certain approximation on the deformed configuration must be accepted. Fig. 3.6(a) shows the deformed configuration at

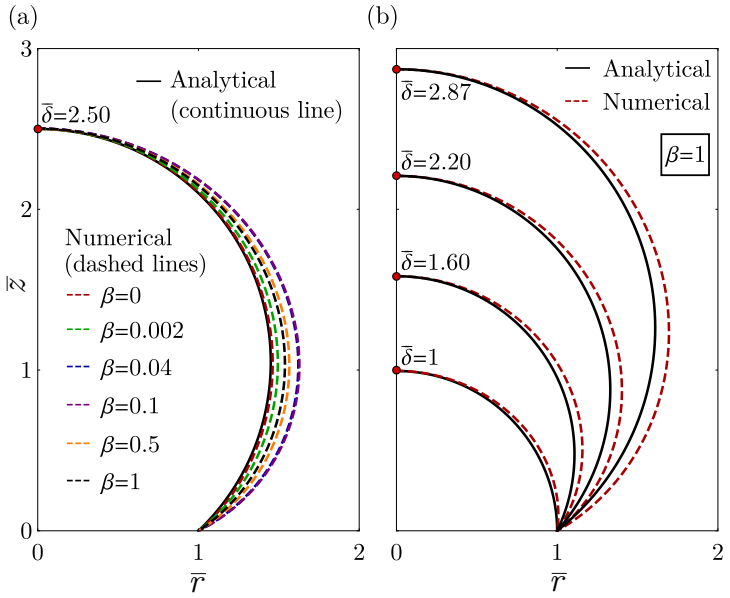

Figure 3.6: Normalized deformed shapes ($\bar{r} = r/L$ and $\bar{z} = z/L$) at (a) $\bar{\delta} = 2.5$ for different values of β and (b) $\beta = 1$ for different values of $\bar{\delta}$. Continuous black lines represent the spherical deformed shapes assumed by the analytical model, whereas dashed lines represent the actual deformed shapes obtained by the numerical solution. The discrepancy between the spherical caps and the actual deformed shapes increases with the increasing of deflection and depends on the value of material parameter β.

$\bar{\delta} = 2.5$ for different values of β. For $\beta = 0$ the numerical deformed shape is very close to a spherical cap, indeed even the approximate formula resulted very accurate. For other values of β the error increases, showing a trend similar to $\bar{\delta}_{\max}$. The error has a peak around $\beta = 0.1$ and then it decreases. Figure 3.6(b) compares the analytical and numerical deformed configurations for $\beta = 1$ at different values of $\bar{\delta}$. As expected, the discrepancy increases as the deformation increases. On one hand, despite the discrepancies in the deformed shape always remain modest, the proposed model can not be used to extract accurate information on the kinematics of the membrane. On the other hand, it is worth to remark that the pressure curve represents the most important tool in engineering applications. In this sense, the proposed analytical pressure gives very accurate predictions.

Despite it is not possible to provide an accurate description of the entire kinematics of the membrane, it would be useful to provide some information regarding the state of strain and stress at the pole, which is usually the most representative and critical point of the membrane. At the pole the circumferential stretch and radial stretch coincide and are given by

$$\lambda_\Theta\big|_{R\to 0} = \lambda_R = \frac{\alpha_0}{\sin\alpha_0}, \tag{3.27}$$

where $\alpha_0 = 2\tan^{-1}\bar{\delta}$. It goes without saying that Eq. (3.27) is subjected to the

Table 3.3: Coefficients q_{ij} of the adjusted analytical expression of the stretch at the pole, Eq. (3.28), estimated by fitting the numerical solutions of the TPBVP.

	q_{i0}	q_{i1}	q_{i2}	q_{i3}	q_{i4}	q_{i5}	q_{i6}
	q_{i7}	q_{i8}	q_{i9}	q_{i10}	q_{i11}	q_{i12}	
$i=1$	0.31	77.11	-2373.13	32253.9	-2.48×10^5	1.19×10^6	-3.76×10^6
	8.05×10^6	-1.17×10^7	1.14×10^7	-7.14×10^6	2.59×10^6	-4.13×10^5	
$i=2$	0.74	-124.24	3257.57	-41512.8	3.07×10^5	-1.44×10^6	4.49×10^6
	-9.48×10^6	1.36×10^7	-1.32×10^7	8.21×10^6	-2.96×10^6	4.71×10^5	

same approximation that affects the deformed shapes and it needs to be corrected. The same procedure described for the pressure is now applied to fit the analytical stretch at the pole to the correct stretch given by the numerical solution. The adjusted analytical expression for the stretch at the pole reads

$$\lambda_{adj}\left(\bar{\delta},\beta\right)=\frac{\alpha_0}{\sin\alpha_0}\left(1+\sum_{i=1}^{2}\left(\frac{\bar{\delta}}{\bar{\delta}_{\max}}\right)^i\sum_{j=0}^{12}q_{ij}\beta^j\right), \tag{3.28}$$

where coefficients q_{ij}, with $i=1,2$ and $j=0,...,12$, are listed in Tab. 3.3. The principal components in radial and circumferential directions of the Piola-Kirchhoff stress tensor coincide at the pole. The corrected value of the nominal stress at the pole can be computed by imposing $\lambda_R=\lambda_\Theta=\lambda_{adj},\lambda_Z=g\left(\lambda_{adj},\lambda_{adj}\right)$ in Eq. (3.14). The following expression for the nominal stress at the pole is obtained:

$$s_{adj}=\frac{2\left(\lambda_{adj}^2-1\right)\left(a+b\lambda_{adj}^2\right)\left[a+2b+c+(2b+c)\lambda_{adj}^2+c\lambda_{adj}^4\right]}{\lambda_{adj}\left(a+2b\lambda_{adj}^2+c\lambda_{adj}^4\right)}, \tag{3.29}$$

with λ_{adj} given by Eq. (3.28). Fig. 3.7 shows the trend of stretch at the pole obtained from the numerical solution and the adjusted analytical stretch λ_{adj}. Note that for large values of β (0.1, 0.5 and 1) the stretch at the pole does not reach maximum value 7 because it is reached elsewhere in the membrane. With the calibration of λ_{adj} and s_{adj} some information regarding the state of strain and stress inside the membrane is provided. These information are limited to the pole of the membrane, but except particular cases this represents the more critical point of the domain.

3.3 Linearization to the infinitesimal strain theory

The analytical model developed in Section 3.1 considers large displacements and large deformations. Here, the proposed model is reduced to the linearized theory assuming that the components of both displacement field and displacement gradient are small [45]. The components of the right Cauchy-Green deformation tensor, expressed by Eq. (3.9), are developed in Taylor series as functions of α_0. The

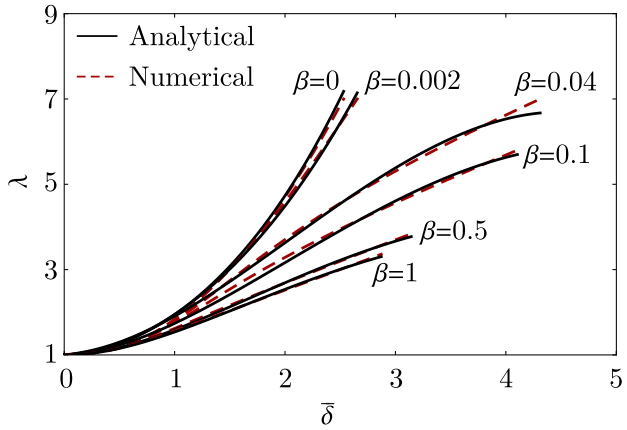

Figure 3.7: Stretch at the pole $\lambda_\Theta\big|_{R\to 0} = \lambda_R = \lambda$, expressed by Eq. (3.28), as a function of the deflection $\bar{\delta}$. The curves are given for different values of β. Continuous black lines are the adjusted analytical curves given by Eq.(3.28), calibrated from the actual curves obtained from the numerical solution of the TPBVP.

following expressions are obtained by truncating the series at the second order:

$$[\mathbf{C}] \cong \begin{bmatrix} \frac{1}{3}\left(\alpha_0^2+3\right) & 0 & 0 \\ 0 & \left(\frac{1}{3}-\frac{4R^2}{3L^2}\right)\alpha_0^2+1 & 0 \\ 0 & 0 & 1-\frac{2(b+c)\left(L^2-2R^2\right)\alpha_0^2}{3(a+2b+c)L^2} \end{bmatrix}. \tag{3.30}$$

The strain tensor of the linearized theory of elasticity is then computed as

$$[\mathbf{E}] = \frac{1}{2}[\mathbf{C}-\mathbf{I}] = \begin{bmatrix} \frac{\alpha_0^2}{6} & 0 & 0 \\ 0 & \frac{\left(L^2-4R^2\right)\alpha_0^2}{6L^2} & 0 \\ 0 & 0 & -\frac{(b+c)\left(L^2-2R^2\right)\alpha_0^2}{3(a+2b+c)L^2} \end{bmatrix}. \tag{3.31}$$

The linearization of stress tensor $\mathbf{S}$ provides

$$\begin{aligned} S_R &\cong \frac{2(a+b)\left[(a+4b+3c)L^2-4(b+c)R^2\right]\alpha_0^2}{3(a+2b+c)L^2} \\ S_\Theta &\cong \frac{2(a+b)\left[(a+4b+3c)L^2-4(a+3b+2c)R^2\right]\alpha_0^2}{3(a+2b+c)L^2}. \\ S_Z &= 0 \end{aligned} \tag{3.32}$$

It is immediate to verify that the linearized form of the Piola-Kirchhoff stress tensor $\mathbf{T_R}$ coincides with the linearized form of the Cauchy stress tensor $\mathbf{T} = (\det\mathbf{F})^{-1}\mathbf{T_R}\mathbf{F}^T$.

In linear elasticity, under the assumption of plain stress, the relations between stress and strain is given by Navier's inverse relationships

$$\begin{aligned}\sigma_R &= \frac{E}{1-\nu^2}\left(\epsilon_R + \nu\epsilon_\Theta\right),\\ \sigma_\Theta &= \frac{E}{1-\nu^2}\left(\epsilon_\Theta + \nu\epsilon_R\right),\end{aligned} \tag{3.33}$$

when σ and ϵ indicate the only measures of stress and strain in linear elasticity. Strain components ϵ_R and ϵ_Θ are given respectively by E_{11} and E_{22} of Eq. (3.31). By imposing the equivalence between the linearized stresses σ_R and σ_Θ and the corresponding components S_R and S_Θ, expressed by Eq. (3.32), a system of two equation is obtained. The system reads

$$\begin{aligned}&\frac{4(a+b)\left[L^2(a+4b+3c)-4R^2(b+c)\right]}{a+2b+c}+\frac{E\left[L^2(\nu+1)-4\nu R^2\right]}{\nu^2-1}=0,\\ &\frac{4(a+b)\left[L^2(a+4b+3c)-4R^2(a+3b+2c)\right]}{a+2b+c}+\frac{E\left[L^2(\nu+1)-4R^2\right]}{\nu^2-1}=0\end{aligned} \tag{3.34}$$

and from its solution the following expressions for the elastic constants of linear elasticity are obtained:

$$E=\frac{4(a+b)(a+4b+3c)}{a+3b+2c}, \qquad \nu=\frac{b+c}{a+3b+2c}. \tag{3.35}$$

The transversal strain component ϵ_Z in linear elasticity is expressed by

$$\epsilon_Z=-\frac{\nu}{E}\left(\sigma_R+\sigma_\Theta\right). \tag{3.36}$$

From Eqs. (3.35) and (3.32) it can be easily verified that the expression of ϵ_Z corresponds to component E_{33} of the strain tensor in Eq. (3.31).

Both Young's modulus E and Poisson's ratio ν of Eq. (3.35) correspond to those reported in [46] and [47]. In these two works, the authors analyzed respectively the finite bending of hyperelastic solids and the equilibrium of the von Mises truss in finite elasticity. In both works, a compressible Mooney-Rivlin material was adopted and the linearization of the theory allowed to derive the expressions of E and ν, which provide a link between the Mooney-Rivlin parameters and the elastic constants of linear elasticity. It is interesting to observe that, although the problems addressed by the authors involve different stress states, the expressions derived from the linearization correspond.

3.4 Validation of the proposed model

In this section the adjusted analytical formula for the pressure, given by Eq. (3.26), is validated. First, the adjusted formula is compared with the results of finite element simulations. Then, the simplified analytical solutions already available in the literature are introduced and it is shown how the proposed formula overcome the limitations of the existing models. Finally, compressible Mooney-Rivlin materials are considered and it is proved how the validity of the adjusted formula is easily extended to this class of materials.

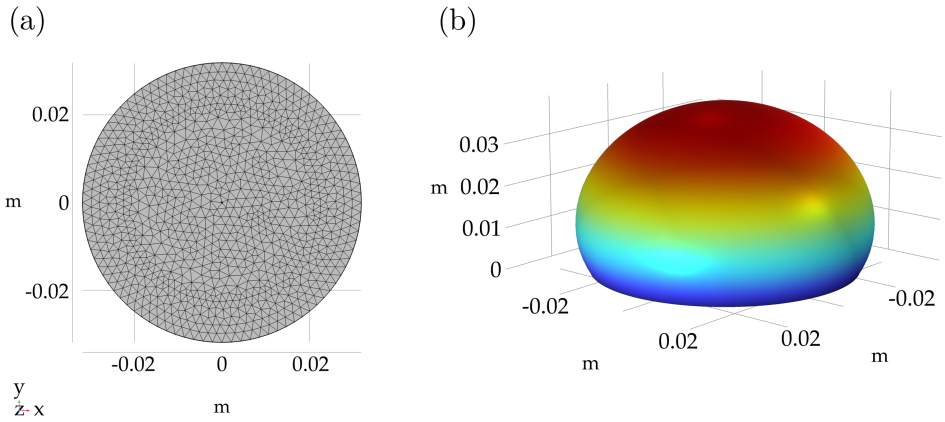

Figure 3.8: FE model of the inflated membrane created in COMSOL Multiphysics. (a) Meshed geometry of the membrane. (b) Deformed configuration after application of the uniform lateral pressure.

3.4.1 Finite element validation

The FE simulations are carried out in software COMSOL Multiphysics version 6.0. The 3D membrane interface of the structural mechanics module is used to build the model. The membrane element is a plane stress element in 3D that can deforms both in the in-plane and out-of-plane directions. Differently from shell elements, membrane elements do not have bending stiffness. Since field variables do not change over time, a stationary study is selected.

A circle with diameter $L = 65$ mm is created in the work plane, whereas the thickness of the membrane is set to $H = 1.5$ mm in the membrane settings. Note that the numerical values of L and H have no influence, since the results will be reported in terms of normalized quantities. The outer boundary is simply-supported by applying a fixed constraint to the edges of the membrane. The built-in two-parameter incompressible Mooney-Rivlin energy function is assigned as hyperelastic material. Parameter a is set to 1 MPa, while parameter b varies in order to consider different cases of ratio β. In particular, the following simulations are carried out: $b = 0$ MPa, $b = 0.1$ MPa, $b = 0.25$ MPa, $b = 0.5$ MPa and $b = 1$ MPa.

In the reference configuration, the membrane is flat and has zero transverse stiffness, generating a singularity. A tensile prestress is introduced through an external in-plane force of 10^{-4} N/m to overcome this issue. The sole purpose of the prestress is to allow the solver to find a solution. In fact, the prestress is negligible compared to the stress values acting on the membrane during the simulation. The membrane is then discretized in a fine mesh composed of triangular elements with size around 0.6 mm (Fig. 3.8(a)). Finally, a pressure load is applied to the free face and increased linearly in a quasi-static manner, inflating the membrane. In particular, the increasing values of applied pressure are defined as a list in the auxiliary sweep of the stationary analysis. Geometric nonlinearities are taken into account because large deformations are involved.

The MUMPS solver is used for the stationary analysis. The simulation stops at the last applied value of pressure or when a stationary value is reached. In this case, for further increasing values of pressure, convergence is not found anymore and the analysis stops. Fig. 3.8(b) shows the deformed configuration of the circular inflated membrane.

3.4.2 Analytical models from the literature

Only a few analytical solutions of the problem of inflated circular membranes can be found in the literature. All of them are based on simplifying assumptions on the kinematics or constitutive law. However, each of them is affected by limitations in correspondence of certain ranges of material parameters or deformation. In the following, these simplified models are introduced and compared with the proposed analytical formula. It is shown how the adjusted formula overcomes the limitations of the available models, being accurate for every range of deformation and material parameters.

Yuan et al. [48] have recently proposed a simplified solution for incompressible Mooney-Rivlin materials, assuming that the membrane deforms into a spherical cap. The expression of pressure as a function of deflection derived by Yuan et al. [48] is the following:

$$\bar{p}_{\text{Yuan}} = \frac{4\sin^7\alpha_0}{\alpha_0^6}\left(1+\beta\,\alpha_0^2\csc^2\alpha_0\right)\left(\alpha_0^6\csc^6\alpha_0-1\right), \tag{3.37}$$

with $\alpha_0 = 2\tan^{-1}\bar{\delta}$. This expression coincides with Eq. (3.22). This correspondence is not surprising, because both formulations are derived under the same assumption on the kinematics of the membrane.

Yang et al. [49] derived an analytical solution for pre-stretched inflated membranes for the case of neo-Hookean materials. Since the membrane is pre-stretched, both radial and circumferential stretches are assumed to be large. Therefore, following the approach of Foster [50], the authors assume that the term $\lambda_R^{-3}\lambda_\Theta^{-3}$ is negligible with respect to λ_R/λ_Θ and λ_Θ/λ_R. Under this assumption, the solution proposed in [49] is

$$\bar{p}_{\text{Yang}} = \frac{8\bar{\delta}}{1+\bar{\delta}^2}. \tag{3.38}$$

This solution gives an accurate description of the inflation of the membrane when deformations are large, but it is not suitable for the range of relatively small deformations.

The last solution considered is proposed by Fichter [51]. In this case, the author assumes a linear elastic model for the material. The equilibrium equations read

$$\begin{aligned} &N^2\left(\bar{R}^2\frac{d^2N}{d\bar{R}^2}+3\bar{R}\frac{dN}{d\bar{R}}\right)-\frac{1}{2}\bar{R}^3\frac{dN}{d\bar{R}}+\frac{1}{2}(3+\nu)\,\bar{R}^2N+\frac{1}{4}\frac{\bar{R}^2EH}{pL}=0,\\ &N\frac{d\bar{\delta}}{d\bar{R}}+\frac{1}{2}\bar{R}=0, \end{aligned} \tag{3.39}$$

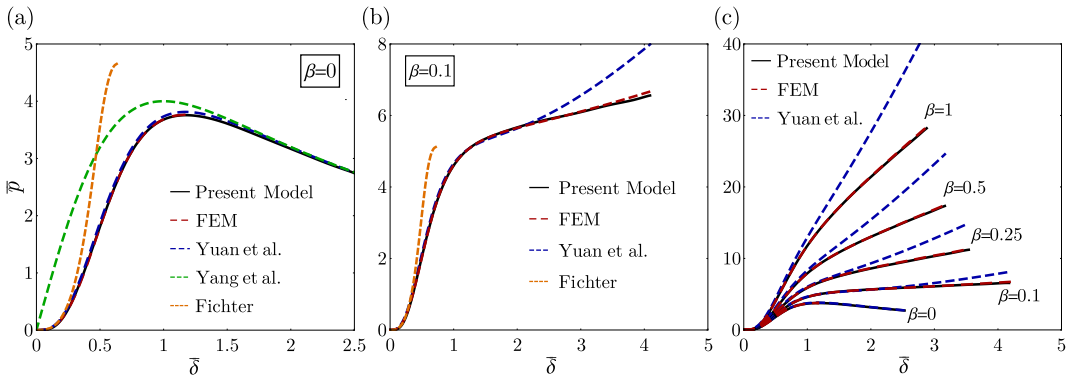

Figure 3.9: Normalized pressure $\bar{p} = pL/(aH)$ vs. normalized deflection at the pole $\bar{\delta} = \delta/L$. Comparison of pressure-deflection curves obtained with present analytical model (Eq. (3.26)), FE simulations and other solutions found in the literature: (a) Neo-Hookean material ($\beta = 0$); (b) Mooney-Rivlin material with $\beta = 0.1$; (c) variations of material parameter β.

where $\bar{R} = 2R/L$, E is the Young's modulus, ν is the Poisson's ratio and $N = 2N_{rr}/(pL)$, with N_{rr} indicating the radial stress resultant. The linear elastic model is a convenient choice due to its mathematical simplicity, but it is not appropriate to describe the inflation of rubberlike membranes, where deformations are expected to be very large. Moreover, in spite of the simplicity of such model, even in this case a closed-form solution for this problem is not available. Indeed, the solution for both stress resultant and deflection is found in the form of a power series

$$\begin{aligned} N\left(\bar{R}\right) &= \sum_{0}^{\infty} n_{2m} \bar{R}^{2m}, \\ \bar{\delta}\left(\bar{R}\right) &= \sum_{0}^{\infty} w_{2n} \left(1 - \bar{R}^{2n+2}\right). \end{aligned} \tag{3.40}$$

The expressions of the first six coefficients n_i and w_i of the power series for N and $\bar{\delta}$ are reported in [51]. In order to increase the accuracy of the solution, here the first twelve terms of both power series are considered. The procedure for the determination of coefficients n_i and w_i is outlined in [51].

3.4.3 Results and comparison

The adjusted pressure given by Eq. (3.26) is compared with the results of the finite element simulations and the simplified solutions described above in Fig. 3.9. The solution by Fichter [51] involves the elastic constants E and ν. These two constants are computed from Eq. (3.35), considering $c \to \infty$ since we are dealing with incompressible materials.

Figure 3.9(a) compares the solutions for the particular case of neo-Hookean material ($\beta = 0$). The prediction of the proposed model agrees perfectly with the solution given by the finite element model. In this case, the equilibrium path exhibits a softening branch after the maximum value of pressure. Since the FE analysis is carried

out in force control, the FE model is not able to capture this softening branch. As expected, the solution by Yang et al. given by Eq. (3.38) agrees well with the FE solution for large deformations, but it is completely wrong when the deflection is small. This is due to the simplifying hypothesis of assuming large stretches in the constitutive law. The solution proposed by Fichter is accurate only in the range of small deflections, namely less than one third of the radius of the membrane. For larger deflections, this solution results much stiffer than the others. This happens because the linear elastic model is not capable of capturing the nonlinearities in the material response arising for moderate and large deformations. The solution by Yuan et al., expressed by Eq. (3.37), is also quite accurate. This because when $\beta = 0$ the hypothesis of spherical caps is close to the actual deformed configurations (see Fig. 3.5(a)). However, as can be seen in Fig. 3.9(b), in case of $\beta = 0.1$ the solution by Yuan et al. is no longer accurate. In particular, as the deflection increases the discrepancy in the pressure curve increases, since the deformed shapes deviate more and more from spherical caps. The solution by Fichter suffer the same limitations as for $\beta = 0$, whereas the solution by Yang et al. is not reported because it is valid only for neo-Hookean materials. On the other hand, the proposed formula still perfectly agrees with the FE solution.

Finally, Fig. 3.9(c) compares the pressure-deflection curves obtained with our analytical model, the FE simulation and the formulation proposed by Yuan et al. for various values of β. For each value of β, the analytical model proposed in the present work gives a result that is in good agreement with the FE simulation. On the other hand, the solution by Yuan et al. can be considered accurate only for values of β that are very close to 0.

The results discussed above demonstrate that the proposed model overcomes the limitations of the current analytical solutions. Indeed, the adjusted analytical formula is capable of predicting the response of an inflated circular membrane composed of Mooney-Rivlin material regardless of the values of material parameters or the magnitude of deformation. On the other hand, current analytical solutions based on simplifying assumptions are reliable only for particular material properties or magnitude of deformation. For instance, the solution by Fichter is accurate only for small deformations, while the solution by Yang et al. only for very large deformations and neo-Hookean material.

3.4.4 Compressible materials

In Section 3.1 the simplified model for the inflation of circular membranes was developed for compressible Mooney-Rivlin materials, leading to the approximate expression of pressure given by Eq. (3.21). By computing the limit of Eq. (3.21) for $\gamma \to \infty$, the corresponding pressure for incompressible materials was derived. However, in Section 3.2 the adjustment of the pressure was carried out for the case of incompressible materials, fitting the numerical solution relative to incompressible materials. In this section it is shown how the adjusted pressure remains valid and accurate for compressible materials, provided Eq. (3.21) instead of Eq. (3.22) is used in Eq. (3.26). Essentially, the effect of compressibility is already taken into

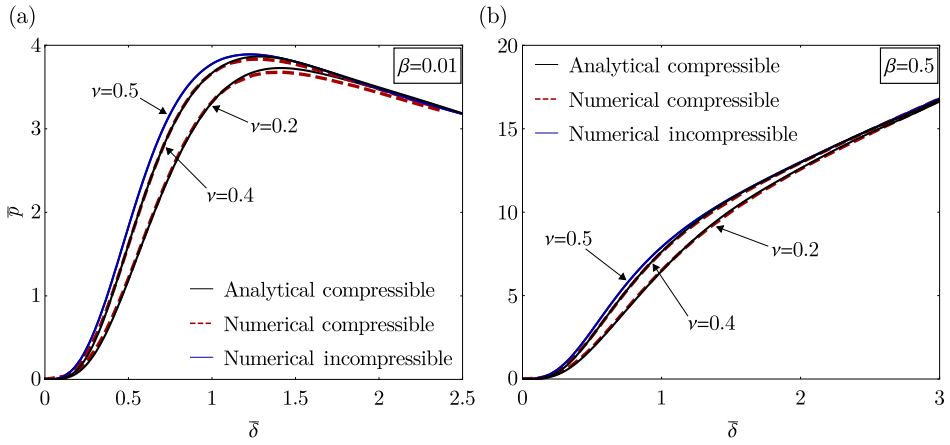

Figure 3.10: Pressure-deflection curves for compressible membranes: (a) $\gamma = 0.326$ ($\nu = 0.2$), $\gamma = 2.01$ ($\nu = 0.4$) and $\gamma \to \infty$ ($\nu = 0.5$) in the case of $\beta = 0.01$; (b) $\gamma = 0$ ($\nu = 0.2$), $\gamma = 2.5$ ($\nu = 0.4$) and $\gamma \to \infty$ ($\nu = 0.5$) in the case of $\beta = 0.5$. The analytical curve is obtained from Eq. (3.26), with $\bar{p}$ given by Eq. (3.21).

account in the analytical model and it does not affect the corrective polynomial. Therefore, the adjusted pressure for compressible materials is given by

$$\bar{p}_{adj}\left(\beta,\gamma,\bar{\delta}\right) = \bar{p}\sum_{j=1}^{10}\left(\frac{\bar{\delta}}{\bar{\delta}_{\max}}\right)^{j}\sum_{k=0}^{12} d_{jk}\beta^{k}, \tag{3.41}$$

with $\bar{p}$ given by Eq. (3.21). The effectiveness of Eq. (3.41) for compressible materials is proved in the following by a comparison with the reference numerical solution. The numerical solution for compressible Mooney-Rivlin materials was described in Sec. 2.4.2.

Fig. 3.10 shows the comparison between the numerical solution for compressible materials (red dashed lines) and the adjusted pressure given by Eq. (3.41) (continuous black lines). The continuous blue lines represent the numerical solution for incompressible materials, corresponding to $\nu = 0.5$.

Two values of β are considered, namely $\beta = 0.01$ and $\beta = 0.5$. These two cases allow to explore the effect of compressibility when softening and hardening behaviors take place. For each case, two values of parameter $\gamma = c/a$ are selected, such that Poisson's ratio ν equals 0.2 and 0.4. The Poisson's ratio is linked to the Mooney-Rivlin parameters through Eq. (3.35), which is rewritten as a function of only β and γ as

$$\nu = \frac{\beta+\gamma}{1+3\beta+2\gamma}. \tag{3.42}$$

From Fig. 3.10, it is evident how the analytical pressure given by Eq. (3.41) is in good agreement with the numerical solution for each case considered. This proves that the proposed analytical solution gives accurate predictions also in the most general case of compressible materials. It is worth noting that incompressible membranes are always stiffer than compressible ones. This behaviour may be explained

by the fact that incompressible solids can not undergo volume variations. In addition, Fig. 3.10 shows that compressibility mainly affects the moderate-to-large-strain region of the pressure curve and its impact is more significant for low values of β. Indeed, in the case of $\beta = 0.01$ significant differences are observed for low values of ν, particularly focused in the limit point region.

3.5 Experimental tests and material characterization

Several experimental tests have been carried out on circular flat membranes. For instance, Pamplona and Mota [52] investigated the inflation of a rubber membrane over a rigid and an elastic foundation. Jourdan et al. [53] performed bulge tests on a silicone membrane and proposed a semi-analytical method to evaluate the stress and strain around the pole. Machado [54] reconstructed the curvatures and the strain field during the inflation of a silicone membrane by means of 3D digital image correlation techniques. Suleman and Bosi [55] performed bulge tests on thin membranes made of an elastoplastic material.

In this section, uniaxial tensile tests and bulge tests are performed on three different kind of rubbers. Styrene butadiene rubber (SBR), latex rubber and silicone are considered as specimens. All the rubbers are available as sheets with of 1, 1 and 0.5 mm respectively. For each material, a set of optimal parameters is calibrated for both tests. The adjusted analytical pressure is used to characterize the material parameters based on the results of the bulge tests. In the following, the experimental tests are presented first. Then, the parameters of the Mooney-Rivlin model are calibrated by fitting the experimental results and the predictions given by the analytical model are compared with the experimental results.

3.5.1 Experimental tests

Three uniaxial tensile tests are carried out for each rubber. The dog-bone specimens have the same thickness of the rubber sheets, a width of 4 mm and an effective length of 40 mm. The tests are performed by using the materials testing apparatus ME-8236 produced by PASCO (Fig. 3.11). The machine has a built-in load cell (strain gauge transducer) capable of measuring up to 7100 N. An optical encoder module measures the displacement of the load bar. A crank gear raises or lowers the load bar on two translation screws. Force data from the load cell and displacement data from the encoder module are recorded, displayed and analyzed using the PASCO PASPORT Compatible Interface with the PASCO Data Collection Software. The sensor cable from the testing machine is connected to the PASPORT input port. Then, the USB link connected the PASCO Interface to a USB port on a laptop. Nominal stress and stretch are computed for each test.

After the uniaxial tensile tests, three bulge tests are carried out for each rubber. The setup of the tests is shown in Figs. 3.12(a) and 3.12(b). A steel plate with a circular hole in the center is supported by four pillars. The circular hole has diameter of 15 mm and the rubber membrane is placed above it. A striking plate is positioned on top to fix the membrane and a pressure is applied from above. As

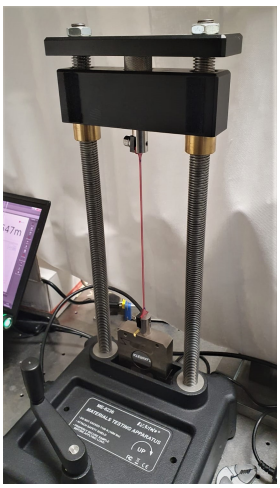

Figure 3.11: Set up of the uniaxial tensile test. The dog-bone specimen is fixed at the bottom and connected to the load bar at the top. A crank gear is used to raise the load bar and stretch the specimen. Force and displacement data are recorded.

shown in Fig. 3.12(c), the deflection of central point of the membrane is monitored with a laser placed at the bottom of the system. Fig. 3.12(d) shows the deformation of the membrane during the test.

An aluminium tank is pressurized by a low-pressure compressor using an air compression gun equipped with a one-way valve. The pressure inside the tank is measured using the pressure transmitter TR2101100 produced by Trafag International. The gauge has a 0-10 bar measuring range and precision of 0.03 bar. The pressure gauge is powered by a 24 V DC power supply unit. The output current signal is converted into the corresponding value of pressure with a 4-20 mA current loop operation. A 270 Ω resistor is inserted into the current path and a Rohde & Schwarz RTM3004 oscilloscope measures the voltage drop across the resistor with a sampling rate of 3.33 MSa/s.

The deflection of the inflated membrane is measured using the OPTO1420 laser sensor produced by Microepsilon. The sensor has a measuring range of 10-500 mm with a 0.01 mm precision. The deflection is also measured with a 4-20 mA current loop operation. The analogue voltage signals proportional to pressure and deflection are simultaneously acquired by the Rohde & Schwarz RTM3004 oscilloscope and exported as .csv files. The data files are then processed using MATLAB and the pressure-deflection curve is obtained.

3.5.2 Calibration of model parameters

The constitutive parameters of the Mooney-Rivlin material are initially calibrated for each rubber by fitting the data from the uniaxial tensile tests. The equilibrium equations governing the problem of a homogeneous, isotropic, compressible solid subjected to uniaxial traction are reported in A.1. In particular, Eq.(A.1) is an implicit relation which determines the lateral stretch for each value of the longitu-

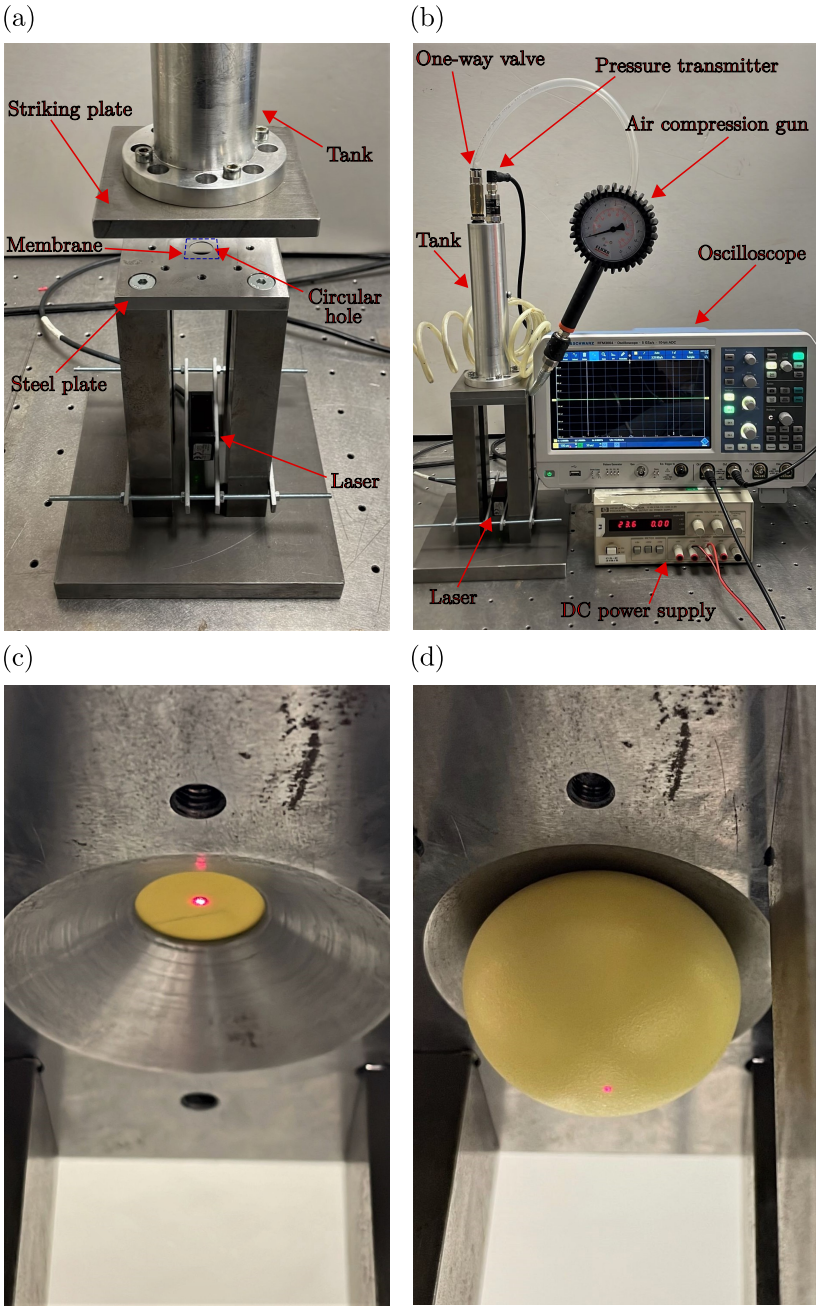

Figure 3.12: Set up of the bulge test on circular rubber membranes. (a) The membrane is placed over a circular hole in a steel plate. An upper striking plate is used to fix the membrane. The pressure is applied from above into an aluminum tank and it is measured with a pressure transmitter, as shown in (b). The deflection of the central point of the membrane is monitored with a laser placed at the bottom of the system. Figures (c) and (d) show, respectively, the membrane in initial configuration and after inflation.

Table 3.4: Mooney-Rivlin parameters calibrated by fitting experimental data from uniaxial and bulge tests.

	SBR	Latex	Silicone
a (MPa)	1.1	0.262	0.27
b (MPa)	0.1	0.014	0.033
β	0.091	0.053	0.122

dinal strech. Once known the lateral stretch, Equation (A.2) allows to compute the nominal tensile stress. Here, Eq. (A.2) is fitted to the experimental data from uniaxial tensile tests for each rubber using the *NonlinearModelFit* function of software Wolfram Mathematica.

Successively, the analytical pressure vs. deflection curve given by Eq. (3.41) is used to adjust the parameters in order to find a set which best fits also the results from bulge tests. This fitting is performed by means of *NonlinearModelFit* function of software Wolfram Mathematica. Table 3.13 lists the set of optimal parameters for each kind or rubber tested. The calibration of parameters a, b and c is done for all three specimens of each rubber. Since there is not much variability in the experimental responses, the average values are taken as final reference values. For each rubber specimen, the calibration gives as a result a very high value of parameter c, which means that Poisson's ratio ν is close to 0.5. Therefore, the rubbers analyzed are assumed incompressible for simplicity. As a consequence, only parameters a and b of the Mooney-Rivlin material need to be calibrated and Eq. (3.26) can be used to compute the analytical pressure vs. deflection curves. This assumption has the purpose to simplify the characterization of the material. However, in general, a proper investigation of material compressibility should involve the measurement of the actual volume changes occurring during deformation, as done in [56, 57]. Here, the assumption of incompressibility remains the most convenient approach for the purpose of demonstrating the effectiveness and usefulness of the propose formula.

Figure 3.13 shows the experimental uniaxial stress vs. strain curves and the analytical predictions. The Mooney-Rivlin model results very accurate for the SBR rubber, because it breaks at a stretch around 2 which is relatively small. The analytical prediction is acceptable also for latex rubber, even if some accuracy is lost for moderate strains. However, it is well know in the literature that the Mooney-Rivlin material model is not capable of describing strong hardening of polymers [41]. In fact, the calibrated analytical response for silicone is accurate only for stretches lower than 3. For larger stretches, silicone shows a very pronounced hardening and the material model is not capable of capturing such behavior. In light of this, an accurate modeling of the response of silicone requires a more refined constitutive law, such as those proposed by Ogden [58], Yeoh, [59], Gent [60] and Yeoh & Fleming [61]. A detailed discussion and analysis of such strain energy functions will be developed in Chapter 5 in order to select a refined strain energy function for accurate predictions of the response of elastomers. Nevertheless, for stretches less than 3 the analytical

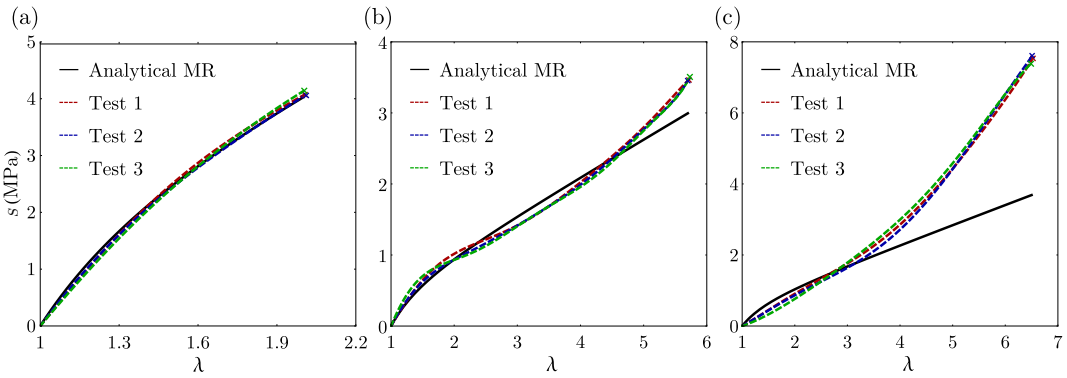

Figure 3.13: Experimental nominal stress s vs. longitudinal stretch λ from uniaxial tensile tests and fitting with Mooney-Rivlin constitutive law for (a) SBR, (b) latex and (c) silicone.

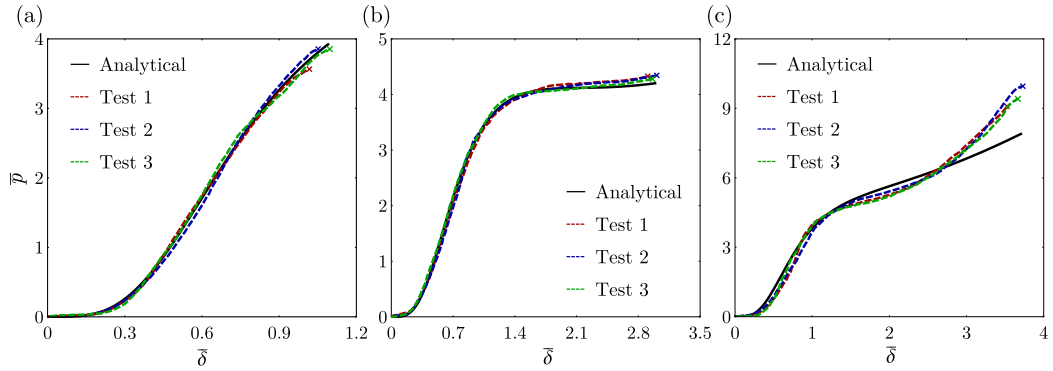

Figure 3.14: Pressure-deflection curves from bulge tests and comparison with analytical predictions for (a) SBR, (b) latex and (c) silicone. The analytical curves are obtained using Eq. (3.26) with the constitutive parameters listed in Tab. 3.4.

prediction of the Mooney-Rivlin model is accurate and allows to draw interesting conclusions and comparisons with the results of the bulge tests.

The experimental responses of the inflated circular membranes are shown in Fig. 3.14, along with the analytical predictions computed by Eq. (3.26). In case of SBR, the result of the bulge test also is in good agreement with the experimental data, since also the uniaxial response was accurately depicted by the Mooney-Rivlin law. Same goes for the latex rubber, with the exception of the final part of the curve with $\overline{\delta} > 2.5$. In accordance with the corresponding uniaxial response in Fig. 3.13(b), latex rubber shows a slight hardening that is not captured by the Mooney-Rivlin law. This is the reason of the gap between analytical prediction and experimental curve in Fig. 3.14(b). The bulge tests on silicone shows the same trend as the uniaxial tensile tests of Fig. 3.13(c). The analytical prediction of the inflation of the silicone membrane is accurate only until a deflection $\overline{\delta} \approx 2.5$. After this value hardening takes place and the Mooney-Rivlin model is not suitable anymore.

The uniaxial tensile test is the most common and practical test for material

characterization, due to its simplicity. Despite of this, it is important to remark that a correct characterization should consider the state of stress actually experienced by the material in practical applications. In this context, the bulge test represents an adequate and easy test to evaluate the material response under a biaxial stress state. To this purpose, the proposed formula was proved to be a powerful means for the calibration of the material parameters.

4 Approximate analytical solution for pre-stretched membranes

In Chapter 3 an analytical formula to compute the pressure curve of inflated circular membranes was proposed. The proposed formula has the advantage of being accurate for both compressible and incompressible Mooney-Rivlin materials, for every value of practical interest of the material parameters and for every magnitude of deformation. However, only unstretched membranes were considered.

In this Chapter, the proposed analytical formula is extended to pre-stretched membranes. Indeed, in engineering applications membranes are in most cases subjected to an in-plane homogeneous pre-stretch before inflation [62]. The presence of a pre-stretch gives an initial out-of-plane stiffness to the membrane and it often improves its performances [63, 64]. The combined effect of inflation and pre-stretch is of much interest in applications such as thermoforming [65] and soft robotics [66]. Considering these practical necessities, accurate analytical solutions regarding the inflation of pre-stretched membranes are of notable importance.

First, the simplified model proposed in Section 3.1 is extended to the case of pre-stretched, leading to an approximate expression for the pressure. Again, it is shown how the approximate solution loses accuracy for some values of material parameters and deformation. Following the approach of Chapter 3, the approximate pressure is then adjusted by fitting the numerical solution for incompressible Mooney-Rivlin materials. The pre-stretch causes significant qualitative changes in the deformed configurations, in the stretches profiles, as well as in the pressure curve. For this reason, the extension of the polynomial calibrated in Section 3.2 to the case of pre-stretched membranes is not straightforward. However, it is used as a starting point for the calibration of a new corrective polynomial which considers variations of pre-stretch and material parameter β. The adjusted formula is validated by finite element simulations and compared with the simplified solutions proposed in the literature. It is shown how the adjusted formula remains valid for compressible materials. Finally, experimental tests are carried out on pre-stretched membranes and the adjusted formula is applied to calibrate the material parameters.

4.1 Analytical model

In this Section, the simplified model based on the assumption of spherical deformed configurations is extended to the problem of pre-stretched membranes. As shown in Fig. 4.1, the kinematics is described by combining an initial uniform radial stretch and a subsequent inflation.

The circular flat membrane has radius L_0 and thickness H in the undeformed configuration. The membrane is first axisymmetrically stretched radially and L indicates the final radius, as shown in Fig. 4.1(a). The amount of pre-stretch is

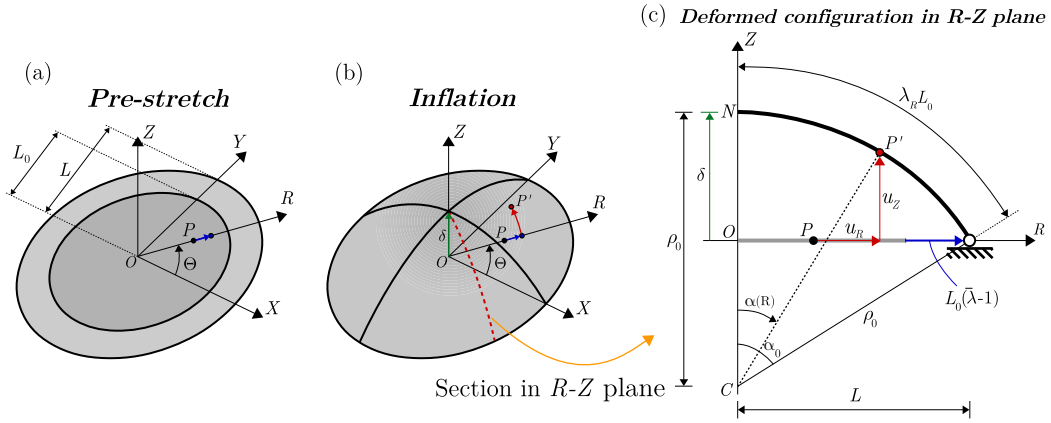

Figure 4.1: Kinematics of the pre-stretched membrane under uniform lateral pressure p. (a) The membrane is first subjected to a radial pre-stretch $\bar{\lambda} = L/L_0$ and then (b) inflated by a lateral pressure. The cylindrical coordinates (R, Θ, Z) are used as reference system. (c) The deformed membrane preserves the axial symmetry and thus the deformation is described for a generic section in the R-Z plane. After pre-stretch and inflation, a point P moves to P'. The displacement components are u_R and u_Z. The membrane deforms into a spherical cap with radius ρ_0 and central angle α_0. Parameter α_0 governs the kinematics. The deflection δ is linked to α_0 by the relation $\alpha_0 = 2\tan^{-1}(\delta/L)$.

given by the ratio $\bar{\lambda} = L/L_0$. In the following, the final length L will be held fixed and the pre-stretch will be changed by varying the initial length L_0. The radial stretch $\bar{\lambda}$ is accompanied by a circumferential stretch again equal to $\bar{\lambda}$. Therefore, after the application of the pre-stretch, the membrane results in an homogeneous, equibiaxial stress state.

The membrane is then inflated by a uniform lateral pressure p, as shown in Fig. 4.1(b). A generic material point $P \equiv (R, \Theta, 0)$ moves to P', with coordinates (R', Θ, Z'). The deformed configuration is assumed as a spherical cap. The kinematics deriving from this hypothesis is described in Fig. 4.1(c). The displacement field is again given by Eqs (3.1), with ρ_0 and $\alpha(R)$ now given by

$$\rho_0 = \frac{\bar{\lambda} L_0}{\sin\alpha_0}, \qquad \alpha(R) = \frac{\alpha_0 R}{L_0}. \tag{4.1}$$

The deformation gradient reads

$$[\mathbf{F}] = \begin{bmatrix} \rho_0 \dfrac{\partial \alpha}{\partial R}\cos\alpha & 0 & \lambda_Z \sin\alpha \\ 0 & \dfrac{\rho_0 \sin\alpha}{R} & 0 \\ -\rho_0 \dfrac{\partial \alpha}{\partial R}\sin\alpha & 0 & \lambda_Z \cos\alpha \end{bmatrix}, \tag{4.2}$$

where

$$\lambda_R = \rho_0 \frac{\partial \alpha}{\partial R} = \frac{\bar{\lambda}\alpha_0}{\sin\alpha_0}, \qquad \lambda_\Theta = \frac{\rho_0 \sin\alpha}{R} = \frac{\bar{\lambda} L_0 \sin\alpha}{R \sin\alpha_0}, \tag{4.3}$$

are the principal stretches in the meridian and circumferential directions.

The first Piola-Kirchhoff $\mathbf{T}_R$ stress tensor is computed following Eq. (3.10). Assuming the compressible Mooney-Rivlin material model given by Eq. (2.26), the components of the Biot stress tensor $\mathbf{S}$ coincide with Eq. (3.14). Imposing $S_Z = 0$ to satisfy the membrane assumption, the transversal stretch λ_Z assumes the following expression

$$\lambda_Z = \sqrt{\frac{a+2b+c}{a+2b\,\alpha_0^2\bar{\lambda}^2\csc^2\alpha_0 + c\,\alpha_0^4\bar{\lambda}^4\csc^4\alpha_0}}. \tag{4.4}$$

As expected, for $\bar{\lambda}=1$, Eq. (3.20) for unstretched membranes is retrieved. The local equilibrium at the pole of the membranes, for $R\to 0$, leads again to Eq. (3.18). In the presence of a pre-stretch, the normalized pressure for a compressible Mooney-Rivlin material reads [67]

$$\bar{p} = \frac{4\sin^3\alpha_0\left(\alpha_0^2\bar{\lambda}^2\csc^2\alpha_0-1\right)\left(1+\beta\,\alpha_0^2\bar{\lambda}^2\csc^2\alpha_0\right)\left[1+2\beta+\alpha_0^2\bar{\lambda}^2\csc^2\alpha_0(2\beta+\gamma)+\gamma\left(1+\alpha_0^4\bar{\lambda}^4\csc^4\alpha_0\right)\right]}{\alpha_0^2\bar{\lambda}^2\left(1+2\beta\,\alpha_0^2\bar{\lambda}^2\csc^2\alpha_0+\gamma\,\alpha_0^4\bar{\lambda}^4\csc^4\alpha_0\right)}. \tag{4.5}$$

Computing the limit of Eq. (4.5) for $\gamma\to\infty$, the expression for incompressible materials is found

$$\bar{p}\big|_{\gamma\to\infty} = \frac{4\sin^7\alpha_0}{\alpha_0^6\bar{\lambda}^6}\left(1+\beta\,\alpha_0^2\bar{\lambda}^2\csc^2\alpha_0\right)\left(\alpha_0^6\bar{\lambda}^6\csc^6\alpha_0-1\right) \tag{4.6}$$

For $\bar{\lambda}=1$, Eq. (4.5) and Eq. (4.6) reduce respectively to Eq. (3.21) and Eq. (3.22) valid for unstretched membranes. Again, in case of incompressible materials, the normalized pressure depends only on material parameter β, whereas it is indipendent of the geometrical parameters of the membrane.

Figure 4.2 shows the comparison between the approximate pressure given by Eq. (4.6) and the numerical solution for pre-stretched membranes. The results are shown for two values of pre-stretch, $\bar{\lambda}=1.5$ and $\bar{\lambda}=2$, and for different values of β. The analytical solution is accurate only for small deformations, due to the simplifying assumption on the kinematics. As the deformation increases, the discrepancy between the analytical and numerical solution increases. The errors are more pronounced for high values of β, since the deformed shapes turn away from the spherical assumption. As happened for unstretched membranes, Figure 4.2 remarks the need of an adjustment to the proposed model in order to obtain an analytical formula with a wide range of validity. The adjustment is performed in the next section by fitting the numerical solution of the problem.

4.2 Adjustment of the pressure curves

In the case of unstretched membranes, the adjusted expression for the pressure read

$$\bar{p}_{adj}\left(\beta,\bar{\delta}\right) = \bar{p}\big|_{\gamma\to\infty}\left(\beta,\bar{\delta}\right)F\left(\beta,\bar{\delta}\right), \tag{4.7}$$

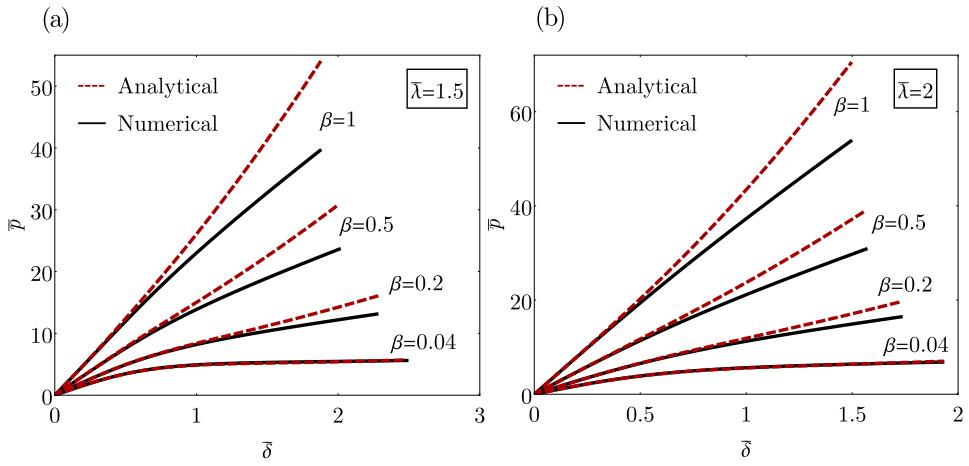

Figure 4.2: Normalized pressure $\bar{p} = pL/(aH)$ vs. normalized deflection at the pole $\bar{\delta} = \delta/L$ for different values of β. The plots refers to incompressible materials for (a) $\bar{\lambda} = 1.5$ and (b) $\bar{\lambda} = 2$. As in the case of unstretched membranes, the approximate analytical solution results accurate only for small deformation, while it exhibits significant errors at large deformations. The errors increase as parameter β increases.

where $F\left(\beta, \bar{\delta}\right)$ is a polynomial function given by

$$F\left(\beta, \bar{\delta}\right) = \sum_{j=1}^{10} \frac{\bar{\delta}^j}{\bar{\delta}_{max}(\beta)} \sum_{k=0}^{12} d_{jk} \beta^k. \tag{4.8}$$

Coefficients d_{jk} were calibrated fitting the numerical solution and are reported in Tab. 3.2. Being calibrate for the special case $\bar{\lambda} = 1$, this polynomial is no longer valid when an initial pre-stretch is applied to the membrane. The presence of a pre-stretch causes significant differences in the response of the membrane. A simplifying approach [67] to generalize Eq. (3.26) to the case of pre-stretched membranes is translating the argument in $F(\beta, \bar{\delta})$ to $F(\beta, \bar{\delta} + \Delta\bar{\delta})$. This approach is based on the qualitative idea that a point computed at $F(\beta, \bar{\delta} + \Delta\bar{\delta})$ on the fitted polynomial corresponds to a more demanding state with respect to point $F(\beta, \bar{\delta})$. The value of $\Delta\bar{\delta}$ can be determined so that the increment in the stress state in the interval $F(\beta, \bar{\delta} + \Delta\bar{\delta})$ - $F(\beta, \bar{\delta})$ corresponds on average to the pre-stress caused by the pre-stretch $\bar{\lambda}$. In general, the increment $\Delta\bar{\delta}$ depends on the values of β and $\bar{\lambda}$. Therefore, a value for $\Delta\bar{\delta}$ must be determined for each combination of β and $\bar{\lambda}$, namely $\Delta\bar{\delta} = \Delta\bar{\delta}(\beta, \bar{\lambda})$. Despite being not rigorous from a mechanical point of view, this approach simplifies considerably the fitting procedure preserving a good accuracy.

As further simplication, it is assumed that $\Delta\bar{\delta}$ can be expressed as product of two separate functions of β and $\bar{\lambda}$, namely

$$\Delta\bar{\delta}\left(\beta, \bar{\lambda}\right) = \phi(\beta)\, \psi\left(\bar{\lambda}\right). \tag{4.9}$$

This assumption corresponds to the intuitive idea that the dependency of function $\Delta\bar{\delta}$ on β does not change qualitatively for different values of pre-stretch, but only

Table 4.1: Optimal coefficients of the polynomial function $\phi(\beta)$, calibrated by fitting the discrete values ϕ_i.

b_0	b_1	b_2	b_3	b_4	b_5	b_6
b_7	b_8	b_9	b_{10}	b_{11}	b_{12}	
1.08	40.19	-620.1	2211.96	1.69×10^4	-1.99×10^5	9.14×10^5
-2.42×10^6	4.07×10^6	-4.40×10^6	2.97×10^6	-1.15×10^6	1.92×10^5	

by a scaling factor. This allows to study the dependence from β for a fixed value of pre-stretch, and to calibrate the function $\psi(\bar{\lambda})$ subsequently. For simplicity, function $\phi(\beta)$ is calibrated for the case $\bar{\lambda}=2$. Thus, function $\psi(\bar{\lambda})$ results a monotonic function defined in [1,2] with values in [0,1]. For $\bar{\lambda}=2$, $\psi(2)=1$ and $\Delta\bar{\delta}(\beta,2)=\phi(\beta)$, while for $\bar{\lambda}=1$, $\psi(1)=0$, $\Delta\bar{\delta}(\beta,1)=0$ and the expression for unstretched membranes, Eq. (3.26), is retrieved.

Therefore, the case of $\bar{\lambda}=2$ is considered first. The values considered for parameter β are the same considered in Section 3.2, namely 70 discrete values ranging in [0,1]. For each value of β_i, $i=1,...,70$, the optimal values ϕ_i are determined so that $\bar{p}_{\text{adj}}(\beta_i,\bar{\delta})=\bar{p}(\beta_i,\bar{\delta})\,F(\beta_i,\bar{\delta}+\phi_i)$ best fits the numerical solution. Successively, function *NonlinearModelFit* of Wolfram Mathematica is employed to find the best fitting function $\phi\,(\beta)$ for the discrete values ϕ_i. Assuming a polynomial expression

$$\phi\,(\beta)=\sum_{k=0}^{12} b_k\beta^k, \tag{4.10}$$

NonlinearModelFit determines the set of parameters b_k that best fits the discrete values of ϕ_i based on a least-square approach. The optimal coefficients b_k are given in Tab. 4.1. Finally, the influence of pre-stretch $\bar{\lambda}$ is studied. Regarding the range of variability of $\bar{\lambda}$, 10 values ranging from 1 to 2 with step 0.1 are considered. Values of pre-stretch greater than 2 exceed the range of practical interest. Again, the optimal values ψ_j, $j=1,..,10$, are determined so that

$$\bar{p}_{\text{adj}}\left(\bar{\lambda}_j,\beta,\bar{\delta}\right)=\bar{p}\left(\bar{\lambda}_j,\beta,\bar{\delta}\right)\,F\left(\beta,\bar{\delta}+\psi_j\,\phi\,(\beta)\right) \tag{4.11}$$

best fits the numerical solutions for each $\bar{\lambda}_j$ and *NonlinearModelFit* is applied again to determine the best fitting function of the form

$$\psi\left(\bar{\lambda}\right)=\sum_{k=0}^{3} l_k\bar{\lambda}^k. \tag{4.12}$$

The estimated coefficients l_k are listed in Tab. 4.2. The optimal values ϕ_i and ψ_j and the fitting functions $\phi(\beta)$ and $\psi(\bar{\lambda})$ are shown in Fig 4.3. Overall, the adjusted analytical pressure assumes the following form

$$\bar{p}_{\text{adj}}\left(\bar{\lambda},\beta,\bar{\delta}\right)=\bar{p}\left(\bar{\lambda},\beta,\bar{\delta}\right)\,F\left(\beta,\bar{\delta}+\psi\left(\bar{\lambda}\right)\,\phi\,(\beta)\right). \tag{4.13}$$

Table 4.2: Optimal coefficients of the polynomial function $\psi(\bar{\lambda})$, Eq. (4.12), calibrated by fitting the discrete values ψ_j.

l_0	l_1	l_2	l_3
-4.92	8.34	-4.16	0.73

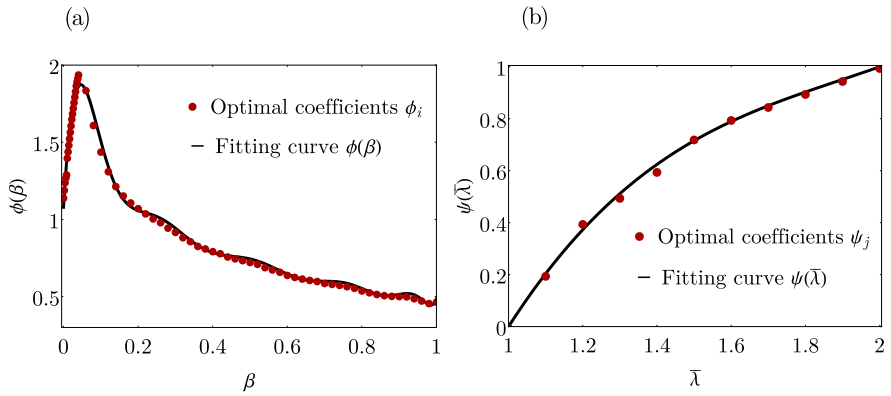

Figure 4.3: (a) Optimal coefficients ϕ_i for the discrete values β_i (red dots) and fitting curve $\phi(\beta)$ (continuous line) and (b) optimal coefficients ψ_j for the discrete values $\bar{\lambda}_i$ (red dots) and fitting curve $\psi(\bar{\lambda})$ (continuous line).

Figure 4.4 compares the adjusted analytical formula with the numerical solution of pre-stretched membranes. The plots are given for $\beta = 0.04, 0.2, 0.5, 1$ and for each β the values of pre-stretch $\bar{\lambda} = 1, 1.2, 1.5, 2$ are considered. The adjusted analytical pressure results accurate for each value of parameter β and pre-stretch $\bar{\lambda}$.

It is important to remark the wide range of validity of Eq. (4.13). Indeed, the normalized pressure is indipendent from the constitutive parameter a as well as from the geometrical quantities L and H of the membrane. A variation of these parameters only causes a scaling in the dimensional value of pressure. Moreover, due to the wide ranges considered for β and $\bar{\lambda}$, Eq. (4.13) covers most cases of practical interest.

4.3 Validation and discussion

The adjusted pressure calibrated for pre-stretched membranes is first validated by FE simulations. Several values of material parameter β and pre-stretch $\bar{\lambda}$ are considered. Successively, some considerations on the particular class of incompressible neo-Hookean membranes ($\beta = 0$) are drawn. Finally, the adjusted formula is extended to compressible Mooney-Rivlin materials and a conclusive discussion on the limitations of the material models employed are drawn.

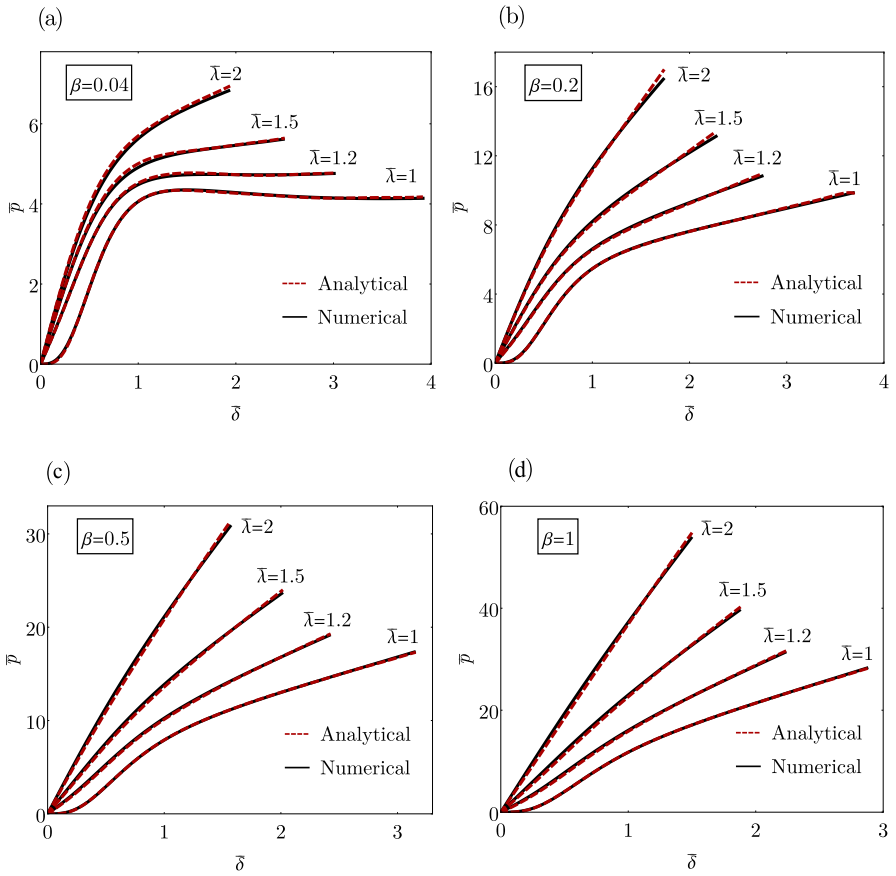

Figure 4.4: Normalized pressure $\bar{p} = pL/(aH)$ vs. deflection $\bar{\delta} = \delta/L$ curves for different levels of pre-stretch $\bar{\lambda}$: (a) case of $\beta = 0.04$, (b) case of $\beta = 0.2$, (c) case of $\beta = 0.5$ and (d) case of $\beta = 1$. The analytical curves (red dashed lines) are given by Eq. (4.13).

4.3.1 Finite element validation

The FE simulations are carried out in COMSOL Multiphysics® version 6.0 and follow similarly the procedure described in Section 3.4.1. Firstly, the geometry of the undeformed membrane is defined by creating a *work plane* in the *3D Component*. The stretched diameter L and thickness H of the membrane are fixed to 100 mm and 1 mm, respectively. The initial diameter L_0 is assigned so that $L/L_0 = \bar{\lambda}$. The *Membrane* interface of the *Structural Mechanics* module is selected as the *Physics* for the model. A two-parameters Mooney-Rivlin incompressible material is selected in the *Hyperelastic Material* menu of the *Membrane* interface. Parameter a is set to 1 MPa, while parameter b varies in order to consider different cases of ratio β. In particular, for each value of pre-stretch four cases of β are considered: $\beta = 0.04$ MPa, $\beta = 0.2$ MPa, $\beta = 0.5$ MPa and $\beta = 1$ MPa. The outer boundary of the membrane is simply supported. The pre-stretch $\bar{\lambda}$ is enforced by assigning a prescribed radial displacement to the outer boundary of the membrane. Two values of $\bar{\lambda}$ are consid-

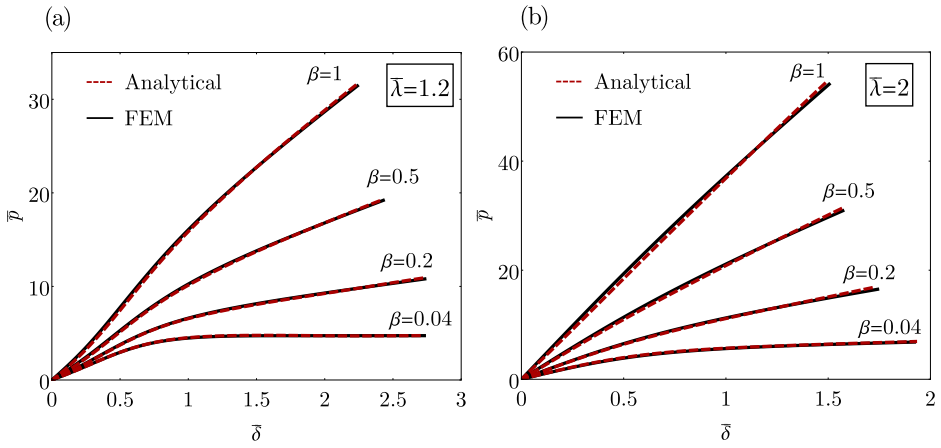

Figure 4.5: Normalized pressure $\bar{p} = pL/(aH)$ vs. deflection $\bar{\delta} = \delta/L$ curves given by FE simulations (continuous black lines) and by Eq. (4.13) (red dashed lines) for different values of β: (a) case of $\bar{\lambda} = 1.2$ and (b) case of $\bar{\lambda} = 2$.

ered, $\bar{\lambda} = 1.2$ and $\bar{\lambda} = 2$. Note that the geometry of the membrane has no influence on the results, since they will be reported in terms of normalized quantities. The lateral pressure is applied as a *Face Load* on one side of the membrane. Finally, the membrane is discretized in a fine mesh with element size of the order of 0.6 mm and a *Stationary Study* was created. The pressure was increased in a quasi-static manner considering geometric nonlinearities.

The results of the FE simulations are compared with adjusted analytical pressure in Fig. 4.5. The results provided by the FE simulations confirm the accuracy of the adjusted pressure for pre-stretched membranes in the entire ranges of deformation and constitutive parameters considered.

4.3.2 Neo-Hookean material

The case of $\beta = 0$ corresponds to a neo-Hookean material model. In this case, the numerical simulation show that the deformed configurations tend to spherical caps for increasing values of the pre-stretch $\bar{\lambda}$. For this reason, as $\bar{\lambda}$ increases the simplified model described in Section 3.4.1 becomes more and more accurate. As a result, the approximate pressure given by Eq. (4.6) is sufficient to describe the pressure-deflection relation for incompressible neo-Hookean pre-stretched membranes, as shown in Fig. 4.6. This result is consistent with the model proposed by Yang et al. [49], where the authors derived an analytical solution for incompressible neo-Hookean membranes under very large deformations. The following expression for the normalized pressure was obtained:

$$\bar{p}_{\text{Yang}} = \frac{8\bar{\delta}}{1+\bar{\delta}^2}. \tag{4.14}$$

Figure 4.6 shows that approximate pressure in Eq. (4.6) matches perfectly the numerical solution even for small values of pre-stretch. On the contrary, as shown

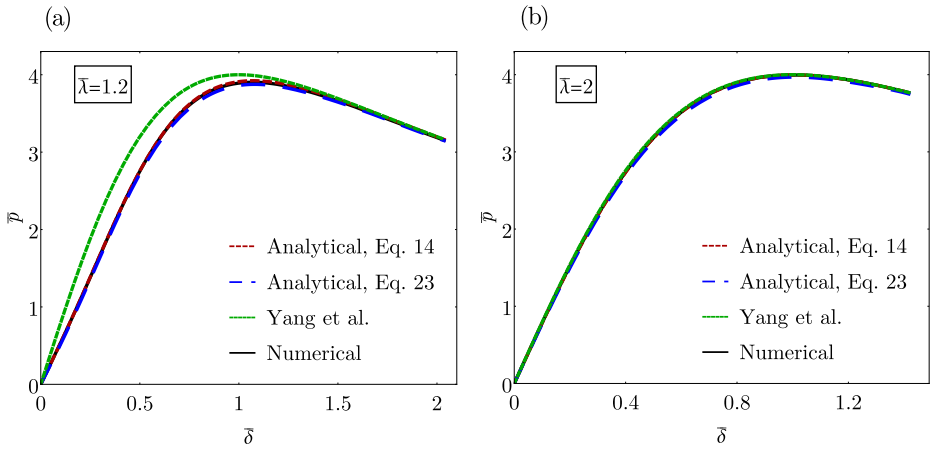

Figure 4.6: Normalized pressure $\bar{p} = pL/(aH)$ vs. deflection $\bar{\delta} = \delta/L$ curves for Neo-Hookean membranes ($\beta = 0$): (a) case of $\bar{\lambda} = 1.2$ and (b) case of $\bar{\lambda} = 2$. In case of Neo-Hookean materials, both the approximate pressure, Eq. 14, and the adjusted pressure, Eq. 23, result accurate. The green dashed lines represent the solution proposed by Yang et al., which is accurate only for large values of pre-stretch $\bar{\lambda}$.

in Fig. 4.6(a), the solution proposed by Yang et al. is not accurate for $\bar{\lambda} = 1.2$ in the range of small to moderate deformation.This is due to the assumption of very large deformations, which allowed the authors to neglect terms in the constitutive law and to derive a closed-form solution. For $\bar{\lambda} = 2$, as shown in Fig. 4.6(b), it results accurate in the entire range of deformation since the strain is already sufficiently large.

It goes without saying that, even if Eq. (4.6) is sufficient to properly describe the response of Neo-Hookean membranes, the final adjusted expression given by Eq. (4.13) is accurate as well, as clarified by Fig. 4.6.

4.3.3 Compressible materials

The adjusted pressure in Eq. (4.13) was calibrated by fitting the numerical simulation for incompressible Mooney-Rivlin materials. In the same manner as for unstretched membranes, it is shown that the corrective polynomial is valid also for compressible materials, provided that the approximate pressure for compressible materials given by Eq. (4.5) is used in place of Eq. (4.6). Namely, the adjusted pressure for compressible Mooney-Rivlin materials reads

$$\bar{p}_{\text{adj}}\left(\bar{\lambda}, \beta, \gamma, \bar{\delta}\right) = \bar{p}\, F\left(\beta, \bar{\delta} + \psi\left(\bar{\lambda}\right)\phi\left(\beta\right)\right), \tag{4.15}$$

with $\bar{p}$ given by Eq. (4.5). Again, the compressibility is already taken into account by the analytical model.

Figure 4.7 compares the analytical curves given by Eq. (4.15) with the numerical solution for compressible materials. The plots are given for $\bar{\lambda} = 1.2$ and for two values of β, namely $\beta = 0.004$ and $\beta = 0.1$. For each plot two values of parameter γ are

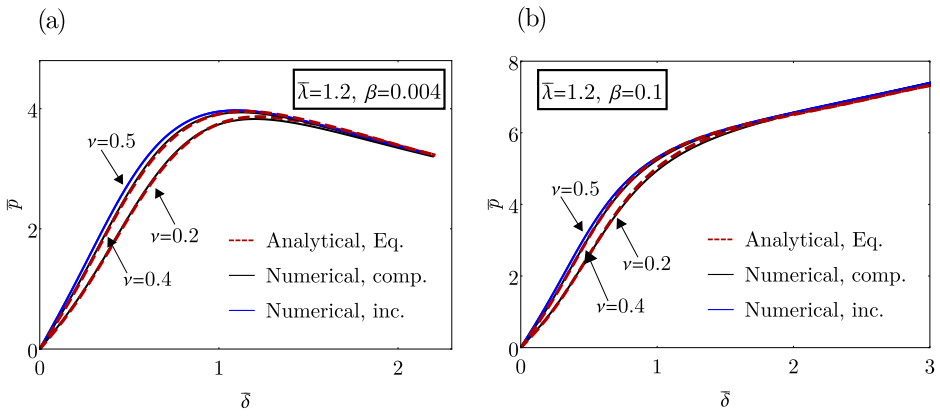

Figure 4.7: Pressure-deflection curves for compressible Mooney-Rivlin membranes with pre-stretch $\bar{\lambda} = 1.2$: (a) $\gamma = 0.33$ ($\nu = 0.2$) and $\gamma = 2.004$ ($\nu = 0.4$) for the case of $\beta = 0.004$; (b) $\gamma = 0.27$ ($\nu = 0.2$) and $\gamma = 2.1$ ($\nu = 0.4$) for the case of $\beta = 0.1$. The analytical pressure reproduces accurately the numerical solution for compressible materials. As ν decreases, significant differences between compressible and incompressible models appear in the first branch of the curve.

selected, so that Poisson's ratio ν equals 0.2 and 0.4. Poisson's ratio is linked to the Mooney-Rivlin constitutive parameters by Eq. (3.35). Red dashed lines represent the numerical solution for compressible materials and continuous blue lines represent the numerical solution for incompressible materials ($\nu = 0.5$).The analytical pressure perfectly matches with the numerical solution for compressible materials.

Similarly to the case of unstretched membranes, as ν decreases discrepancies between compressible and incompressible models appear and concentrate in the range of moderate deformations, where the increasing branch of the curve takes place regardless of the values of the material parameters. It is important to highlight that a value of Poisson's ratio equal to 0.2 is not realistic for elastomers. However, such value may be appropriate for advanced materials like polymeric foams and gels, which nowadays receive an increasing attention in membrane applications. As demonstrated by Fig. 3.10 and Fig. 4.7, when such materials are considered, the effect of material compressibility has a significant impact on the response of inflated membranes and it can not be neglected.

The discrepancies observed in Fig. 4.7 highlight the impact of compressibility for materials capable of experiencing volume changes. However, the formulation of compressibility adopted so far suffers of two main limitations:

(i) the strain energy function is not split into deviatoric and volumetric components. The split of the SED allows an indipendent description and characterization of the volumetric response of the material, given by the volumetric part of the SED. Without this approach, all the parameters involved in the SED are responsible of the volumetric response, making impossible a physical investigation on the real volumetric response of the material;

(ii) the function proposed by Ciarlet & Geymonat [36] was adopted to incorporate

volume variations into the strain energy function. This choice was due to its mathematical simplicity. Indeed, its mathematical simplicity allows to determine an explicit relation for the transversal stretch. However, this function is not capable of accurately describe the actual response of elastomers, foams and gels to large volume changes.

These limitiations underscore the importance of a detailed analysis regarding the real volumetric response of elastomers. To this aim, in Chapter 5 the actual volumetric response of elastomers to volumetric deformations is carefully investigated experimentally and a proper strain energy function for large volumetric deformations of elastomers is proposed.

4.4 Experimental tests and material characterization

Only a few experimental tests on pre-stretched membranes have been carried out. Amabili et al. [68] performed static and dynamic tests on a thin squared silicone rubber plate. Fox and Goulbourne [14, 69] tested the vibrations of elastomer membranes under electromechanical loading. To fill this void, a series of experimental tests on pre-stretched membranes is carried out. In particular, bulge tests are performed on three different rubber sheets considering moderate values of pre-stretch. NBR rubber, silicone and NR rubber are the three kinds of rubber considered, with thickness of 2, 2 and 1.5 mm respectively. In the following, the setup of the bulge tests is presented and the adjusted analytical pressure is used for the calibration of the Mooney-Rivlin material parameters for each rubber.

4.4.1 Bulge tests

The setup of the tests is shown in Fig. 4.8. The initially flat circular membrane is inserted into two steel rings that are tightened so that the membrane results fixed. The membrane is placed on a circular steel plate supported by four pillars. The steel plate has a circular hole in the center, with diameter of 15 mm. The rings can slide along four screwed rods, allowing the application of a pre-stretch to the membrane. In particular, the value of pre-stretch is set by regulating the position of the rings using 4+4 nuts, placed below and over the rings.

A perforated striking plate is positioned on the membrane. The striking plate is connected to an aluminum tank inside which the external pressure is applied. An hydraulic press is used to push the striking plate against the steel plate and thus avoiding pressure losses. The aluminium tank is pressurized by a low-pressure compressor using an air compression gun equipped with a one-way valve.

A pressure reducing valve is used to obtain an applied pressure rate of 0.1 bar/s. The pressure inside the tank is measured using the pressure transmitter TR2101100 produced by Trafag International. The deflection of the central point of the membrane is monitored with the OPTO1420 laser sensor produced by Microepsilon, which is placed at the bottom of the system. The pressure transmitter has an accuracy of 0.04 MPa, whereas the laser sensor has a repeteability of 0.5 μm. The output current signal of both laser sensor and pressure gauge are converted into the

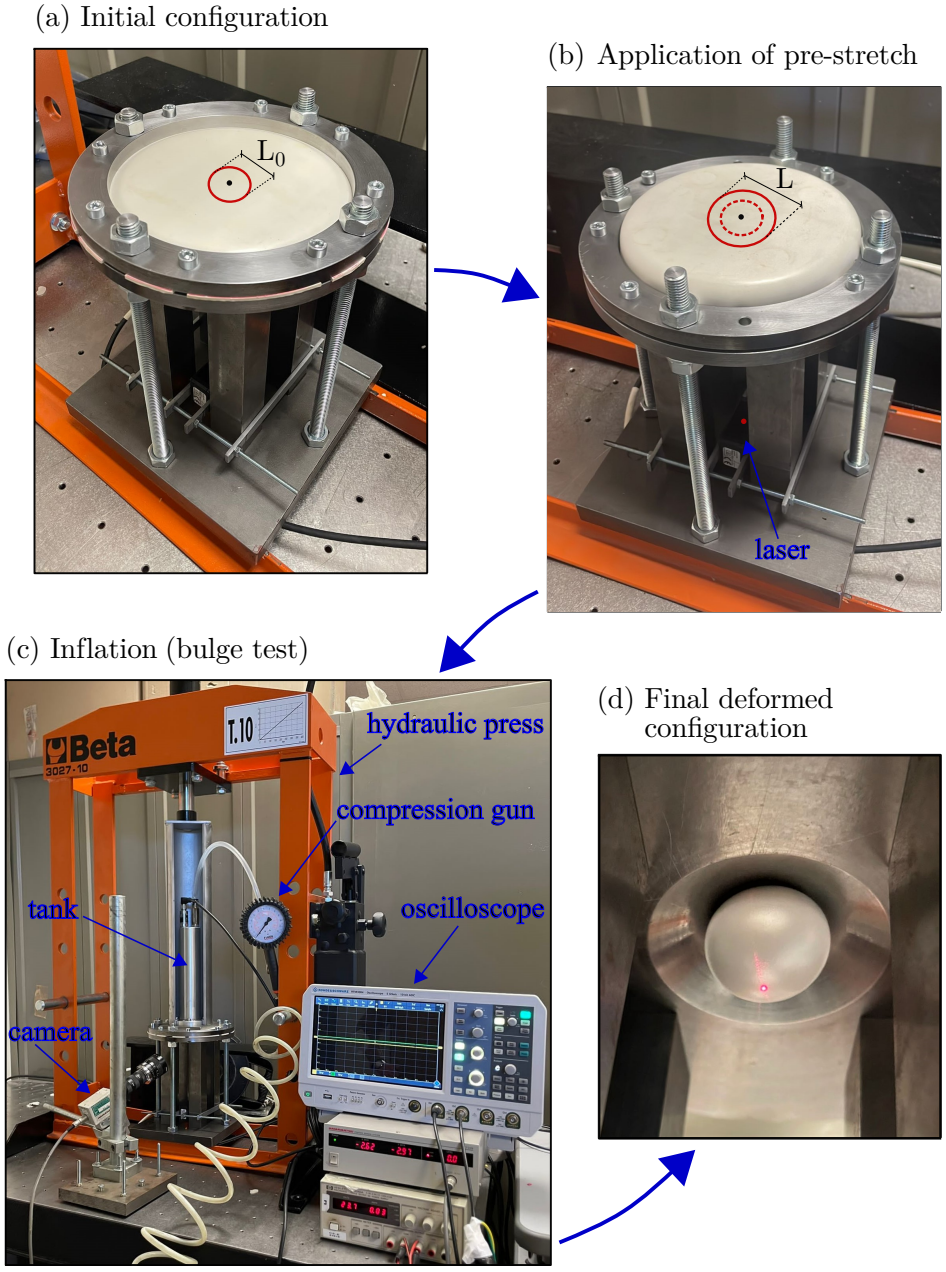

Figure 4.8: Set up for the bulge test on pre-stretched rubber membranes. (a) The membrane is placed on a steel plate with a central circular hole. Two steel rings fix the membrane. (b) The rings slide along four screwed rods and stretch the membrane. A laser sensor is placed at the bottom to measure the membrane deflection. (c) A perforated striking plate connected to a tank is positioned on the membrane. A low-pressure compressor injects air into the tank and generates pressure applied on the membrane. (d) Deformed configuration of the circular pre-stretched membrane after inflation.

Table 4.3: Values of pre-stretch and Mooney-Rivlin parameters calibrated by fitting experimental data from bulge tests.

	$\bar{\lambda}$	a (MPa)	b (MPa)	β
NBR	1.3	0.5	0.015	0.03
Silicone	1.1	0.55	0.03	0.055
NR	1.2	0.37	0.0296	0.08

corresponding voltage values following a resistive approach. The Rohde & Schwarz RTM3004 oscilloscope acquired the voltage signals and the data files are then processed using MATLAB, obtaining as outcome the pressure-deflection curve.

For further validation, the membrane deflection is measured by targeting the position of the membrane centre with an optical follower analogue camera (1 Optron 5000 Hz, produced by Hamamatsu). The camera follows the position of the red dot generated by the laser. The output of the camera are two independent signals related to vertical and horizontal components of displacement. This allows a cross-check of the deflection data from the laser sensor and to make sure that the horizontal component of displacement is negligible.

4.4.2 Calibration of model parameters

Quasi-static bulge tests are carried out on NBR, silicone and NR rubber sheets. For each kind of rubber three specimens are tested. Before inflation, the specimens have been subjected to a pre-stretch equal to 1.3, 1.1 and 1.2 respectively for NBR, silicone and NR. The choice of the pre-stretch is conditioned by the friction which develops during the sliding of the steel rings, preventing the application of larger values of pre-stretch.

After the tests, the experimental curves are fitted to calibrate the material parameters of the Mooney-Rivlin material model. As done in Section 3.5.2, it assumed that the tested materials are incompressible, as it happens in most cases for elastomers. Therefore, the only material parameters to be fitted are a and b, and the adjusted pressure for incompressible materials is used to this purpose.

The experimental responses and the analytical fitting curves for each rubber are shown in Fig. 4.9. The calibrated Mooney-Rivlin parameters a and b are reported in Table 4.3. The analytical formula results in excellent agreement with the experimental curves for NBR and silicone. Regarding NR rubber, the analytical curve fits well the experimental response until a stretch approximately equal to 2.5. From that point the experimental response starts to exhibit a hardening trend, similar to the one shown by the silicone tested in Section 3.5.2 (see Fig. 3.14) and typical of some class of polymers for large strains. This behaviour can not be described appropriately by the Mooney-Rivlin model, causing a discrepancy between the experimental and analytical curves.

Combining the results of Fig. 3.14 and Fig. 4.9 it can be concluded that the proposed analytical formula for the pressure can be used for the characterization of

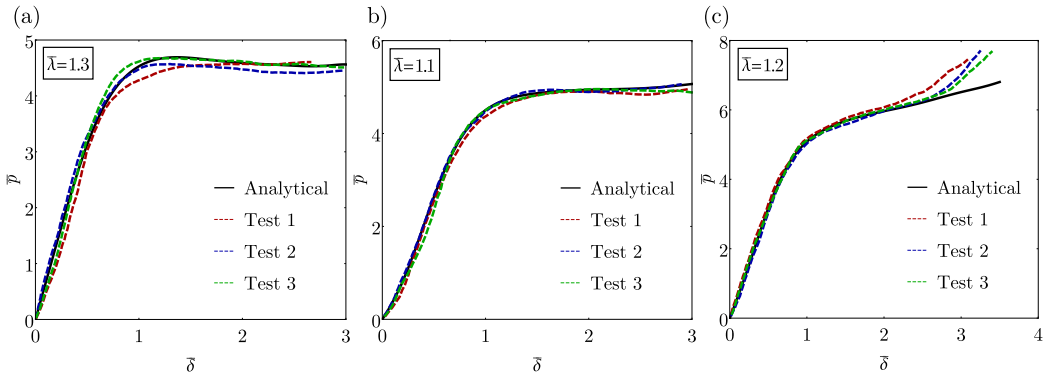

Figure 4.9: Normalized pressure-deflection curves from bulge tests and comparison with analytical predictions given by Eq. (4.13) for (a) NBR rubber, (b) silicone and (c) NR rubber. The material parameters used in the analytical formula are listed in Table 4.3.

material parameters on the basis of bulge tests. It is particular reliable for small to moderate strains, since in this range the Mooney-Rivlin model is capable of capturing accurately the response of elastomers. For large strains, more complex phenomena take place, like the hardening due to the limit extensibility of polymer chains. The Mooney-Rivlin results inadeguate to provide a satisfactory simulation of elastomers at large strains, and more refined constitutive law are required, such as those proposed by Ogden [58], Yeoh, [59], Gent [60] and Yeoh & Fleming [61]. A detailed discussion and analysis of such strain energy functions is developed in Chapter 5, in order to select a refined strain energy function for accurate predictions of the response of elastomers with particular attention to material compressibility.

5 A strain energy function for large deformations of compressible elastomers

The analysis on inflated circular membranes carried out in previous chapters showed the need of refined material models to comprehensively describe the response of elastomers at large deformations. Indeed, despite its mathematical convenience, the Mooney-Rivlin model is not capable of reproducing the hardening effect at large deformations. In addition, the Charlet-Geymonat function adopted to model compressibility lacked of a physical basis on the real response of elastomers to volume changes. The goal of the present chapter is to develop a strain energy function able to overcome these limitations and to provide an accurate description of the response of elastomers to both large shape and volumetric deformations. In the next chapter, the proposed SED will be applied to the study of benchmark problems of inflatable membranes.

Elastomers are typically modelled under the assumption of material incompressibility. This common approach is based on the observation that their bulk modulus is much larger than their shear modulus [70–72]. This assumption considerably simplifies the mathematical form of equilibrium problems, and therefore it has been adopted by many researchers [73–75]. However, most problems in the framework of finite elasticity remain impossible to be solved analytically, requiring the use of finite element codes. The implementation of incompressible constitutive models in finite element algorithms often causes serious convergence problems due to volumetric locking [76, 77]. In addition, some experimental tests have already indicated that some kind of rubbers can experience volume changes, resulting compressible [5, 6, 56, 78]. To overcome these issues, some compressible and slightly compressible models for elastomers have been proposed in the literature [79, 80].

Horgan and Saccomandi [81] developed a constitutive model for slightly compressible materials that reflects limiting chain extensibility. Peng et al. [82] proposed an extension of the Mooney-Rivlin hyperelastic model introducing a term that takes into account compressibility. Lengyel et al. [83] studied the interface crack between a compressible elastomer and a rigid substrate and found that the solution was sensitive to the bulk properties of the material. Li et al. [84] adopted a compressible constitutive law for rubber-like materials to describe the evolution of damage due to the Mullins effect and the cavity growth process. Landis et al. [85] analyzed the surface wrinkles and creases in constrained dielectric elastomers under electromechanical loading by assuming a compressible material model. Angeli et al. [86] proposed analytical solutions for carbon fiber-reinforced isolators with compressible elastomer subjected to compression and bending.

The deviatoric-volumetric decoupling of the SED [87] is the most convenient

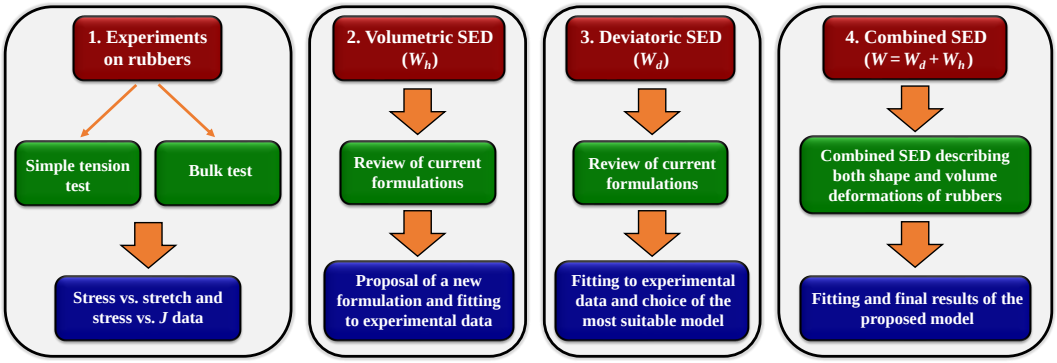

Figure 5.1: Outline of the steps for the calibration of the proposed SED.

approach to the study of the compressible materials. The advantage is the possibility of an indipendent characterization of the volumetric response of the material. Nevertheless, only a few authors analyzed the volumetric behavior [88], whereas many attentions have been devoted to model the deviatoric material response (see, e.g., [89–94]).

In the following, a new volumetric SED for elastomers is proposed, based on the volumetric response of four different elastomers to simple tension and bulk tests. The deviatoric part of the SED is selected from the literature in order to provide an accurate simulation of the experimental response. The combination of the two provides the overall proposed SED for large deformations of compressible elastomers. The steps leading to the derivation of the proposed SED for compressible elastomers are outlined in Fig. 5.1. A brief description of each step is provided in the following:

(1) Simple tension and bulk tests performed on four kinds of rubbers are presented. The stress vs. stretch curves and the σ_h vs. J curves are obtained.

(2) The currently available volumetric SED formulations are analyzed and their limitations are discussed. Consequently, a new volumetric SED function that overcomes such limitations is proposed. The model parameters are fitted on the experimental σ_h vs. J data.

(3) The most common strain energy functions for the deviatoric part of the SED are reviewed. Each model is fitted to the experimental data in simple tension and the most suitable formulation is selected.

(4) The combined SED formulation is obtained by assembling the deviatoric and the proposed volumetric parts. The model describes both shape and volume changes of compressible rubbers under large deformations.

5.1 Experimental investigation on the compressibility of elastomers

Among the numerous experimental tests carried out to derive the stress vs. stretch response of rubbers, only a few works dealt with the measure of volumetric deformations [95, 96]. In this section, simple tension tests and bulk tests on four kinds of rubber are carried out and presented. The rubbers considered are EPDM (ethylene propylene diene monomer), NBR (nitrile butadiene rubber), NR (natural rubber) and silicone. During the simple tension test, the lateral strain is monitored by a digital image correlation technique (DIC). Combining the results of both tests, the complete volumetric response of the materials is determined.

5.1.1 Simple tension test

Three dogbone specimens are prepared for each rubber considered. The specimens had an effective length of 60 mm, a height of 7 mm and a thickness of 1 mm. The tests were performed using the testing machine Instron 5567. The elongation was applied with a displacement rate of 500 mm/min.

Digital image correlation is employed to monitor the displacement field during each test. In particular, as shown in Fig. 5.2(a), a Nikon D3200 camera is used to record a video throughout the experiment. The camera is positioned in front of the specimen with an orthogonal view, which is ensured by properly installing a tripod. The camera records a video of the test from the initial load application to the specimen failure. From the video, 100 frames are extracted with regular time intervals. The captured images are then imported to MATLAB and processed with the open-source DIC package *Ncorr* [97].

A rectangular region of interest (ROI) is defined in the central part of the rubber specimen, where the strains are expected to be homogeneous. The dimension of the region of interest is 40 mm x 5.5 mm. The DIC analysis with *Ncorr* provides the displacement and strain fields in both longitudinal and lateral directions. Contour plots of the test on NBR are displayed in Fig 5.3. Both longitudinal and lateral strains ε_x and ε_y inside the ROI are homogeneous. Since *Ncorr* computes the Green-Lagrange strain components [98], the corresponding values of stretch components are computed as $\lambda_x = \sqrt{1+2\varepsilon_x}$ and $\lambda_y = \sqrt{1+2\varepsilon_y}$. As a double check, the images are post-processed with the MATLAB application *Ncorr_post*. Virtual extensometers are placed inside the ROI along x and y directions. The software computes the relative displacements, from which stretches are calculated. The accuracy of the strain fields is then checked.

The nominal stress s_x is computed as F/A, where F is the force applied by the testing machine and A is the cross-section area of the specimen in the initial configuration (7 mm x 1 mm). In this way, the stress vs. stretch curve is derived from each test. For each rubber, three tests are carried out on the three specimens prepared. Since there is not much variation in the results of the three tests, the average data of stretches and stresses are considered.

The experimental data are displayed in Figs. 5.4(a) and 5.4(b) in terms of s_x

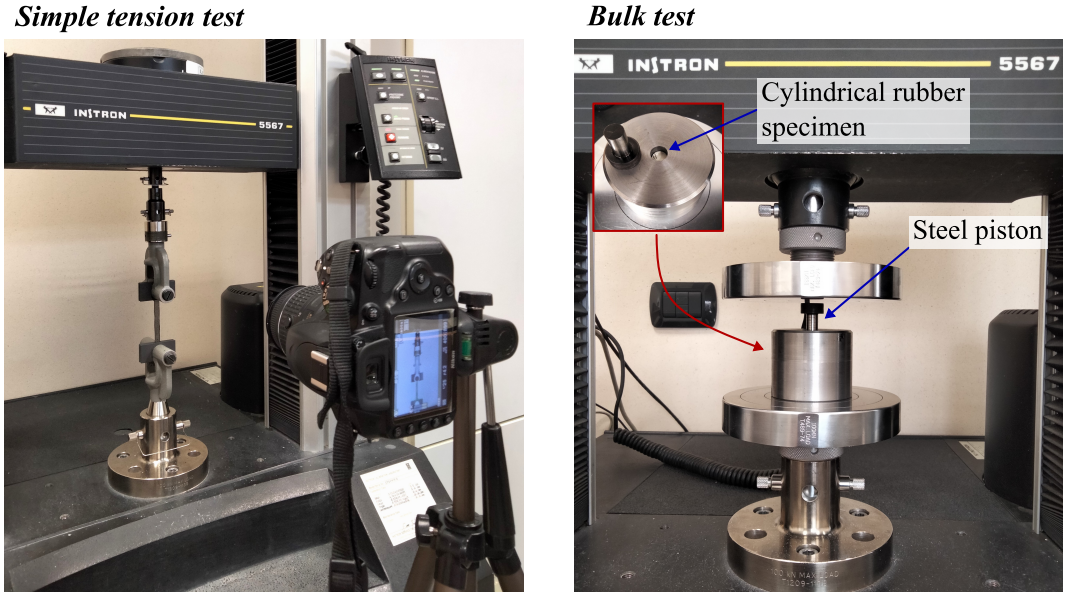

Figure 5.2: Experimental tests on elastomers to measure volumetric deformations. (a) Simple tension test performed on a dogbone specimen. The test is monitored with a camera and the displacement field is obtained through digital image correlation (DIC). (b) Bulk test performed on a cylindrical specimen. The specimen is inserted into a rigid annulus and a steel piston is used to apply the axial load.

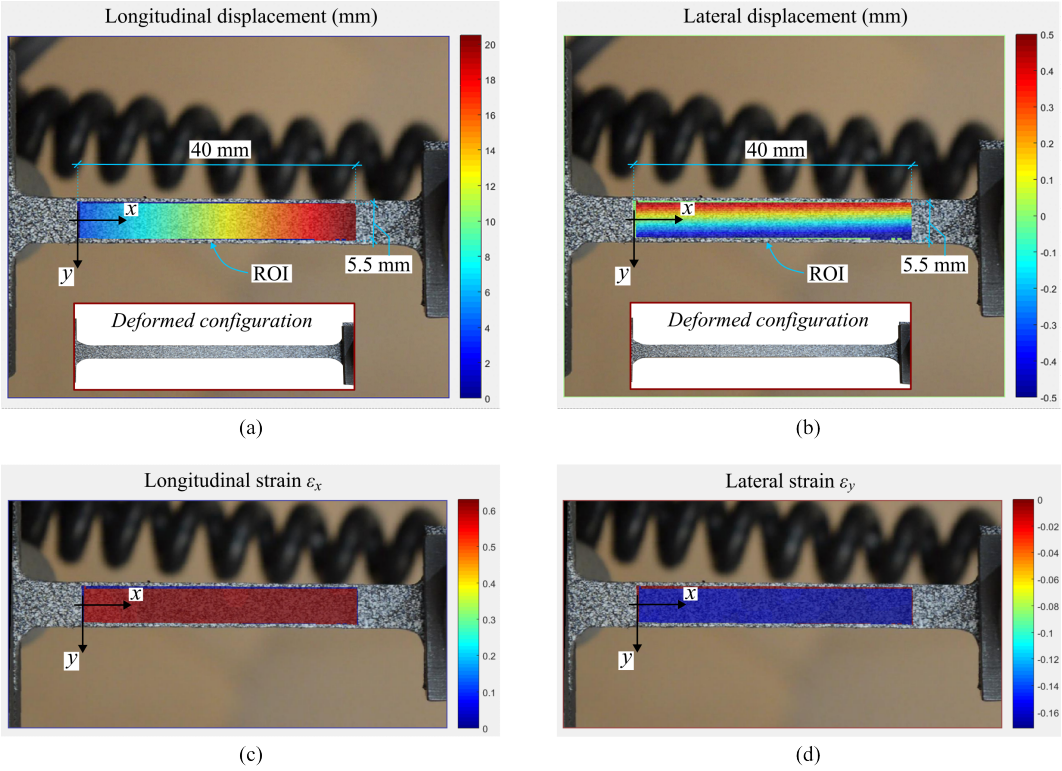

Figure 5.3: Contour plots in the selected region of interest (ROI) obtained from DIC analysis with MATLAB software *Ncorr*. Figures (a) and (b) show respectively longitudinal and lateral displacement fields, while figures (c) and (d) show longitudinal and lateral strain fields, respectively. The plots are referred to the simple tension test on NBR at the step corresponding to longitudinal stretch $\lambda_x = 1.5$.

vs. λ_x and λ_y vs. λ_x curves, respectively. Figure 5.4(b) shows a representation of the incompressible limit, expressed by $\lambda_y = 1/\sqrt{\lambda_x}$. The response of all four rubbers is very close to incompressibility for relatively small strains. EPDM and NBR start to deviate at values of longitudinal stretch around 1.35 and 1.15 respectively. On the other hand, NR and silicone are nearly incompressible throughout the deformation process and show sensible deviations only for very large deformations. The significant amount of specific fillers contained in both EPDM and NBR compounds, such as carbon black, can provide an explanation for these behaviors. Instead, the amount of filler in NR rubber and silicone considered in this work is very low. A higher compressibility associated with an increase in filler content is observed also in other works [99, 100].

Only a few experimental measurements of the lateral deflection in rubbers are reported in the literature. The results of such experiments agree with the ones derived from the presented experiments. Starkova and Aniskevich [5] performed uniaxial tension tests on silica-filled SBR rubber and measured the Poisson's ratio ν during the experiments. They found out that for small stretches the response is close to incompressibility ($\nu \approx 0.5$), while for large deformations ν becomes stretch-dependent

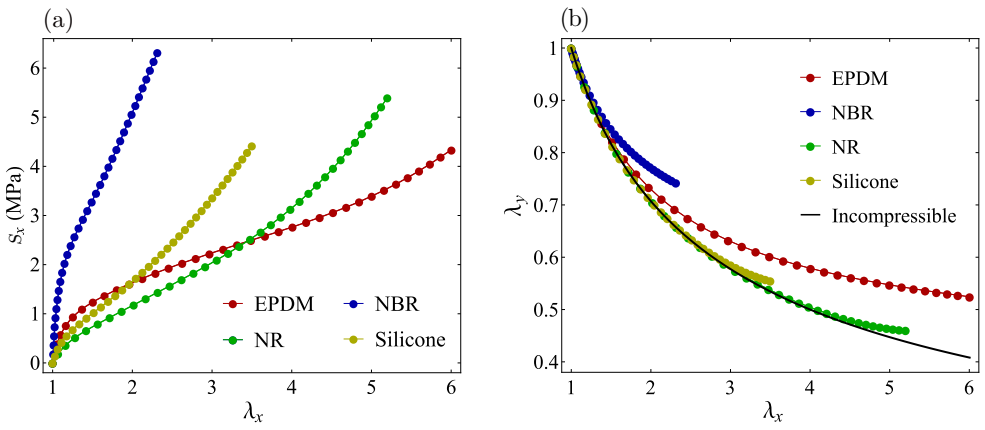

Figure 5.4: Results from simple tension tests on EPDM, NBR, NR and silicone. (a) Nominal stress s_x vs. longitudinal stretch λ_x and (b) lateral stretch λ_y vs. longitudinal stretch λ_x. The black curve shows the behavior of incompressible materials, expressed by $\lambda_y = 1/\sqrt{\lambda_x}$.

and the material is compressible. Kugler et al. [6] considered five elastomers and reported measurements of volume changes during simple tension tests, which showed once again that compressibility increases with the deformation.

5.1.2 Bulk test

The bulk (or volumetric compression) test involves the application of an axial compressive load on a cylindrical specimen inserted into a rigid annulus. The deformation of the cylinder is homogeneous and it is entirely attributed to volume change. In fact, the lateral deformation of the cylindrical specimen is constrained ($\lambda_y = \lambda_z = 1$) and we have that $\lambda_x = J$.

Three cylindrical specimens with a height of 12 mm and a diameter of 10.5 mm were prepared for each rubber. A cylindrical steel block with a circular hole was manufactured. The hole had a depth of 20 mm and a diameter of 10.55 mm. The rubber specimen was inserted into the hole so that its side walls were fixed. Note that the diameter of the hole in the steel block was slightly larger than that of the specimen so as to allow smooth insertion and removal.

As shown in Fig. 5.2(b), a steel piston with the same diameter as the cylindrical specimen was used to apply the axial load. The tests were performed by using the testing machine Instron 5567 equipped with a 30 kN load cell. A limit on the applied load was set to 26 kN, which corresponds to an axial stress on the specimen of around 300 MPa. The displacement was applied with a displacement rate of 2 mm/min. At the beginning of the test, the lateral walls of the specimen were still not perfectly constrained by the rigid annulus, due to a slightly smaller diameter. Thus, the data until an applied force of 4 N were removed. Such a force corresponds to an axial stress of approximately 0.05 MPa. This cut-off value was defined by computing the axial stress corresponding to a lateral strain of 0.48%, which is the condition where the specimen touches the internal walls of the rigid annulus. Since

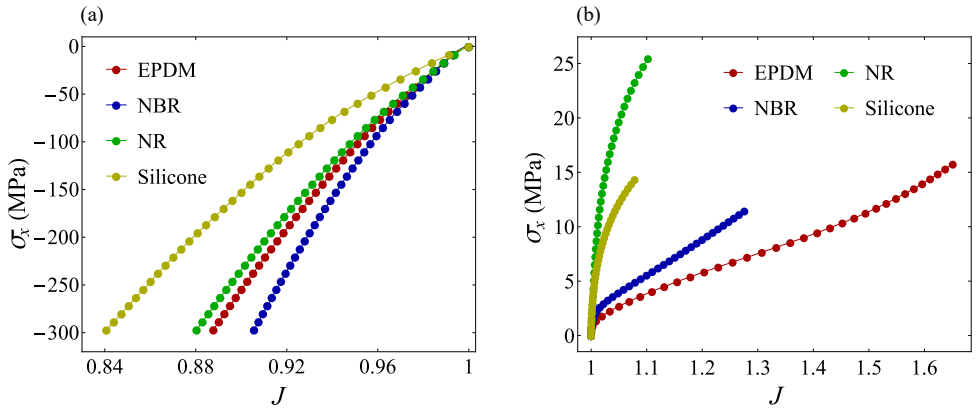

Figure 5.5: Cauchy stress σ_x as a function of volume change J from experimental tests on EPDM, NBR, NR and silicone. Figure (a) shows the response obtained from the bulk tests, where the specimens are subjected to shrinkage ($J \leq 1$), while figure (b) shows the response from simple tension tests, where the volume of the specimens is expanding ($J \geq 1$).

the strains are still small, this simple computation was done by assuming a linear elastic response with Poisson's ratio 0.5 and Young's modulus 5 MPa.

The force vs. displacement data were converted into stress vs. stretch data. In this test, the nominal stress s_x is equal to the true stress σ_x. Hence, for convenience in the following analysis, the results are given in Fig. 5.5(a) in terms of true stress as a function of J. The curves show that, at the maximum level of stress, all four rubbers undergo large volumetric changes (up to 10-15% of shrinkage).

The above results show the response of the rubbers in terms of σ_x vs. J curve when $J < 1$ (shrinkage). To have a comprehensive picture of the volumetric changes in the materials, the σ_x vs. J curve was extracted from the experimental data from the simple tension tests, which show the response when the volume is expanding ($J > 1$). The results are shown in Fig. 5.5(b).

As discussed in detail in A.2, it can be assumed that for rubber-like materials the axial stress measured during the bulk test is approximately equal to the hydrostatic stress ($\sigma_h \approx \sigma_x$). In light of this, the bulk modulus κ was derived from the slope of the experimental data from bulk tests in the small-strain domain. In shrinkage, the range of small strains was identified by observing until what magnitude of deformation the material response was still approximately linear. For the rubbers considered, the linear behavior is restricted to a shrinkage of 2‰. The estimated values of κ are reported in Tab. 5.1 and a detail of the experimental data from bulk tests in the small-strain region is shown in Fig. 5.6.

Table 5.1: Values of bulk modulus κ calibrated from the experimental data from bulk tests in the small-strain domain (up to a shrinkage of 2‰).

Rubber	κ (MPa)
EPDM	490
NBR	410
NR	710
Silicone	670

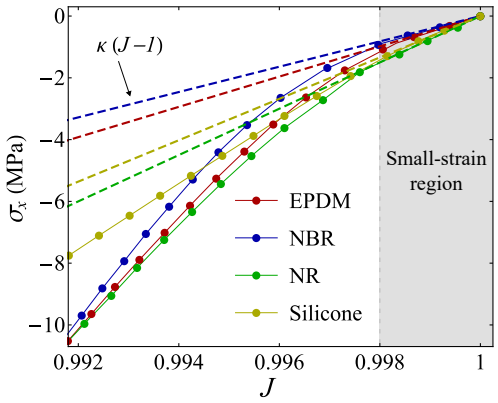

Figure 5.6: Detail of the experimental data from bulk tests. The values of bulk modulus reported in Tab. 5.1 were calibrated in the small-strain region, up to a shrinkage of 2‰, where the response of all the rubbers is approximately linear. The dashed lines represent the linear response given by $\kappa(J-1)$.

5.2 The split of the SED and current volumetric formulations

When dealing with compressible materials, the SED is written as a function of all three invariants I_1, I_2 and I_3 (or J). The general form of the SED reads

$$W = W(I_1, I_2, J), \tag{5.1}$$

or alternatively

$$W = W_c(I_1, I_2, J) + W_h(J), \tag{5.2}$$

where W_c and W_h are respectively the compressible and the hydrostatic terms of the strain energy. Despite of this distinction, both terms contribute to the response to a volume change, whether or not J appears explicitly in W_c [80]. The most convenient approach to develop phenomenological models for compressible materials, and to identify the response of the material to volume changes, consists in the split of the strain energy function into its deviatoric and volumetric parts. This can be achieved by introducing the so-called deviatoric strain invariants, defined as

$$\bar{I}_1 = J^{-2/3} I_1, \quad \bar{I}_2 = J^{-4/3} I_2. \tag{5.3}$$

This allows to write the SED as the sum of two uncoupled terms, responsible for the deviatoric (shape changing) and volumetric (volume changing) deformations. The SED assumes the form

$$W = W_d\left(\bar{I}_1, \bar{I}_2\right) + W_h\left(J\right), \tag{5.4}$$

where W_d is the deviatoric term of the strain energy. In this case, $W_h\left(J\right)$ is the only responsible for the material response to pure volumetric deformations and its characterization determines the response of the material to volume changes.

As classic results in Elasticity, the Cauchy stress tensor can be decomposed into a deviatoric and hydrostatic contribution

$$\mathbf{T} = \mathbf{T_d} + \sigma_h \mathbf{I}, \tag{5.5}$$

being $\mathbf{T_d}$ the deviatoric part of the Cauchy stress, σ_h the hydrostatic stress and $\mathbf{I}$ the identity tensor. The hydrostatic stress is defined as [88]

$$\sigma_h = \frac{1}{3}\mathrm{tr}(\mathbf{T}). \tag{5.6}$$

The deviatoric-volumetric split allows to compute the hydrostatic stress directly as

$$\sigma_h = \frac{\partial W_h}{\partial J}. \tag{5.7}$$

The above relations allow an independent characterization of the volumetric part W_h by measuring volume changes in experimental tests. In the case of simple tension test, $\sigma_2 = \sigma_3 = 0$ and $\mathrm{tr}(\mathbf{T}) = \sigma_1$, where σ_1 is the principal Cauchy stress in the longitudinal direction. Therefore, combining Eqs. (5.6) and (5.7), the relation between the stress and W_h reads becomes

$$\frac{1}{3}\sigma_1 = \sigma_h = \frac{\partial W_h}{\partial J}, \tag{5.8}$$

In the case of bulk tests, the expression of the principal stress in longitudinal direction can be expressed as

$$\sigma_1 \approx \sigma_h = \frac{\partial W_h}{\partial J}. \tag{5.9}$$

This approximation is based on the consideration that for elastomers the bulk modulus remains much larger than the shear modulus in the entire range of deformation. A detailed demonstration is carried out in Appendix C.

Following Eqs. (5.8) and (5.9) the σ_h vs. J curve is derived from the experimental data described in Section 5.1 for the four materials considered. In the following, the most significant formulations of volumetric SEDs are introduced. Their effectiveness in modeling the volume changes in elastomers is studied by fitting the experimental σ_h vs. J curves.

Table 5.2: Validity criteria and physical constraints of volumetric SED formulations, as reported in Moerman et al. [88].

Crit.	Description	Form
I	Zero SED in reference state	$\Psi_{vol}(J=1)=0$
II	Zero hydrostatic stress in reference state	$\sigma_h(J=1)=0$
III	Positive strain energy density	$\Psi_{vol}(J\neq 1)>0$
IV	Consistent with linear elasticity	$\frac{d^2\Psi_{vol}(J=1)}{dJ^2}=\kappa$
V	SED approaches ∞ if J approaches 0	$\lim_{J\to 0}\Psi_{vol}(J)=+\infty$
VI	Hydrostatic stress approaches $-\infty$ if J approaches 0	$\lim_{J\to 0}\sigma_h(J)=-\infty$
VII	SED approaches ∞ if J approaches ∞	$\lim_{J\to\infty}\Psi_{vol}(J)=+\infty$
VIII	Hydrostatic stress approaches ∞ if J approaches ∞	$\lim_{J\to\infty}\sigma_h(J)=+\infty$
IX	Tangent modulus >0 (polyconvexity)	$\frac{d^2\Psi_{vol}(J)}{dJ^2}\geq 0$
X	Control of strain stiffening for all J	

5.2.1 Review of current volumetric formulations

Doll and Schweizerhof [101], following previous developments in the literature (e.g. [102]), established nine criteria and physical constraints that should be respected to guarantee the phyisical plausibility of a volumetric strain energy function. These validity criteria impose conditions on the SED, on the hydrostatic stress, and on their behavior for limiting values of J. In their recent work, Moerman et al. [88] added a tenth requirement, imposing an indipendent control of the response in shrinkage and in expansion. The ten validity criteria are reported in Tab. 5.2.

Hencky [103] and Simo [104] proposed two functions which are implemented in many finite element codes and have found large success due to their mathematical simplicity. The two functions read respectively

$$W_h(J)=\frac{\kappa}{2}\ln(J)^2 \tag{5.10}$$

and

$$W_h(J)=\frac{\kappa}{2}(J-1)^2 \tag{5.11}$$

They provide good performance for nearly-incompressible materials ($J\approx 1$), but they lead to non-physical behaviours when dealing with large volumetric changes. Indeed, they do not respect all the validity criteria and physical constraints reported in Tab. 5.2. In particular, as shown in [101], Eq. (5.10) does not satisfy criteria VIII and IX, while Eq. (5.11) does not satisfy criteria V and VI.

Doll and Schweizerhof [101] proposed a three-parameters volumetric function

$$W_h(J)=\frac{\kappa}{\alpha+\beta}\left(\frac{1}{\alpha+1}J^{\alpha+1}+\frac{1}{\beta-1}J^{-(\beta-1)}\right)-\frac{\kappa}{(\alpha+1)(\beta-1)} \tag{5.12}$$

that allows control in both shrinkage and expansion through parameters α and β. To satisfy the validity criteria they proposed, the constraints on parameters α and β are: $\alpha > 0$ and $\beta > 1$. Parameter α increases the response in expansion while slightly limiting the response in shrinkage, whereas parameter β produces the opposite effect. Note that the control on the response in shrinkage and expansion is not independent, since α and β have an effect on both branches. Thus, criterion X is not satisfied.

Montella et al. [105] proposed a five-parameters formulation

$$W_h(J) = \frac{\kappa}{2\beta_1}\left(e^{\beta_1 \ln(J)^2} - 1\right) + \frac{\kappa_2}{m\beta_2}\left(e^{\beta_2 |\ln(J)|^m} - 1\right) \tag{5.13}$$

developed starting from the exponentiated Hencky strain energy, firstly presented by Neff et al. [106]. This function provides a flexible formulation to model the volumetric response at large deformations and it respects the 9 criteria established in [101] with the following constraints on the model parameters: $\beta_1 \geq 1/8$, $\beta_2 \geq 1/8$, and $m > 2$. Parameters β_1 and β_2 allow for the simultaneous variation of response for shrinkage and expansion, acting respectively on the first and the second term of Eq. (5.13). Parameter κ_2 regulates the slope for higher strains. Finally, parameter m is capable of enhancing the response for $J > e$ and $J < 1/e$, while suppressing it in the range $1/e < J < e$. However, this formulation does not offer independent control on the response for shrinkage and expansion, not satisfying criterion X.

Moerman et al. [88] added a tenth requirement to the 9 described by Doll and Schweizerhof, which states that the volumetric part of a hyperelastic model should be capable of describing strain stiffening for all values of J. This means that the control of strain stiffening should be independent for shrinkage and expansion. In [88], the authors proposed three novel formulations for the volumetric strain energy function. Formulation No. 3, which is the most refined one, is given by the following function

$$W_h(J) = \kappa\left[-(1-q)a^2 \ln\left(\cos\left(\frac{J-1}{a}\right)\right) + qb^2 \ln\left(\cosh\left(\frac{J-1}{b}\right)\right)\right] \tag{5.14}$$

and involves three parameters a, b and q that assume different values for expansion and shrinkage. In particular, the parameters are defined as

$$a = \frac{2}{\pi}\begin{cases} J_1 - 1, & J \geq 1 \\ J_2 - 1, & J < 1 \end{cases} \qquad b = \frac{1}{\kappa}\begin{cases} s_1, & J \geq 1 \\ s_2, & J < 1 \end{cases} \qquad q = \begin{cases} q_1, & J \geq 1 \\ q_2, & J < 1 \end{cases} \tag{5.15}$$

This ensures that the formulation offers a completely independent control of the two branches. Including κ, the parameter values that must be calibrated are 7, and parameter q has the constraint $0 \leq q \leq 1$. More details about all the above formulations can be found in [88]. In this work, the authors tested the above formulations on experimental data of polymeric foams.

In the following, the current volumetric SED formulations are fitted to the σ_h vs. J curves derived from the experimental tests presented in Section 3.1 for EPDM, NBR, NR and silicone. The formulations proposed by Doll and Schweizerhof [101], Montella et al. [105] and Moerman et al. [88] are considered. The simple formulations proposed by Hencky [103] and Simo [104] are not taken into account, since they do

Table 5.3: Current volumetric SED formulations from the literature.

Formulation	$W_h(J)$
Hencky [103]	$\frac{\kappa}{2}\ln(J)^2$
Simo [104]	$\frac{\kappa}{2}(J-1)^2$
Doll and Schweizerhof [101]	$\frac{\kappa}{\alpha+\beta}\left(\frac{1}{\alpha+1}J^{\alpha+1}+\frac{1}{\beta-1}J^{-(\beta-1)}\right)-\frac{\kappa}{(\alpha+1)(\beta-1)}$
Montella et al. [105]	$\frac{\kappa}{2\beta_1}\left(e^{\beta_1\ln(J)^2}-1\right)+\frac{\kappa_2}{m\beta_2}\left(e^{\beta_2\lvert\ln(J)\rvert^m}-1\right)$
Moerman et al. [88], No. 3	$\kappa\left[-(1-q)a^2\ln\left(\cos\left(\frac{J-1}{a}\right)\right)+qb^2\ln\left(\cosh\left(\frac{J-1}{b}\right)\right)\right]$

not fulfill the previously mentioned criteria of physical plausibility. Besides, due to their simplicity, it is clear that they are not capable of performances as accurate as the other functions which involve more parameters.

The formulation presented above are gathered in Tab. 5.3. It goes without saying that further volumetric SED functions have been proposed in the literature. For instance, the formulations proposed by Bischoff et al. [80], Ogden [58], Hill [107], and Horgan and Murphy [108]. However, such formulations do not fulfill all the criteria of physical plausibility and provide accurate behaviors only for small or moderate volume changes. Hence, they are not capable of accurately reproducing the response of the elastomers tested in Section 5.1 during both volume shrinkage and expansion.

5.2.2 Fitting to experimental data

The hydrostatic stress is computed as $\sigma_h = \partial W_h/\partial J$ for each of the volumetric SED formulations described above. The analytical expression is fitted to the experimental σ_h vs. J curve derived from simple tension and bulk tests by using the *FindFit* function in software *Wolfram Mathematica*.

For each rubber, the bulk modulus is fixed to its corresponding value given in Tab. 5.1. To perform an in-depth study of the advantages and limitations of each material model for both shrinkage and expansion, the fitting is done by considering separately the experimental data for $J < 1$ and $J \geq 1$. Hence, two sets of calibrated parameters are obtained for each formulation (note that the formulation by Moerman et al. already involves two values for each parameter). The calibrated parameters are reported in Tab. B.1 and the σ_h vs. J curves for each type of rubber are displayed in Fig. 5.7.

From Figs. 5.7(a), 5.7(c), 5.7(e) and 5.7(g), it is evident how none of the current formulations is capable of simulating accurately the volumetric curve of the rubber specimens in shrinkage. Indeed, most of the formulations were defined to capture the volumetric response of foams and hydrogels, which differ substantially from the response of elastomers. On one hand, as shown in [109, 110], the elastic volume

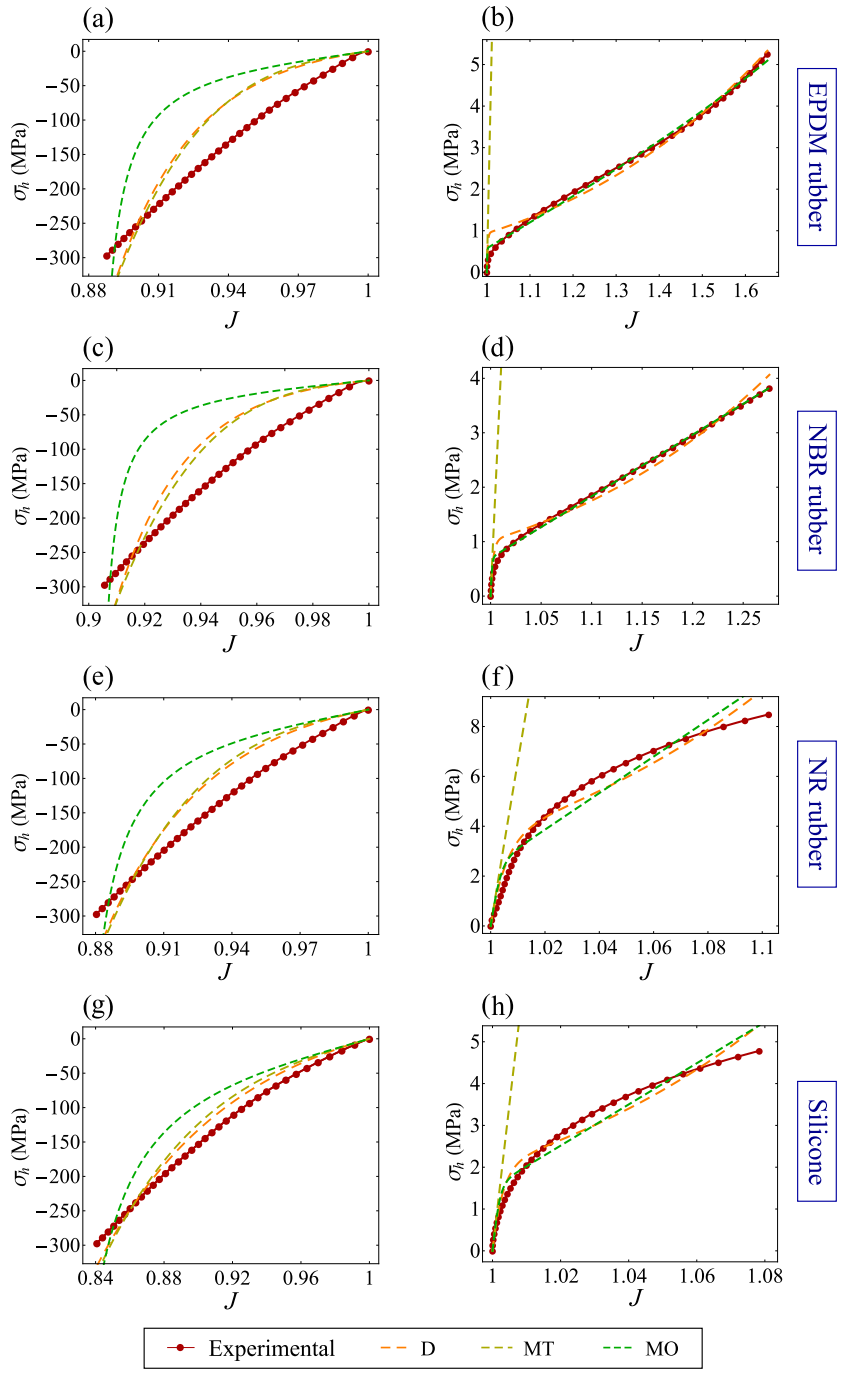

Figure 5.7: Fitting of current volumetric SED formulations to the experimental data from bulk tests (Figs. (a), (c), (e) and (g)) and simple tension tests (Figs. (b), (d), (f) and (h)) for (a) and (b) EPDM, (c) and (d) NBR, (e) and (f) NR, and (g) and (h) silicone. The following acronyms are used: D = Doll et al. [101]; MT = Montella et al. [105]; MO = Moerman et al. [88].

reductions in foams and hydrogels can reach easily values around 60-80% and strain stiffening typically takes place in a smooth way. On the other hand, in case of elastomers, a pronounced strain stiffening occurrs for small reductions of J. Then, the rate of stiffening decreases and stabilizes.

Figs. 5.7(b) and 5.7(d) show the behavior of EPDM and NBR when the volume is expanding. Except for the formulation by Montella et al., the current formulations give quite accurate descriptions of the volumetric response. Some discrepancies are found only in the range of $J \approx 1$. However, as shown in Figs. 5.7(f) and 5.7(h), for NR and silicone the predictions made by each one of the current SED functions are inaccurate. The reason consists in the fact that rubbers are nearly incompressible when $J \approx 1$, whereas they show a remarkable reduction in stiffness (softening) that takes place for relatively low values of J. This abrupt change in stiffness between the range of nearly-incompressible materials ($J \approx 1$) and the range of large volume changes makes the response of elastomers critical. For instance, the SED proposed by Moerman et al. is perfectly capable of reproducing both strain softening and stiffening in foams, which occurs smoothly and generally for much larger volume changes. However, the response of elastomers requires functions that capture these behaviors for smaller deformations and thus more rapidly.

In light of the above considerations, there is still a lack of a formulation capable of simulating accurately the entire response of elastomers to volume changes. The main limitations of the formulations currently available in the literature are the following:

- Most of them were developed for foams and hydrogels, therefore they exhibit limitations in reproducing the volumetric response of elastomers. In particular, they result uncapable of simulating the pronounced strain stiffening and softening shown by elastomers even for relatively small volume variations ($J \approx 1$).
- The formulations do not allow independent control of strain stiffening in shrinkage and expansion, except from the one proposed by Moerman et al. [88].
- The formulation proposed by Moerman et al. [88] involves one single set of parameters which assume two different values for $J < 1$ and $J \geq 1$, the form of the energy function being the same. For rubbers, and perhaps other materials, it is convenient to have two different response functions defining the diverse behaviors in shrinkage and expansion.

In the next section, a volumetric SED function is proposed with the aim to overcome the limitations described above.

5.3 The proposed volumetric SED

The proposed volumetric SED is expressed by

$$W_h(J) = \kappa \left[H(1-J)\,\Psi_c + H(J-1)\,\Psi_t \right], \tag{5.16}$$

where H is the Heaviside step function, defined as

$$H(x) = \begin{cases} 0, & x < 0 \\ 1/2, & x = 0 \\ 1, & x > 0 \end{cases} \tag{5.17}$$

and Ψ_c and Ψ_t, are two function which give indipendent control of shrinkage and expansion respectively. They are expressed by

$$\begin{aligned} \Psi_c(J) = \frac{1}{\alpha_1+\alpha_2-\alpha_3}\Bigg[\Bigg(J + \frac{J^{\alpha_1+1}}{\alpha_1+1} + \frac{J^{-(\alpha_2-1)}}{\alpha_2-1} - \frac{J^{\alpha_3+1}}{\alpha_3+1}\Bigg) \\ - \Bigg(1 + \frac{1}{\alpha_1+1} + \frac{1}{\alpha_2-1} - \frac{1}{\alpha_3+1}\Bigg)\Bigg], \end{aligned} \tag{5.18}$$

$$\Psi_t(J) = (1-q)\left[\frac{\beta_2 e^{\beta_1(J-1)} + \beta_1 e^{-\beta_2(J-1)}}{\beta_1\beta_2(\beta_1+\beta_2)} - \frac{1}{\beta_1\beta_2}\right] + q\beta_3^2 \ln\left(\cosh\left(\frac{J-1}{\beta_3}\right)\right). \tag{5.19}$$

The Heaviside step function allows an independent control of the response shrinkage and expansion. When $J<1$, $H(J-1)$ vanishes and $H(1-J)$ equals 1, therefore the energy reduces to $\kappa\Psi_c$. On the contrary, when $J>1$, $H(1-J)$ vanishes and $H(J-1)=1$. Hence, the energy reduces to $\kappa\Psi_t$.

The hydrostatic stress reads[1]

$$\sigma_h(J) = \frac{dW_h(J)}{dJ} = \kappa\left[H(1-J)\,\psi_c + H(J-1)\,\psi_t\right] \tag{5.20}$$

with

$$\psi_c(J) = \frac{d\Psi_c(J)}{dJ} = \frac{1 + J^{\alpha_1} - J^{-\alpha_2} - J^{\alpha_3}}{\alpha_1+\alpha_2-\alpha_3}, \tag{5.21}$$

$$\psi_t(J) = \frac{d\Psi_t(J)}{dJ} = (1-q)\frac{e^{\beta_1(J-1)} - e^{-\beta_2(J-1)}}{\beta_1+\beta_2} + q\beta_3 \tanh\left(\frac{J-1}{\beta_3}\right). \tag{5.22}$$

The presence of the Heaviside step function in Eq. (5.20) guarantees again a separate control on shrinkage and expansion for the hydrostatic stress, regulated by ψ_c and ψ_t respectively. Due to its discontinuity in $J=1$, in practical implementations the Heaviside step function can be replaced by a smooth approximation [111]. To this propose, the following smooth approximation is proposed

$$\begin{aligned} H(1-J) &\approx \frac{1-\tanh\left(10^3(J-1)\right)}{2} = \rho_c, \\ H(J-1) &\approx \frac{1+\tanh\left(10^3(J-1)\right)}{2} = \rho_t. \end{aligned} \tag{5.23}$$

[1] From the derivative of the product, the two terms $\delta(1-J)\Psi_c$ and $\delta(J-1)\Psi_t$ arise, where δ is the Dirac delta function. The above terms vanish because $\Psi_c\big|_{J=1} = \Psi_t\big|_{J=1} = 0$ and therefore the distributional products are identically zero.

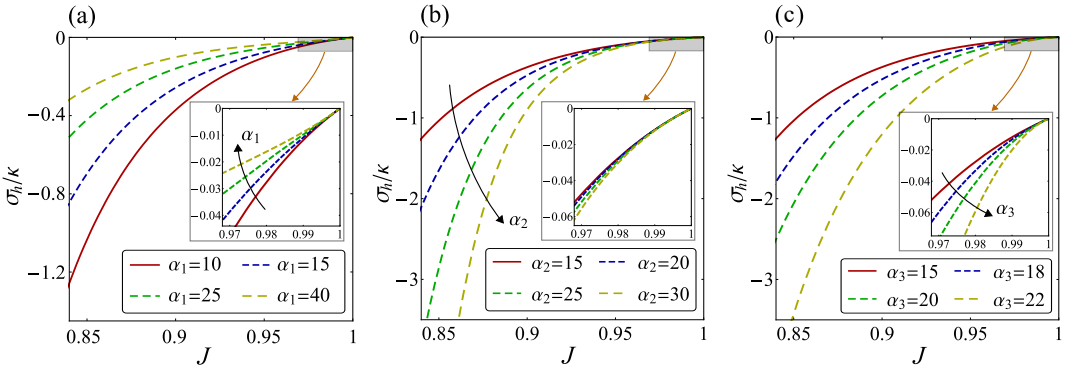

Figure 5.8: Effect of parameters α_1, α_2 and α_3 of the proposed volumetric SED, which control the behavior for volume shrinkage. Parameters α_1 (a) and α_3 (c) are responsible respectively for strain softening and stiffening in the region of small to moderate shrinkage. Parameter α_2 (b) controls hardening during large volume shrinkage, while it has very little effect for small and moderate deformations. The curves are drawn starting from $\alpha_1 = 10$, $\alpha_2 = 15$ and $\alpha_3 = 15$, then the parameters are varied one by one.

The factor 10^3 ensures an adequate steepness of functions ρ_c and ρ_t when $J \to 1$. The volumetric strain energy and the hydrostatic stress become

$$W_h(J) = \kappa \int (\rho_c \psi_c + \rho_t \psi_t)\, dJ, \tag{5.24}$$

$$\sigma_h(J) = \kappa (\rho_c \psi_c + \rho_t \psi_t). \tag{5.25}$$

A detailed discussion on smooth approximations of step functions is found in [112–114].

Overall, the model involves seven parameters in addition to the bulk modulus. Parameters α_1, α_2 and α_3 control the response in shrinkage, while β_1, β_2, β_3 and q control the response in expansion. The proposed SED fulfills the 10 requirements reported in [88] provided the parameters satisfy the following constraints:

$$\begin{cases} \beta_1 > 0,\ \beta_2 > 0,\ \beta_3 > 0,\ 0 \le q \le 1 \\ \alpha_1 > 0,\ \alpha_2 > 1,\ \alpha_3 > 0,\ \alpha_1 + \alpha_2 - \alpha_3 > 0 \end{cases} \tag{5.26}$$

A thorough demonstration of the above inequalities is carried out in Appendix B. The term ψ_c in the hydrostatic stress, given in Eq. (5.21), is the results of adding parameter α_3 to the formulation proposed by Doll and Schweizerhof [101]. The effect of parameters α_1, α_2 and α_3 is displayed in Fig. 5.8. Parameters α_1 and α_3 produce, respectively, strain softening and stiffening in the range of small to moderate volume shrinkage. Parameter α_2 controls hardening for large volume changes. The combination of parameters α_1 and α_3 allows to model the rapid strain stiffening that occurs in rubbers for relatively small shrinkage values.

The term ψ_t in the hydrostatic stress, given in Eq. (5.22), is inspired by the formulation proposed by Moerman et al. [88]. In formulation No. 3, the authors

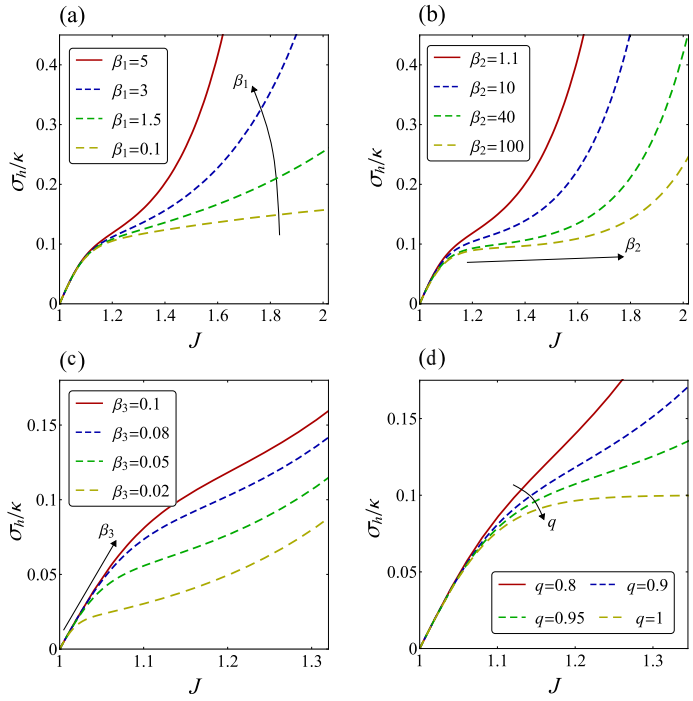

Figure 5.9: Effect of parameters β_1, β_2, β_3 and q of the proposed volumetric SED, which control the behavior for volume expansion. Parameter β_1 (a) regulates the amount of hardening at large volume expansions, while β_2 (b) controls the activation of the hardening in the range of moderate deformations. Parameter β_3 (c) controls the extent of the linear response and q (d) governs the transition from linear to nonlinear responses. The curves are drawn starting from $\beta_1 = 5$, $\beta_2 = 1.1$, $\beta_3 = 0.1$ and $q = 0.9$, then the parameters are varied one by one.

used functions *tan* and *tanh* to create vertical and horizontal sigmoid functions that simulate hardening and softening, respectively. In the proposed SED, the sum of two exponential functions with exponents β_1 and β_2 replace the *tan* function, which is not suitable for the nonlinear behavior of elastomers. The effect of parameters β_1, β_2, β_3 and q is displayed in Fig. 5.9. Parameter β_1 produces strain stiffening at large volume expansions. The range of J values at which strain stiffening activates is regulated by parameter β_2. Parameter β_3 controls the amplitude of the linear response in small deformations. Finally, q is a weight parameter that regulates the transition from linear to nonlinear response.

The proposed volumetric SED involves just one more parameter than the function proposed by Moerman et al. [88], but it exhibits the following main advantages:

- The proposed SED is a continuous function of J that is developed specifically for elastomers by observing their experimental behavior under large volume deformations.
- The Heaviside step function (or its smooth approximation) allows a total independent control of shrinkage and expansion.

- The formulation allows defining not only different parameters for shrinkage and expansion, but also different response functions. Since elastomers show different behaviours for $J < 1$ and $J \geq 1$, the two functions ψ_c and ψ_t were employed.
- When dealing with volumetric deformations of other hyperelastic materials, like foams and gels, the response functions ψ_c and ψ_t can be replaced by other expressions if necessary.

The expression of the hydrostatic stress σ_h as a function of J, reported in Eq. (5.20), is fitted to the experimental data to calibrate the best parameters of the proposed SED, both in volume shrinkage and expansion. The fitting is performed by using the *FindFit* function in software *Wolfram Mathematica*. For each rubber, the value of bulk modulus is fixed to the values given in Tab. 5.1. The calibrated parameters are listed in Tab. B.2 and the σ_h vs. J curves for each type of rubber are displayed in Fig. 5.10.

For every rubber, the proposed formulation provides excellent accuracy in both volume shrinkage and expansion. In the case of shrinkage, elastomers show a rapid strain stiffening that occurs for small volume changes. This effect is captured thanks to the introduction of the new parameter α_3 in function ψ_c. In the case of volume expansion, elastomers are nearly incompressible when $J \approx 1$ and then an abrupt softening takes place, which is in some cases followed by hardening for large values of J. The exponential terms introduced in function ψ_t, controlled by parameters β_1 and β_2, allow to reproduce such a behavior. In conclusion, the results in Fig. 5.7 demonstrate that the proposed model is capable of describing the volumetric response of rubbers for both small and large deformations, overcoming the limitations of the current models available in the literature.

5.4 The deviatoric part of the SED

In the previous section, an original formulation of a volumetric strain energy function for elastomers was proposed. Following the split of the strain energy function into its volumetric and deviatoric parts, a proper strain energy function must be selected as deviatoric part and coupled with the proposed volumetric SED. Regarding the deviatoric part of the strain energy function, extensive studies have been carried out in the literature. In this section, some of the most significant incompressible SEDs are investigated with the aim of selecting the most suitable deviatoric part for the prediction of the response of elastomers under large deformations. To this purpose, firstly the most common incompressible strain energy formulations from the literature are introduced, successively each formulation is fitted to the experimental results in simple tension.

It is important to specify that in the developments of this section the assumption of material incompressibility is adopted. Indeed, the purpose of this section is to investigate which material model provides the best prediction of the shape-changing large deformations occurring in elastomers, neglecting the variations in volume. In

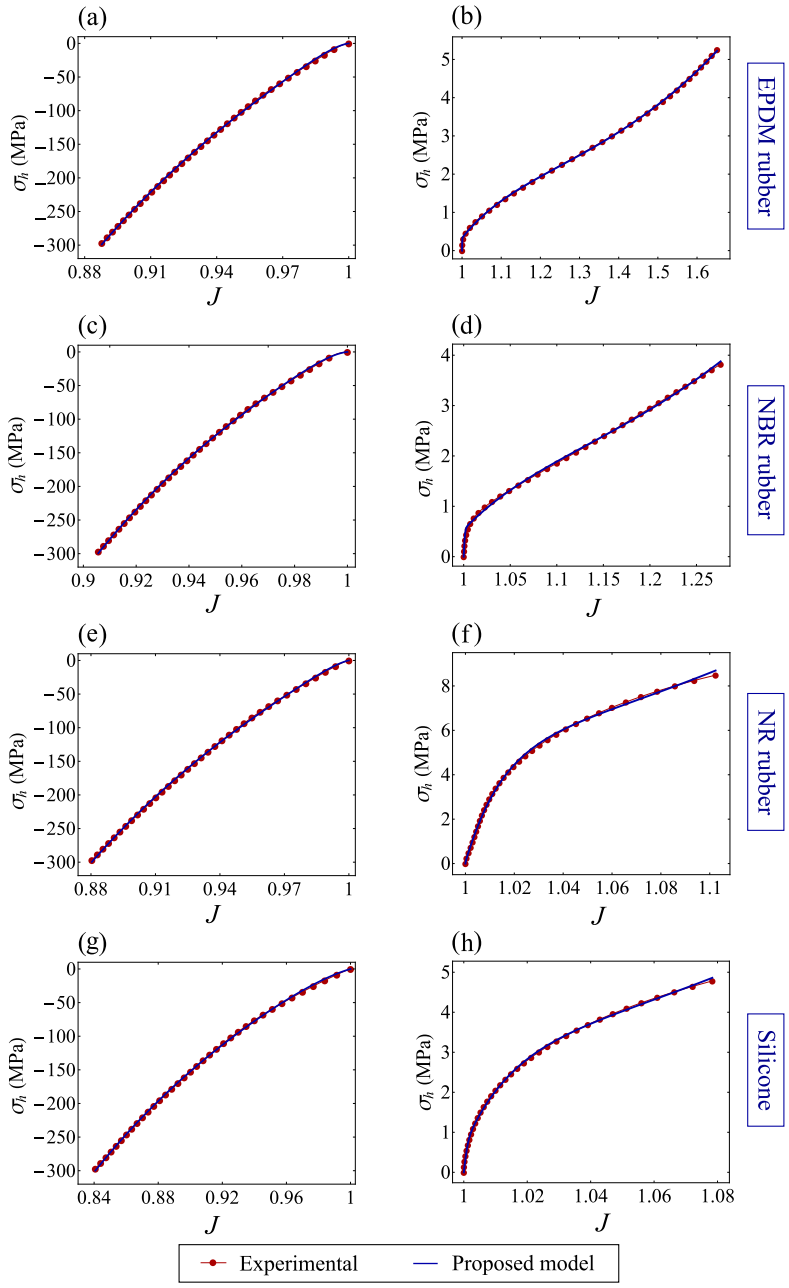

Figure 5.10: Fitting of the proposed volumetric SED formulation to the experimental data from bulk tests (Figs. (a), (c), (e) and (g)) and simple tension tests (Figs. (b), (d), (f) and (h)) for (a) and (b) EPDM, (c) and (d) NBR, (e) and (f) NR, and (g) and (h) silicone.

Table 5.4: Common deviatoric SED formulations from the literature.

Formulation	W_d
Neo-Hookean [116]	$C_{10}\left(I_1-3\right)$
Mooney-Rivlin [117]	$C_{10}\left(I_1-3\right)+C_{01}\left(I_2-3\right)$
Yeoh [59]	$C_{10}\left(I_1-3\right)+C_{20}\left(I_1-3\right)^2+C_{30}\left(I_1-3\right)^3$
Gent [60]	$-\frac{\mu}{2}J_m\ln\left(1-\frac{I_1-3}{J_m}\right)$
Gent-Gent [118]	$-C_1J_m\ln\left(1-\frac{I_1-3}{J_m}\right)+C_2\ln\left(\frac{I_2}{3}\right)$
Yeoh-Fleming [61]	$\frac{A}{B}\left(I_m-3\right)\left(1-e^{-B(I_1-3)/(I_m-3)}\right)-C_{10}\left(I_m-3\right)\ln\left(1-\frac{I_1-3}{I_m-3}\right)$
Carroll [119]	$AI_1+BI_1^4+CI_2^{1/2}$
Ogden [58]	$\sum_{i=1}^{M}\frac{\mu_i}{\alpha_i}\left(\lambda_1^{\alpha_i}+\lambda_2^{\alpha_i}+\lambda_3^{\alpha_i}-3\right)$

Section 5.5 the selected deviatoric SED will be coupled with the proposed volumetric SED in the framework of the split of the strain energy function. The coupled formulation provides a complete description of the response of elastomers to volume and shape-changing deformations.

5.4.1 Review of current incompressible strain energy functions

The generalized Rivlin model [115] is the foundation of many of the hyperelastic material laws. It is expressed by

$$W_d\left(I_1,I_2\right)=\sum_{i=0}^{n}\sum_{j=0}^{m}C_{ij}\left(I_1-3\right)^i\left(I_2-3\right)^j. \tag{5.27}$$

Truncating Eq. (5.27) to the first terms, the Neo-Hookean [116] and the Mooney-Rivlin [117] models are obtained. The Neo-Hookean model is defined as a linear function of the first invariant I_1 and it is based on considerations of the statistical molecular theory. The Mooney-Rivlin model considers deviations from the predictions of the molecular theory by adding a second term linearly dependent on I_2. The neo-Hookean and the Mooney-Rivlin models have been widely employed for their simplicity. However, it is well-known that they do not provide accurate descriptions of the response of rubbers at large strains. In particular, these models are not able to simulate the hardening at large deformations, which is a typical phenomenon occurring in several rubber-like materials. This limitation already appeared in Section 3.5.2 and Section 4.4.2, where the proposed analytical formula for the inflation of circular membranes was fitted to experimental bulge tests.

The formulation proposed by Yeoh [59] is another benchmark model in hyperelasticity. By analyzing the response of carbon-black-filled rubbers in simple tension, Yeoh [59] proposed a three-parameter model defined by a combination of the first three powers of invariant I_1. This model allows for a variable shear modulus along the deformation and it is capable of describing the increase of stiffness at large deformations.

One of the most successful phenomenological models to reproduce severe strain stiffening is the one proposed by Gent [60]. The Gent model corrects the neo-Hookean model in the range of large deformations by introducing a maximum achievable length of the molecular chains. Parameter J_m denotes the chain extensibility limit. This model has the advantage of mathematical simplicity since it involves just two constitutive parameters. However, several authors pointed out that it suffers some limitations in the range of small to moderate strains [74].

In view of this, other authors proposed extensions of the Gent model by introducing more constitutive parameters. The Gent-Gent model [118] is the most famous and it introduces a logarithmic dependence on the second strain invariant. Another modification was proposed by Yeoh and Fleming [61]. The authors combined concepts proposed by Yeoh and Gent in order to derive a comprehensive SED that is accurate for both small and large strains. The model proposed in [61] depends only on the first strain invariant but it involves four parameters. A more recent model composed of three parameters was proposed by Carroll [119]. The model was derived by considering firstly the neo-Hookean function and then adding terms to model the residual stress in experimental data from simple and equibiaxial extensions.

Lastly, the well-known hyperelastic model proposed by Ogden [58] must be mentioned. Contrary to previous formulations, which were expressed as functions of the principal invariants, the Ogden model is expressed as a function of the principal stretches. It consists of a combination of terms depending on the principal stretches raised to real powers. For consistency with the linearized theory, the constants must satisfy the following requirement: $\sum_{i=1}^{M} \mu_i \alpha_i = 2\mu$, where M is a positive integer and μ is the shear modulus.

The analytical expressions of these formulations are summarized in Tab. 5.4.

5.4.2 Fitting of incompressible models to experimental data

The Gent model, the Gent-Gent model, the Yeoh model, the Carroll model, the Yeoh-Fleming model, and the Ogden model with $M = 2$ are considered for the fitting to the experimental data. The neo-Hookean and Mooney-Rivlin models are neglected since they are not adequate to describe the response for large stretches. The incompressible SED formulations are fitted to the experimental stress vs. strain curves derived from the simple tension tests, given in Fig. 5.4(a). The analytical stress-strain relation for incompressible materials in simple tension is reported in Appendix A.1. The fitting procedure is carried out by means of the *FindFit* function in *Wolfram Mathematica*.

The fitting parameters for each formulation are reported in Tab. B.3. Figure 5.11 shows the results of the fitting for the four rubbers analyzed in this work. All the

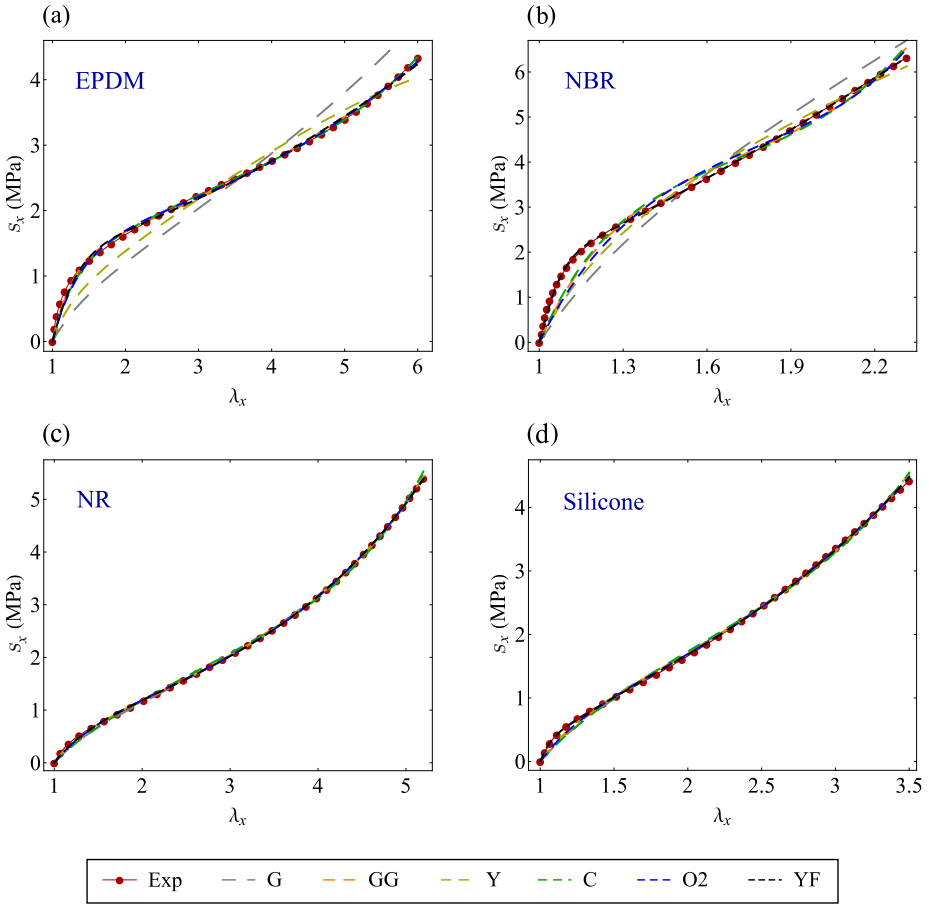

Figure 5.11: Nominal stress vs. stretch curves obtained by fitting the current incompressible deviatoric SED formulations to the experimental data from simple tension tests on (a) EPDM, (b) NBR, (c) NR and (d) silicone. The following acronyms are used: Exp = experimental; G = Gent [60]; GG = Gent-Gent [118]; Y = Yeoh [59]; C = Carroll [119]; O2 = Ogden [58] with $M = 2$; YF = Yeoh-Fleming [61].

formulations exhibit a good accuracy in reproducing the response of NR rubber and silicone, given in Fig. 5.11(c) and Fig. 5.11(d) respectively. From Fig. 5.11(a) it is evident that the Gent and the Yeoh models are not capable of simulating accurately the response of EPDM rubber. However, Fig. 5.11(b) shows that only the Yeoh-Fleming model is capable of reproducing the behavior of NBR. All the other models are inaccurate, especially in the range of small to moderate strains (λ_x between 1 and 1.3). The better performance of the Yeoh-Fleming model compared to the Gent-Gent, Carroll, and Yeoh formulations is not surprising. Indeed, the Yeoh-Fleming model has four parameters, whereas the Gent-Gent, Carroll, and Yeoh formulations only have three. On the other hand, the Ogden model counts for four parameters as well but it results inaccurate to reproduce the response of NBR rubber. The better performance of the Yeoh-Fleming model can be interpreted in light of its

design. Indeed, by combining two terms, one responsible for small strains and one responsible for large strains, the Yeoh-Fleming model results accurate for both small and large strains.

The above results presented above indicate the Yeoh-Fleming model as the most suitable model to be assumed as deviatoric part W_d of the SED. In the next section, the Yeoh-Fleming model is coupled with the volumetric SED proposed in Section 5.3 to provide a complete description of the response of elastomers at large deformations.

In conclusion, it is worth to remark that many more incompressible strain energy functions have been proposed in the literature. A comprehensive review of the proposed isotropic hyperelastic constitutive models for rubber-like materials is found in Dal et al. [120]. It goes without saying that formulations different from the Yeoh-Fleming may be used. For instance, when dealing with soft tissues in problems of biomechanics, other hyperelastic models for W_d may be preferred [121, 122].

5.5 The combined SED

In the previous sections, the split of the strain energy function was adopted and suitable formulations for both volumetric and deviatoric parts of the SED were investigated. In particular, in Section 5.3 a new formulation for the volumetric part W_h of the SED was proposed. The proposed SED is capable of reproducing accurately the σ_h vs. J curves for all the elastomers tested. In Section 5.4, the Yeoh-Fleming model was selected as deviatoric part among the most popular models in the literature. The analysis was done by assuming material incompressibility, since the interest was capturing the shape-changing deformations of rubbers.

In the present section, the above deviatoric and volumetric parts W_d and W_h are combined. The combined SED is introduced and a final fitting of the model parameters is carried out on the experimental data. The combined SED gives the complete description of both shape and volume deformations of rubbers.

5.5.1 The combined SED formulation

The combined SED is obtained by coupling the volumetric part and the deviatoric part

$$W = W_d\left(\bar{I}_1\right) + W_h(J), \tag{5.28}$$

where

$$W_d\left(\bar{I}_1\right) = \frac{A}{B}\left(I_m - 3\right)\left(1 - e^{-B(\bar{I}_1-3)/(I_m-3)}\right) - C_{10}\left(I_m - 3\right)\ln\left(1 - \frac{\bar{I}_1-3}{I_m-3}\right) \tag{5.29}$$

and $W_h(J)$ is given by Eq. (5.16). Note that the Yeoh Fleming model is written as a function of the deviatoric invariant $\bar{I}_1$, defined in Eq. (5.3), consistently with the approach of the split of the strain energy function.

Thanks to the split of the energy function, the calibration of the fitting parameters for the volumetric part of the SED is entirely independent from the deviatoric contribution. Indeed, the hydrostatic stress σ_h only depends on W_h, and once known the σ_h vs. J curve, function W_h can be completely determined. However, the same

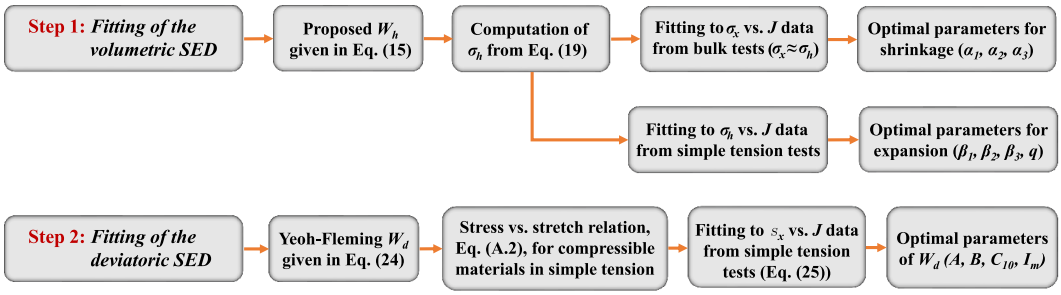

Figure 5.12: Summary of the steps for fitting the parameters of volumetric and deviatoric parts of the combined SED proposed in this work.

rule does not apply to the deviatoric part of the SED. Indeed, since in finite elasticity a shape-changing deformation always implies a volume change, the effect of W_d can never be completely separated from the contribution of W_h. The calibration of the parameters of the SED in simple tension requires the computation of stress s_x (or σ_x), which depends on both W_d and W_h. Hence, the correct procedure for the material characterization consists in: 1) firstly the parameters of W_h are calibrated from the σ_h vs. J curve. The response in expansion derives from the simple tension test, the response in shrinkage comes from the bulk test under the approximation $\sigma_x \approx \sigma_h$; 2) then, the parameters of W_d are calibrated by fitting to experimental data the solution for compressible materials in simple tension.

The parameters of the volumetric part W_h were calibrated in Section 5.3 and are listed in Tab. B.2. In the following, the parameters of the Yeoh-Fleming model are calibrated on the basis of the experimental data in simple tension. The equilibrium solution in simple tension for compressible materials is expressed by Eqs. (A.1) and (A.2). The first is an implicit equation that allows to compute numerically the lateral stretch λ_y as a function of longitudinal stretch λ_x. The second equation gives the expression of nominal stress s_x as a function of longitudinal stretch λ_x. The equilibrium solution for the bulk test is expressed by Eqs. (A.5) and (A.6). It is important to remark that in Section 5.5 the fitting parameters of the proposed function W_h were calibrated by using such the approximation $\sigma_x \approx \sigma_h$. In the present section, since deviatoric and volumetric contributions are coupled, the real stress σ_x is computed by using the exact solution from Eq. (A.5). The overall procedure for parameter fitting is summarized in the scheme shown in Fig. 5.12.

5.5.2 Fitting of the combined SED to experimental data

The fitting process is performed using MATLAB. The experimental data from simple tension tests are imported as stress s_{x_i} and stretch λ_{x_i}, where $i = 1, ..., n$ and n is the number of experimental data points. The constitutive parameters of the Yeoh-Fleming model are gathered in the parameter vector $\mathbf{p} = [A, B, C_{10}, I_m]$. The equilibrium equations in simple tension, expressed by Eqs. (A.1) and (A.2), are implemented in a MATLAB function. The implicit equation (A.1) is solved using *fsolve* to obtain for all data λ_{x_i} the corresponding values of lateral stretch $\lambda_{y_i}(\mathbf{p})$.

The obtained values $\lambda_{y_i}(\mathbf{p})$ were inserted in Eq. (A.2) to compute the stress function $s_x(\lambda_{x_i}, \lambda_{y_i}(\mathbf{p}), \mathbf{p})$. Then, the following objective function was defined:

$$\text{obj}(\mathbf{p}) = \sqrt{\sum_{i}^{n} (s_x(\lambda_{x_i}, \lambda_{y_i}(\mathbf{p}), \mathbf{p}) - s_{x_i})^2}. \tag{5.30}$$

Hence, the optimal parameters are those that minimize the sum of squared residuals between analytical and experimental stress vs. stretch curves.

The minimization of Eq. (5.30) is carried out using function *fmincon*. The initial guess for the parameter vector is $\mathbf{p}_0 = [0.5, 0.01, 1, 2]$. The lower and upper bounds for the parameters are defined respectively as $\mathbf{p}_l = [0, 0, 0, 0]$ and $\mathbf{p}_u = [10, 1, 10, 20]$. The optimal parameters obtained from the optimization are reported in Tab. B.4. The equilibrium solutions for bulk and simple tension tests are finally computed with the optimal parameters and the final results for each rubber are shown in Fig. 5.13.

The left column of Fig. 5.13 shows the σ_x vs. J curves for $J \leq 1$ in comparison with the experimental data from bulk tests. In Section 5.3, the true stress σ_x was approximated to σ_h for the calibration of the parameters of W_h. (see Fig. 5.7). Here, since the volumetric and deviatoric contributions are combined, the exact solution of the bulk test is computed from Eq. (A.5) in terms of σ_x vs. J relation. The approximation $\sigma_x \approx \sigma_h$ for rubber-like materials is validated by the above plots. Indeed the curves are identical to the left column of Fig. 5.7 and the combined SED results accurate. The plots in the middle and right columns of Fig. 5.13 show respectively the s_x vs. λ_x and λ_y vs. λ_x curves in comparison with the experimental data from simple tension tests. The results indicate that the model describes accurately the response in simple tension of all four rubbers considered, being able to capture significant volume changes as occurs in the case of EPDM and NBR rubbers.

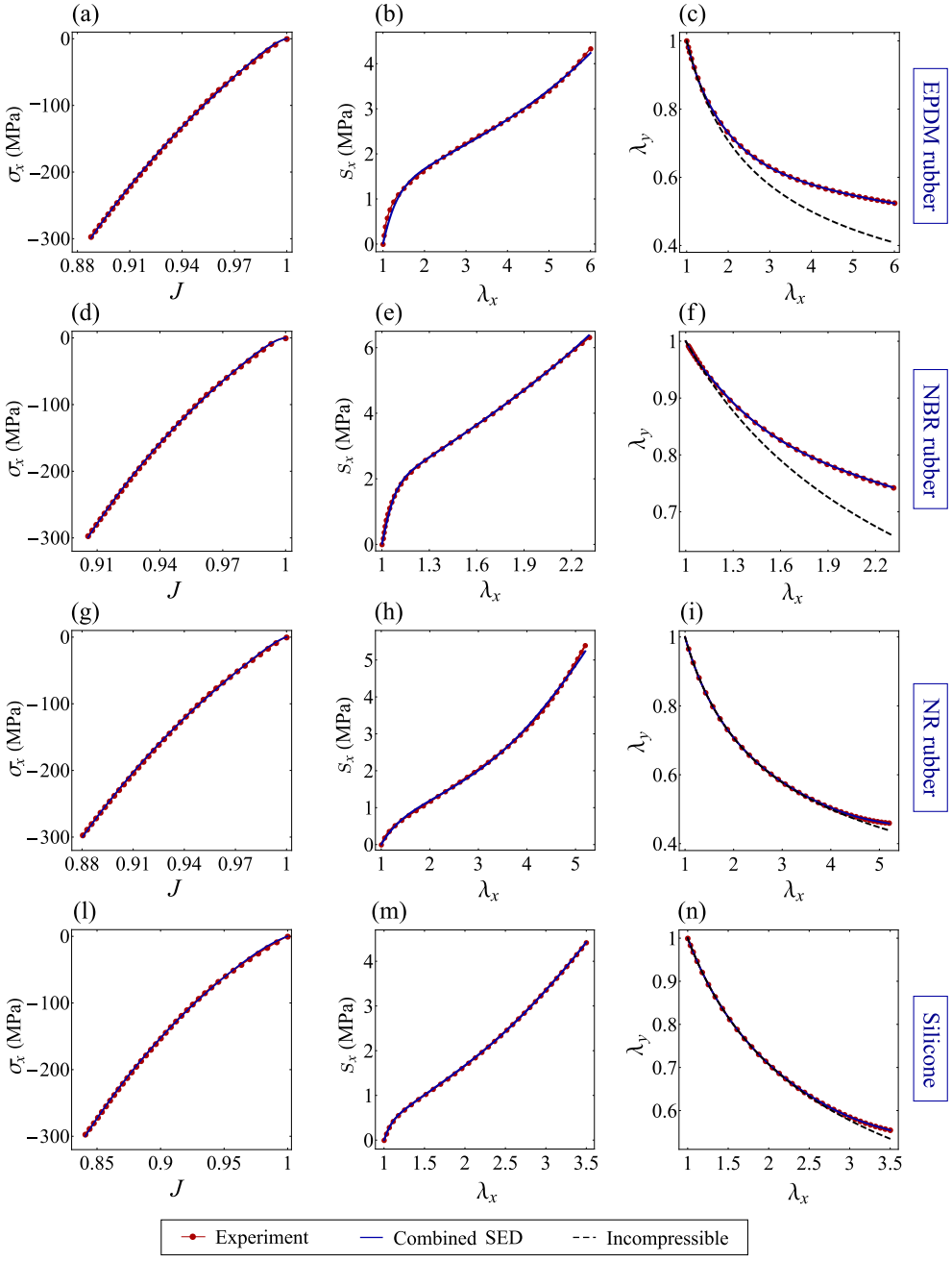

Figure 5.13: Results of the combined SED formulation, given by Eq. (5.28). The results are shown for (a)-(c) EPDM, (d)-(f) NBR, (g)-(i) NR and (l)-(n) silicone. The σ_x vs. J experimental data come from the bulk tests, while the s_x vs. λ_x and λ_y vs. λ_x from the simple tension tests.

6 Effect of compressibility on the mechanics of membranes

In this chapter, the proposed SED is adopted to study the effect of compressibility on the mechanical response of inflated membranes. As shown in Chapter 5, despite the usual assumption of incompressibility, some elastomers can exhibit significant volume changes. The experimental results presented in Section 5.1 show volume expansion up to 60% in simple tension and volume shrinkage of 15% during volumetric compression, depending on the elastomer compound. This chapter aims to provide a comprehensive investigation of the effect of compressibility on the mechanical response of inflatable membranes. To this purpose, different degrees of material compressibility are considered. Besides studying materials compressible at large deformations, like the EPDM and NBR rubbers tested in Chapter 5, the attention here is extended to soft materials like polymeric foams, gels and auxetic materials. These materials are compressible since the range of small deformations, and are being employed in increasingly numerous applications.

Hong et al. [123] formulated a theory of the coupled mass transport and large deformations for polymeric gels in the framework of hyperelasticity. Ding et al. [124] presented equilibrium equations and implemented finite element analysis for inhomogeneous large deformations in temperature-sensitive hydrogels. Their investigation underscored the versatility of hydrogel membranes, demonstrating potential applications ranging from wound healing to soft robotics. Ahearne et al. [125] employed the indentation method to characterize the viscoelastic properties of alginate and agarose hydrogel circular membranes. Liu et al. [7] conducted a hyperelastic model study on instabilities in various polymeric gel membrane structures under large deformations. The biocompatibility of these membranes holds promise for applications in bioengineering and drug delivery. In [126], two-component soft cellular polyurethane membranes were utilized to reduce airflow in injured inflatable structures. Pientka et al. [8] employed a flexible closed-cell polystyrene foam membrane for effective biohydrogen separation. Elele et al. [127] conducted experiments on polymeric microfiltration membranes with pores, designed for water treatment.

Given these considerations, accurate nonlinear material models considering compressibility are necessary. Some authors attempted to introduce material compressibility when modeling hyperelastic membranes [128–130]. The current compressible formulations, as well as the model used in Sections 2.4.2, suffer of severe limitantions. First of all, the volumetric functions were developed for nearly incompressible elastomers, thus resulting inadequate for accurately describing the material response under large volume changes. Moreover, they do not meet the validity criteria listed in Tab. 5.2. In addition, they were not based on the split of the SED. Therefore, the contribution of volumetric deformations was not explicitly determined.

Contrary to these limitations, the following analysis presents the following ad-

vantages:

- The split of the strain energy density function into its deviatoric and volumetric parts allows a clear definition of the effect of volumetric deformations on the mechanical response of membranes;
- The parameters of the volumetric SED are calibrated on the real response of materials to volume changes.

Three benchmark problems are considered: 1) inflation of a circular flat membrane; 2) inflation of an infinite thin-walled cylindrical tube; 3) inflation of a thin-walled spherical balloon. The classic equilibrium solutions are extended to the case of compressible materials, where the transversal stretch must be computed by an implicit relation. The effect of compressibility is analyzed and discussed by comparing these solutions with classical solutions of membrane problems under the assumption of material incompressibility.

6.1 Materials investigated and parameters calibration

This section presents the materials considered in the analysis of compressibility in membrane problems. Four different classes of materials are considered, characterized by an increasing degree of compressibility. The parameters of the proposed SED are fitted to experimental data obtained from simple tension tests for all the materials considered. During the calibration of model parameters, both the cases of compressible and incompressible material are considered. Indeed, the purpose of the following sections is to compare the compressible and incompressible responses to benchmark problems of inflated membranes.

6.1.1 Description of the materials

The aim of the following analyses is to observe the effect of compressibility on the response of inflated membranes. To this purpose, four different types of materials are considered: (I) materials that are nearly incompressible for any magnitude of applied strain; (II) materials that are nearly incompressible for small strains and become compressible for large strains; (III) materials that are compressible for both small and large strains; (IV) auxetic materials. The NR rubber and silicone analyzed in Chapter 5 belong to category I, as can be seen from Fig 6.1(d). On the other hand, the EPDM and NBR can be classified as type II materials, being incompressible for small strains and becoming compressible at large strains. The polymeric foam and the hydrogel tested respectively in works [78] and [131] are regarded as type III materials. As shown in Fig. 6.1, these materials exhibit volume changes even at small strains. Finally, as a type IV material, the foam analyzed in [132] is considered. It is important to remark that the purpose is to shed light on the role of material compressibility on the response of inflatable elastic membranes. It is clear that for materials of type III and IV the assumption of incompressibility is inappropriate from a theoretical standpoint. However, the differences between compressible and

incompressible response are emphasized when the material is characterized by a marked compressibility. In addition, direct approaches for the solution of membrane problems characterized by a marked compressibility have not yet been proposed in the literature.

Figure 6.1 shows the experimental data of the materials described above. The stress attained by materials of type III and IV is significantly lower than the elastomers. Therefore, for the sake of clarity, the nominal stress of materials of type III and IV is normalized with respect to the following values of Young modulus: $E = 650$ kPa for the foam, $E = 1.9$ kPa for the hydrogel and $E = 15$ kPa for the auxetic foam. The black curves in Figs. 6.1(d) and 6.1(e) represent the incompressible behavior, expressed by $\lambda_y = 1/\sqrt{\lambda_x}$. Figure 6.1(f) shows the typical trend of an auxetic material, with the specimen that expands laterally when subjected to simple tension in the longitudinal direction.

6.1.2 Calibration of model parameters

The constitutive parameters for NR, silicone, EPDM and NBR for both compressible and incompressible models were fitted in Chapter 5 and are reported in Tabs. B.3 and B.4 respectively. Materials of type II and III are fitted according to the same procedure, which is remarked in the following.

For the parameters of the compressible model, the fitting is performed in two steps:

(i) The parameters of the volumetric part W_h are calibrated by fitting the σ_h vs. J curve deriving from the experimental data in simple tension. For each material, the bulk modulus κ is calibrated from the initial slope of the curve. Parameters β_1, β_2, β_3 and q are then calibrated by fitting the entire σ_h vs. J curve. The fitting is performed by means of function *FindFit* in Wolfram Mathematica. It is important to notice that only the branch of volume expansion of the volumetric curve is of interest, since membranes can only experience tensile stress. For this reason, the parameters responsible of volume shrinkage, namely α_1, α_2 and α_3, are neglected and the volumetric SED reduces to $W_h = \kappa \Psi_t(J)$.

(ii) The parameters of the deviatoric part W_d are calibrated by fitting the experimental data in simple tension, according to the equilibrium solution described by Eqs. (A.1) and (A.2). In particular, the above equations are written in a MATLAB code. Function *fsolve* is employed to numerically solve the implicit equation between longitudinal and lateral stretches, Eq. (A.1). Successively, the stress vs. stretch relation, expressed by Eq. (A.2), is fitted to the s_x vs. λ_x data. The sum of squared residuals between analytical and experimental stress is considered as objective function, and the optimization is perfomed with function *fmincon*.

For the incompressible model, the stress vs. strain relation is given by Eq. (A.3). The parameters of the Yeoh-Fleming strain energy function are calibrated by fitting this relation to the experimental stress vs. stretch data using function *FindFit* in Wolfram Mathematica.

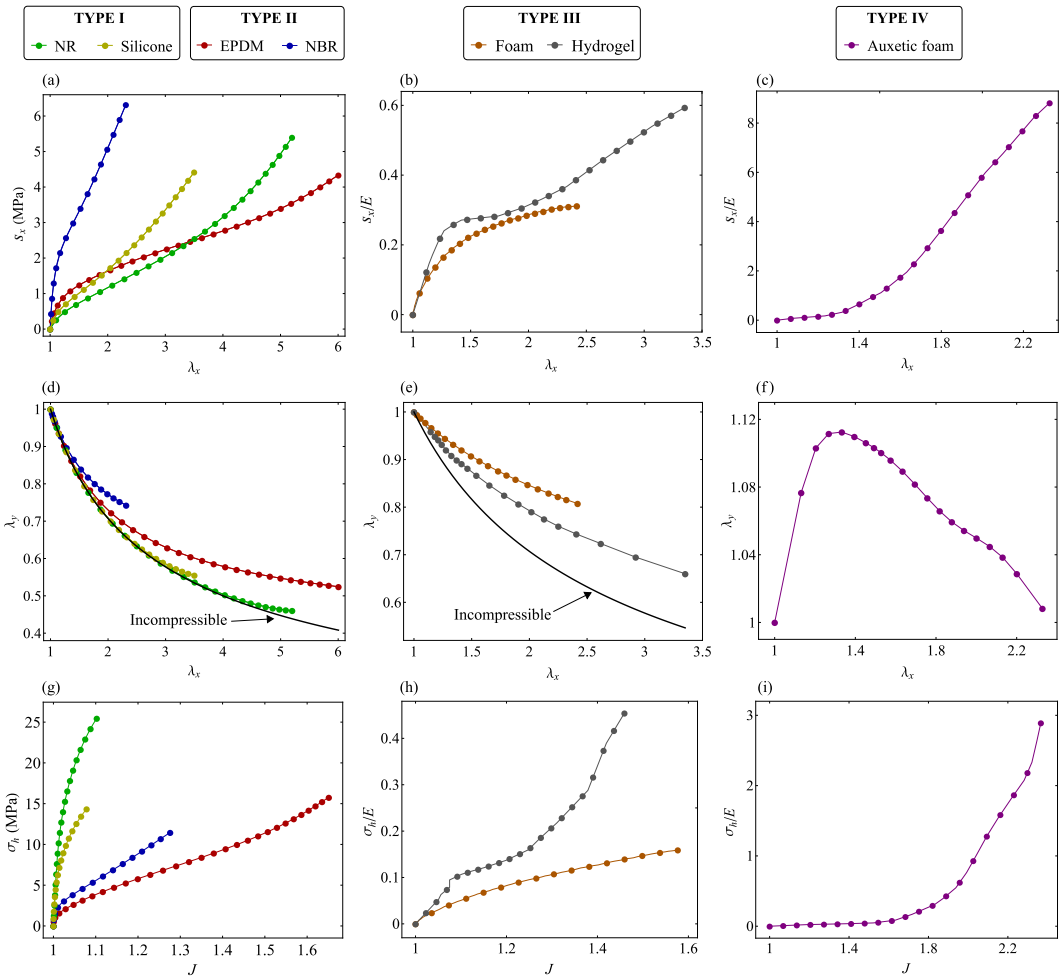

Figure 6.1: Experimental data from simple tension tests: (a)-(c) nominal stress vs. stretch; (d)-(f) lateral stretch vs. longitudinal stretch; (g)-(i) hydrostatic stress vs. volume variation. The experiments on elastomers are described in detail in Section 5.1.1. The data of foam, hydrogel and auxetic foam were digitized respectively from Blatz and Ko [78], Urayama et al. [131], and Choi and Lakes [132]. The values of nominal stress for materials of type III and IV are normalized to the following values of Young Modulus: $E = 650$ kPa for the foam, $E = 1.9$ kPa for the hydrogel, $E = 15$ kPa for the auxetic foam.

The optimal parameters of the soft materials analyzed are reported in Tab. B.5. Figure 6.2 shows the curves obtained from the incompressible and compressible models for materials of type III and IV. Figures 6.2(a) and 6.2(b) show the normalized stress vs. stretch curves for materials of type III and IV with incompressible model, respectively. On the other hand, Figs. 6.2(c) and 6.2(d) show the normalized stress vs. stretch curves in the case of compressible model. Both incompressible and compressible models give accurate predictions of the tensile stress response of the materials analyzed. For the compressible model, the laterals stretch vs. longitudinal stretch curves and the volumetric curves are shown in Figs. 6.2(e), 6.2(f), 6.2(g) and 6.2(h). The predictions of the model result accurate for both the lateral stretch and the hydrostatic stress, proving the effectiveness of the proposed SED for compressible materials different from elastomers.

6.2 Equilibrium solutions for the inflation of compressible membranes

The effect of compressiblity on the inflation of elastic membranes is analysed by studying three benchmark problems in nonlinear elasticity: (1) inflation of a circular flat membrane; (2) inflation of an infinitely long thin-walled cylindrical tube; (3) inflation of a thin-walled spherical balloon. A schematic representation of the three problems is reported in Fig. 6.3. The equilibrium solutions for these problems are reported in the following sections, for both compressible and incompressible case. The combined SED proposed in Chapter 5 is used for the compressible case, whereas the Yeoh-Fleming model is used for the incompressible case. In case of the combined SED, $W = W(\bar{I}_1, J)$, the derivatives of W with respect to the principal strain invariants I_1, I_2 and I_3 are computed with the chain rule and read

$$
\begin{aligned}
w_1 &= \frac{1}{I_3^{1/3}}\left(Ae^{-\frac{B\left(I_1 I_3^{-1/3}-3\right)}{I_m-3}} + C_{10}\left(1-\frac{I_1 I_3^{-1/3}-3}{I_m-3}\right)^{-1}\right),\\
w_2 &= 0,\\
w_3 &= -\frac{I_1}{3I_3^{4/3}}\left(Ae^{-\frac{B\left(I_1 I_3^{-1/3}-3\right)}{I_m-3}} + C_{10}\left(1-\frac{I_1 I_3^{-1/3}-3}{I_m-3}\right)^{-1}\right)\\
&\quad + \frac{\kappa}{2J}\left((1-q)\frac{e^{\beta_1(J-1)}-e^{\beta_2(1-J)}}{\beta_1+\beta_2} + \beta_3 q\tanh\left(\frac{J-1}{\beta_3}\right)\right).
\end{aligned}
\tag{6.1}
$$

For the incompressible Yeoh-Fleming model, $W = W(I_1)$ and the derivative with respect to I_1 reads

$$
w_1 = Ae^{-\frac{B(I_1-3)}{I_m-3}} + C_{10}\left(1-\frac{I_1-3}{I_m-3}\right)^{-1}, \tag{6.2}
$$

with $w_2 = w_3 = 0$.

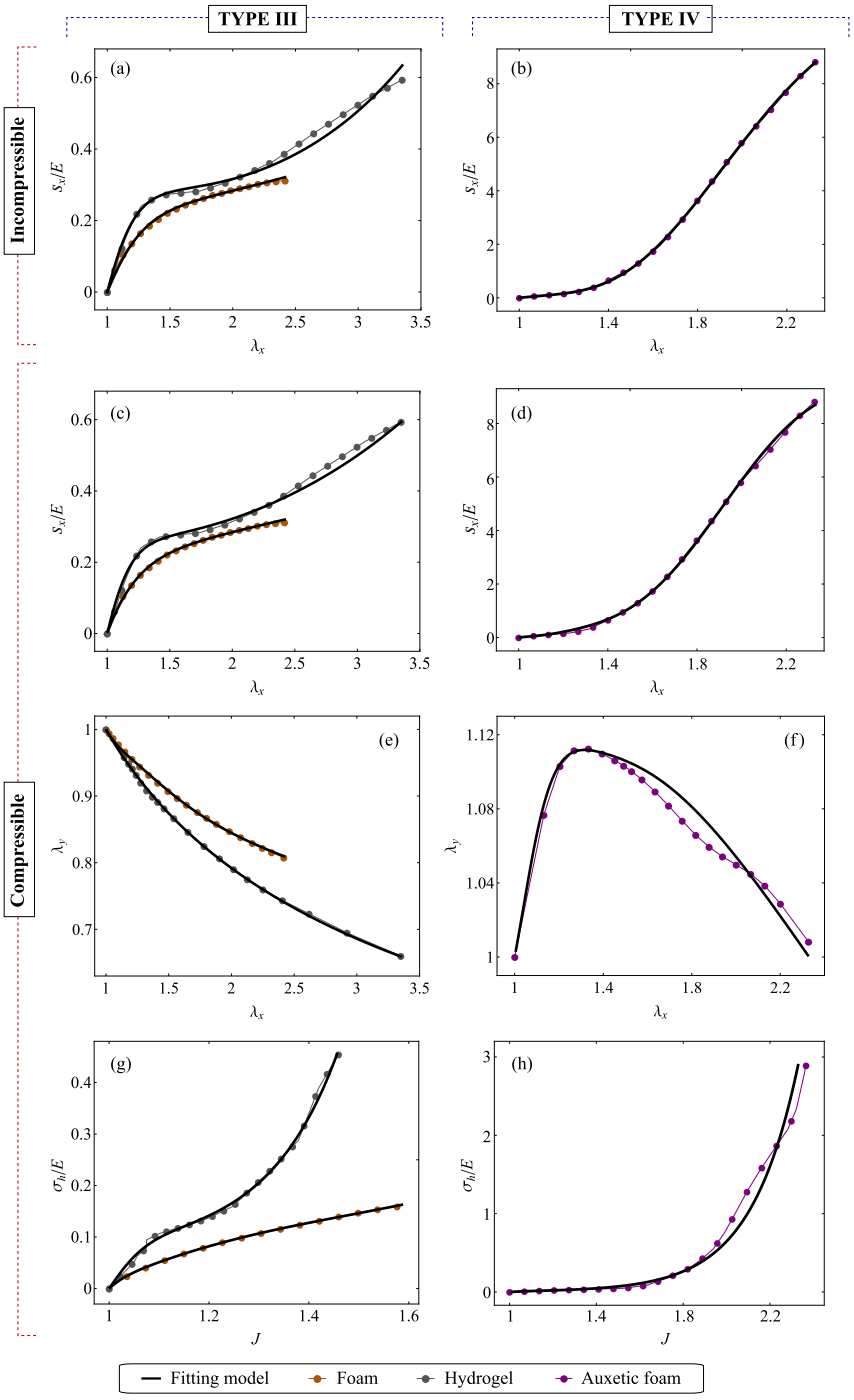

Figure 6.2: Results of model fitting in case of incompressible and compressible models for materials of type III and IV. Stress vs. stretch plots for incompressible, (a) and (b), and compressible models, (c) and (d). For the compressible model, the plots of λ_y vs. λ_x and σ_h/E vs. J are shown respectively in (e) and (f), and (g) and (h). Continuous and dotted lines represent model fitting and experimental data, respectively.

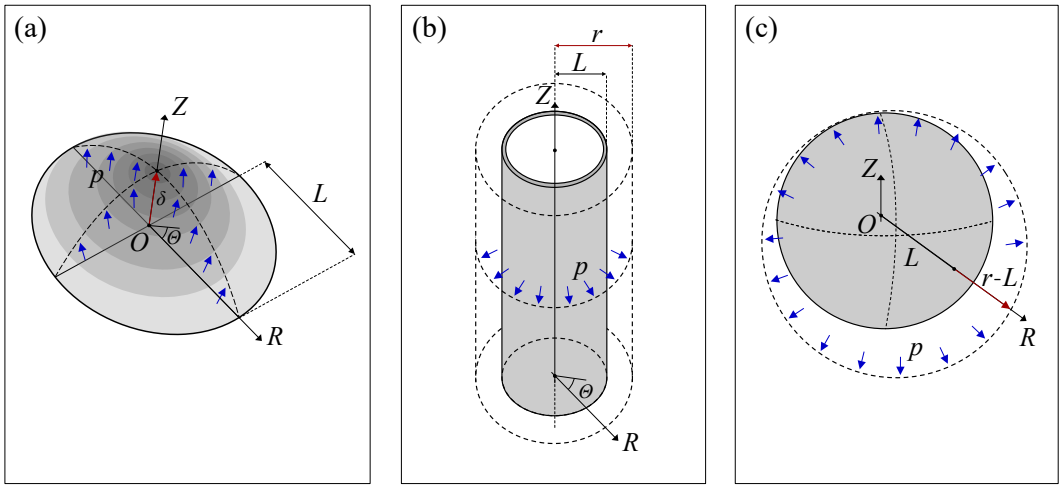

Figure 6.3: Schematic representation of the three problems of inflated membranes: (a) inflation of a circular flat membrane; (b) inflation of an infinitely long thin-walled cylindrical tube; (c) inflation of a thin-walled spherical balloon.

6.2.1 Inflation of circular membranes

The problem of the inflation of a circular membrane was introduced in Chapter 2. Here, the governing equations are extended to the case of the most generic compressible material, for which the tranversal stretch λ_3 is linked to the principal stretches λ_1, λ_2 by an implicit relation. The principal stretches and the principal Cauchy stresses are defined by Eqs. (2.1) and (2.6), respectively. The plane stress condition $\sigma_3 = \partial W/\partial\lambda_3 = 0$ leads to the following relation for λ_3

$$G(\lambda_1,\lambda_2,\lambda_3) = \frac{\partial W}{\partial \lambda_3} = w_1 + \left(\lambda_1^2+\lambda_2^2\right) w_2 + \lambda_1^2\lambda_2^2 w_3 = 0 \tag{6.3}$$

For each pair (λ_1,λ_2), Eq. (6.3) must be solved numerically to the determine the corresponding λ_3.

The principal stress resultants per unit length read

$$\begin{aligned} T_1 &= \frac{2H\lambda_1\left(w_1+\left(\lambda_2^2+\lambda_3^2\right)w_2+\lambda_2^2\lambda_3^2 w_3\right)}{\lambda_2}, \\ T_2 &= \frac{2H\lambda_2\left(w_1+\left(\lambda_1^2+\lambda_3^2\right)w_2+\lambda_1^2\lambda_3^2 w_3\right)}{\lambda_1}, \end{aligned} \tag{6.4}$$

which inserted in the equilibrium equations (2.11) and (2.12) lead to the governing system

$$\begin{aligned} \lambda_1' &= \frac{\xi_0+\xi_1 w_1+\xi_2 w_2+\xi_3 w_3}{w_1+w_2\xi_4+w_3\xi_5+\frac{\partial w_1}{\partial\lambda_1}\lambda_1+\frac{\partial w_2}{\partial\lambda_1}\lambda_1\lambda_2^2+\frac{\partial w_2}{\partial\lambda_1}\lambda_1\lambda_3^2+\frac{\partial w_3}{\partial\lambda_1}\lambda_1\lambda_3^2\lambda_2^2}, \\ \lambda_2' &= \frac{\eta-\lambda_2}{R}, \\ \eta' &= \frac{\eta\lambda_1'}{\lambda_1}+\frac{2\zeta_1\lambda_2\left(\lambda_1^2-\eta^2\right)-\phi\lambda_2\lambda_1^2\sqrt{\lambda_1^2-\eta^2}}{2\zeta_2\lambda_1^2 R}, \end{aligned} \tag{6.5}$$

where $\phi = pR/H$ and, for the sake of clarity, the following quantities were defined:

$$
\begin{aligned}
\xi_0 &= \lambda_1^2 \frac{\partial w_1}{\partial \lambda_2}(\lambda_2 - \eta) + \lambda_1^2 \frac{\partial w_2}{\partial \lambda_2}\left(-\eta\lambda_2^2 - \eta\lambda_3^2 + \lambda_2^3 + \lambda_3^2\lambda_2\right) + \lambda_1^2\lambda_3^2\lambda_2^2 \frac{\partial w_3}{\partial \lambda_2}(\lambda_2 - \eta),\\
\xi_1 &= \eta\lambda_2 - \lambda_1^2,\\
\xi_2 &= -2\frac{\partial \lambda_3}{\partial \lambda_2}\eta\lambda_3\lambda_1^2 + 2\frac{\partial \lambda_3}{\partial \lambda_2}\lambda_2\lambda_3\lambda_1^2 - \eta\lambda_2\lambda_1^2 + \eta\lambda_2\lambda_3^2 + \lambda_2^2\lambda_1^2 - \lambda_3^2\lambda_1^2,\\
\xi_3 &= -2\frac{\partial \lambda_3}{\partial \lambda_2}\eta\lambda_1^2\lambda_3\lambda_2^2 + 2\frac{\partial \lambda_3}{\partial \lambda_2}\lambda_1^2\lambda_3\lambda_2^3 - \eta\lambda_1^2\lambda_3^2\lambda_2 + \lambda_1^2\lambda_3^2\lambda_2^2,\\
\xi_4 &= 2\frac{\partial \lambda_3}{\partial \lambda_1}\lambda_1\lambda_3 + \lambda_2^2 + \lambda_3^2,\\
\xi_5 &= 2\frac{\partial \lambda_3}{\partial \lambda_1}\lambda_1\lambda_3\lambda_2^2 + \lambda_3^2\lambda_2^2,\\
\zeta_1 &= w_1 + \lambda_1^2 w_2 + \lambda_3^2\left(\lambda_1^2 w_3 + w_2\right),\\
\zeta_2 &= w_1 + \lambda_2^2 w_2 + \lambda_3^2\left(\lambda_2^2 w_3 + w_2\right).
\end{aligned}
\tag{6.6}
$$

The partial derivatives of λ_3 with respect to λ_1 and λ_2 can only be computed numerically by means of the implicit function theorem, namely

$$
\frac{\partial \lambda_3}{\partial \lambda_1} = -\frac{\partial G/\partial \lambda_1}{\partial G/\partial \lambda_3}, \quad \frac{\partial \lambda_3}{\partial \lambda_2} = -\frac{\partial G/\partial \lambda_2}{\partial G/\partial \lambda_3}. \tag{6.7}
$$

The derivatives of w_1, w_2 and w_3 with respect to λ_1 and λ_2 are computed with the chain rule

$$
\frac{\partial w_i}{\partial \lambda_j} = \sum_{k=1}^{3} \frac{\partial w_i}{\partial I_k}\left(\frac{\partial I_k}{\partial \lambda_j} + \frac{\partial I_k}{\partial \lambda_3}\frac{\partial \lambda_3}{\partial \lambda_j}\right), \qquad i = 1,2,3 \ \text{ and } \ j = 1,2. \tag{6.8}
$$

The integration of the governing differential equations for the case of incompressible materials was outlined in Section 2.3. Here, the integration is more demanding since the transversal stretch λ_3 must be computed iteratively at every point of the domain. The overall procedure is the following: (i) the initial condition at the pole λ_0 and a guess value p_0 for the pressure are set; (ii) the corresponding transversal stretch λ_3 is computed solving numerically Eq. (6.3) with $\lambda_1 = \lambda_2 = \lambda_0$; (iii) quantities $\partial\lambda_3/\partial\lambda_1$, $\partial\lambda_3/\partial\lambda_2$, $\partial w_1/\partial\lambda_1$, $\partial w_1/\partial\lambda_2$, $\partial w_2/\partial\lambda_1$, $\partial w_2/\partial\lambda_2$, $\partial w_3/\partial\lambda_1$ and $\partial w_3/\partial\lambda_2$ are computed from Eqs. (6.7) and (6.8); (iv) the values of λ_1, λ_2 and η at the next point of the domain are computed from Eq. (6.5); (v) steps (ii), (iii) and (iv) are repeated for each point along the domain until $\lambda_2 = 1$. The value of R at which $\lambda_2 = 1$ is denoted by R^*; (vi) in general, the initial guess value p_0 will be different from the correct pressure p and thus R^* will be different from L. However, system (6.5) is invariant when a scaling factor is multiplied to R. Hence we choose $\gamma = L/R^*$ as scaling factor and we compute the correct value of pressure as $p_1 = p_0/\gamma = p_0 R^*/L$; (vii) perform again the numerical integration with the correct value p_1 and obtain the correct stretches profiles λ_1 and λ_2. The deformed profile can be determined from relations (2.1); (viii) repeat this procedure for different initial conditions λ_0 to derive the entire pressure curve. The integration is performed in MATLAB by means of function *ode45*, with an integration step $dR = L/1000$.

For each material, it is necessary to define the maximum stretch $\lambda_{0,max}$ to apply at the pole as initial condition. This choice requires attention in order to avoid a level of deformation higher than the one attained during the parameters calibration. Since the parameters were calibrated on uniaxial tensile tests, a natural choice for the value of $\lambda_{0,max}$ would be the maximum longitudinal stretch $\lambda_{x,max}$ reached in the experimental tests. However, since membrane inflation is a biaxial problem, the overall strain state would differ substantially from the case of uniaxial tension. Therefore, a global measure of deformation seems more appropriate. To this aim, the first deviatoric invariant $\bar{I}_1$ is assumed as measure of deformation. Thereby, $\lambda_{0,max}$ is set in such a way that $\bar{I}_1$ computed at the pole of the membrane matches the value of $\bar{I}_1$ at the end of the uniaxial tensile test. The choice of $\bar{I}_1$ is supported by the observation that it is the only independent variable of the Yeoh-Fleming model. This approach guarantees that the range of reliability of the fitted model parameters is never exceeded. The maximum stretch $\lambda_{0,max}$ determined with this approach is adopted also for the inflation of the cylindrical tube and the spherical balloon, described in the following.

6.2.2 Inflation of cylindrical tubes

The second problem consists in the inflation of an infinitely long, thin-walled cylindrical tube. In the undeformed configuration, the tube has uniform thickness H and radius L, as shown in Fig. 6.3(b). During inflation, the deformed configuration is assumed axialsymmetrical and the axial stretch at infinity is kept fixed to unity. The deformed radius can either remain constant (uniform solution) or vary along the axial direction (bifurcated state). In the following, the uniform solution and the bifurcation condition are presented [133].

A generic material point $P \equiv (L, \Theta, Z)$ is mapped into P', with coordinates $(r(Z), \Theta, z(Z))$. The meridional, latitudinal and normal directions are the principal directions of strain, and the principal stretches read

$$\lambda_1 = \sqrt{r'^2 + z'^2}, \quad \lambda_2 = \frac{r}{L}, \quad \lambda_3 = \frac{h}{H}. \tag{6.9}$$

Here the prime denotes differentiation with respect to Z.

The principal Cauchy stresses are given by Eq. (2.6). The membrane assumption $\sigma_3 = \partial W/\partial\lambda_3 = 0$ gives again Eq. (6.3), which relates the transversal stretch λ_3 to λ_1 and λ_2. The equilibrium equations are [134]

$$\frac{1}{h}\frac{d(h\sigma_1)}{dZ} + \frac{r'}{r}(\sigma_1 - \sigma_2) = 0, \tag{6.10}$$

$$\frac{\sigma_1 (r''z' - r'z'')}{(r'^2 + z'^2)^{\frac{3}{2}}} - \frac{\sigma_2 z'}{r\,(r'^2 + z'^2)^{\frac{1}{2}}} + \frac{p}{h} = 0. \tag{6.11}$$

Pipkin [135] showed that, in case of axisymmetric deformations of an axisymmetric membrane, Eq. (6.10) can be integrated to obtain

$$W - \lambda_1 \frac{\partial W}{\partial \lambda_1} = C_1 \tag{6.12}$$

where C_1 is a costant. For this problem, Eq. (6.11) can also be integrated giving [134]

$$\frac{1}{\lambda_1}\frac{\partial W}{\partial \lambda_1}z' - \frac{p\lambda_2^2 L}{2H} = C_2 \tag{6.13}$$

where C_2 is a second integration constant.

Defining the normalized pressure $\bar{p} = pL/H$, and assuming that the tube remains uniform far away from the origin with a constant radius r_∞, namely

$$r \to r_\infty,\ r' \to 0,\ r'' \to 0,\ z \to Z,\ z' \to 1,\ \lambda_1 \to 1,\ \lambda_2 \to r_\infty/L \quad \text{as} \quad Z \to \pm\infty, \tag{6.14}$$

constants C_1, C_2 and the pressure p are determined from Eqs. (6.12), (6.13) and (6.11)

$$C_1 = W^{(\infty)} - \frac{\partial W}{\partial \lambda_1}^{(\infty)}, \tag{6.15}$$

$$C_2 = \frac{\partial W}{\partial \lambda_1}^{(\infty)} - \frac{\bar{p}\lambda_{2,\infty}^2}{2}, \tag{6.16}$$

$$\bar{p} = \frac{1}{\lambda_{2,\infty}}\frac{\partial W}{\partial \lambda_2}^{(\infty)}, \tag{6.17}$$

where the superscript (∞) means evaluation at $\lambda_1 = 1$ and $\lambda_2 = r_\infty/L = \lambda_{2,\infty}$. Equation (6.17) gives the $\bar{p}$ vs. $\lambda_{2,\infty}$ curve in case of uniform inflation. The solution is obtained numerically by defining in MATLAB a vector of values of $\lambda_{2,\infty}$, ranging from 1 to $\lambda_{0,max}$. For each value of $\lambda_{2,\infty}$, Eq. (6.3) is expressed as $G(1, \lambda_{2,\infty}, \lambda_3) = 0$ and it is solved numerically using MATLAB function *fsolve* to find the transversal stretch λ_3 which satisfies the membrane assumption. The obtained value of λ_3 is then substituted into Eq. (6.17) to compute the external pressure.

As $\lambda_{2,\infty}$ increases the uniform solution may reach a bifurcation point after which a bulging/necking of the tube takes place. The bulge profile is determined from Eqs. (6.12) and (6.13), which are two coupled first order differential equations for $r(Z)$ and $z(Z)$. The bifurcation condition reads [133]

$$\lambda_{2,\infty}\left(\frac{\partial W}{\partial \lambda_2}^{(\infty)} - \frac{\partial^2 W}{\partial \lambda_2 \partial \lambda_1}^{(\infty)}\right)^2 + \frac{\partial^2 W}{\partial \lambda_1^2}^{(\infty)}\left(\frac{\partial W}{\partial \lambda_2}^{(\infty)} - \lambda_{2,\infty}\frac{\partial^2 W}{\partial \lambda_2^2}^{(\infty)}\right) = 0. \tag{6.18}$$

When computing the second derivatives $\partial^2 W/\partial\lambda_i\partial\lambda_j$, the dependence of λ_3 on λ_1 and λ_2 must be taken into account, writing

$$\frac{\partial^2 W}{\partial \lambda_i \partial \lambda_j} = \sum_{k=1}^{3}\frac{\partial^2 W}{\partial \lambda_i \partial I_k}\left(\frac{\partial I_k}{\partial \lambda_j} + \frac{\partial I_k}{\partial \lambda_3}\frac{\partial \lambda_3}{\partial \lambda_j}\right), \qquad i,j = 1,2 \tag{6.19}$$

where $\partial\lambda_3/\partial\lambda_j$ are given by Eq. (6.7). The value of $\lambda_{2,\infty} = r_\infty/L$ satisfying Eq. (6.18) determines the critical radius that leads to the bifurcated solution. The bifurcation point is determined using MATLAB. Equation (6.18) is solved by means of function *fzero*, which searches iteratively the solution starting from an initial value of $\lambda_{2,\infty}$. For each iteration, before computing Eq. (6.18), the corresponding value λ_3

must determined solving $G(1, \lambda_{2,\infty}, \lambda_3) = 0$ with function *fsolve* and the derivatives of W with respect to the stretches must be computed.

In the case of an incompressible material, substituting Eq. (2.8) in Eq. (6.17), the pressure curve relative to uniform inflation is written as

$$\bar{p} = \frac{2\left(\lambda_{2,\infty}^4 - 1\right)\left(w_1^{(\infty)} + w_2^{(\infty)}\right)}{\lambda_{2,\infty}^4}, \tag{6.20}$$

where $w_1^{(\infty)}$ and $w_2^{(\infty)}$ are the derivatives of W with respect to I_1 and I_2 evaluated at $\lambda_1 = 1$ and $\lambda_2 = \lambda_{2,\infty} = r_\infty / L$.

The bifurcation condition maintains the formal expression of Eq. (6.18). Since the transversal stretch λ_3 is given in explicit form by the relation $1/(\lambda_1\lambda_2)$, the computation of $\partial^2 W/\partial\lambda_1^2$, $\partial W/\partial\lambda_2$, $\partial^2 W/\partial\lambda_2^2$ and $\partial^2 W/\partial\lambda_1\partial\lambda_2$ is straightforward.

6.2.3 Inflation of spherical balloons

The third problem analysed is the inflation of a thin-walled spherical balloon of initial radius L and thickness H, illustrated in Fig. 6.3(c). We assume that during the inflation the balloon retains its spherical shape. Due to the symmetry of the problem, each point is subjected to equibiaxial extension. The deformation is homogeneous and the principal stretches read

$$\lambda_1 = \lambda_2 = \lambda = \frac{r}{L}, \quad \lambda_3 = \frac{h}{H}, \tag{6.21}$$

where r and h are respectively the deformed radius and thickness. The equilibrium equations are given by Eqs. (2.11) and (2.12). For a spherical balloon, Eq. (2.11) is trivially satisfied by simmetry, while Eq. (2.12) reduces to [136]

$$\sigma = \frac{pr}{2h}, \tag{6.22}$$

where σ is the principal Cauchy stress acting in the deformed plane. Recalling that the Cauchy stress reads $\sigma = (\partial W/\partial\lambda)(\lambda\lambda_3)^{-1}$, and using Eq. (6.21) into Eq. (6.22), the relation for the normalized pressure $\bar{p} = pL/H$ is obtained

$$\bar{p} = \frac{2}{\lambda^2}\frac{\partial W}{\partial \lambda}, \tag{6.23}$$

which, in terms of derivatives with respect to the strain invariants, reads

$$\bar{p} = \frac{4}{\lambda}\left[w_1 + \left(\lambda^2 + \lambda_3^2\right) w_2 + \lambda^2\lambda_3^2 w_3\right]. \tag{6.24}$$

The membrane assumption, defined by Eq. (6.3), reduces to

$$w_1 + 2\lambda^2 w_2 + \lambda^4 w_3 = 0. \tag{6.25}$$

This equation determines the transversal stretch λ_3 for a fix value of λ. In particular, a list of values for λ ranging from 1 to $\lambda_{0,max}$ is defined and Eq.(6.25) is

numerically solved using function *fsolve* in MATLAB. The numerical values of λ_3 are then substituted into Eq. (6.24) to compute the corresponding value of pressure. In the case of incompressible materials, the transversal stretch is given by $\lambda_3 = 1/\lambda^2$. The equilibrium equation reduces to the explicit relation

$$\bar{p} = 4\left(\lambda^{-1} - \lambda^{-7}\right)\left(w_1 + \lambda^2 w_2\right). \tag{6.26}$$

For increasing values of λ, the uniform spherical solution can bifurcate into an asymmetrical pear-shaped configuration. However, as shown by Haughton and Ogden [137], bifurcation can only occur after the maximum pressure is reached and the instability is triggered. For this reason, the study of bifurcation in spherical balloons is considered of little interest and is neglected.

6.3 Results and discussion

In this section, the results of incompressible and compressible models are compared for the four types of materials and the three problems considered: inflation of circular membranes, inflation of thin-walled cylindrical tubes and inflation of spherical balloons. The constitutive parameters for both compressible and incompressible models were calibrated from simple tension tests following the procedures outlined in Section 6.1.2. Since incompressible and compressible models provide the same responses in terms of stress vs. stretch in simple tension (see Fig. 6.2), it is reasonable to attribute eventual discrepancies in the following results to the effect of compressibility.

6.3.1 Circular flat membranes

The numerical solution for flat circular membranes under inflation is derived following the procedures outlined in Section 6.2.1. The results in terms of pressure vs. deflection curve, deformed shape and pressure vs. volume curve are presented in Fig. 6.4 for elastomers (types I and II), and Fig. 6.5 for material types III and IV. The second column of the above figures displays the deformed shapes related to the configuration at the maximum pressure $\bar{p}$ from the compressible model.

As expected, Fig. 6.4 shows an almost identical response between incompressible and compressible models for materials of type I. Indeed, volume deformations are small and the contribution of the volumetric strain energy is not relevant. However, materials of type II already show sensible discrepancies between incompressible and compressible solutions. On one hand, the pressure vs. deflection curve for EPDM exhibits a limit pressure followed by a softening branch. The effect of compressibility is focused in the region near the limit point, which is the region of most interest for practical applications. On the other hand, the pressure vs. deflection curve for NBR exhibits a monotonic trend, where the discrepancy between compressible and incompressible models slightly increases as the deformation increases.

A comparison in terms of deformed shapes provides further insigths into the effect of compressibility. In practical applications, membranes are generally inflated in pressure control, namely by applying an increasing internal pressure. The deformed

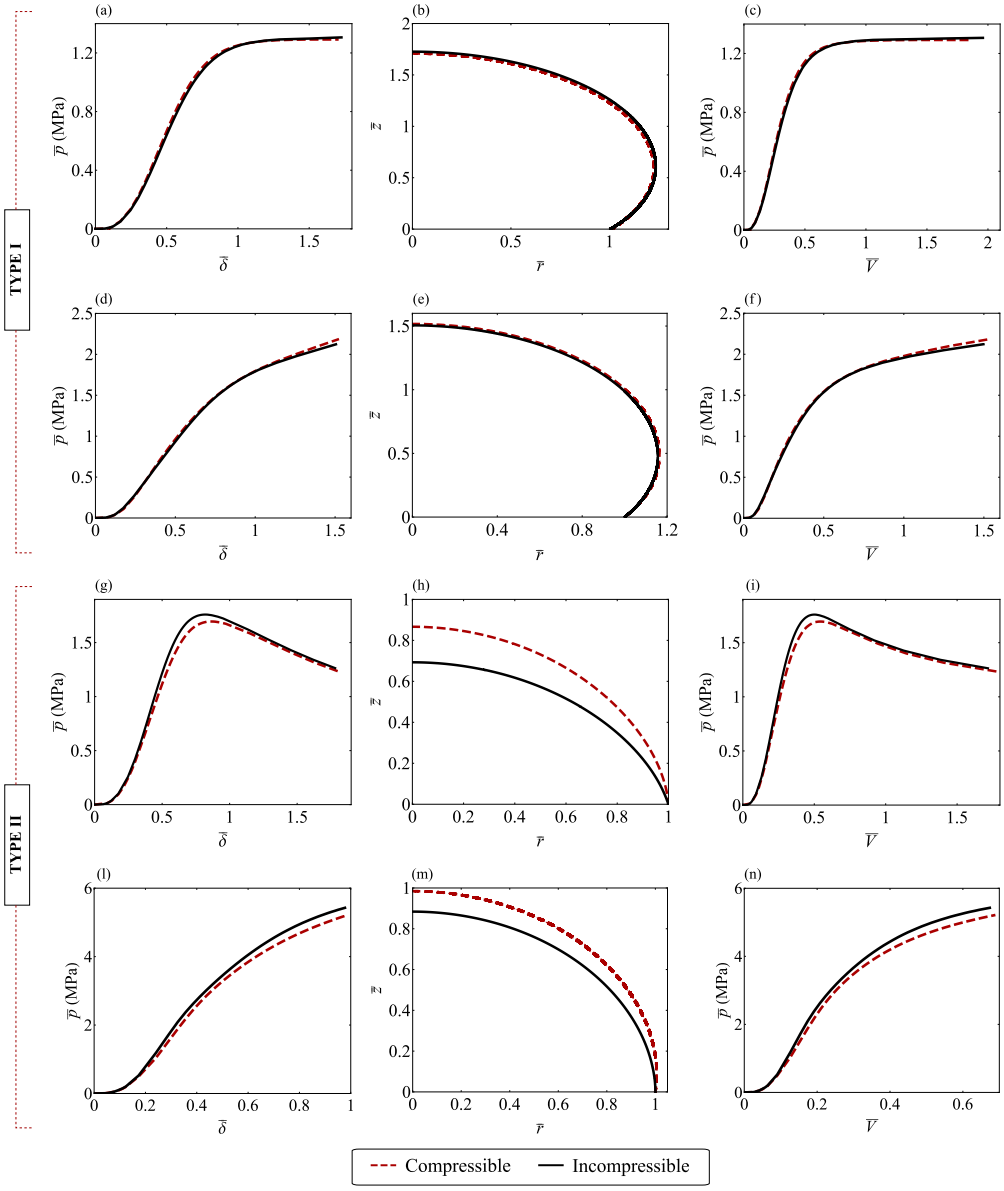

Figure 6.4: Inflation of a circular flat membrane. The results are shown for (a)-(c) NR, (d)-(f) silicone, (g)-(i) EPDM, (l)-(n) NBR, in terms of normalized pressure $\bar{p} = pL/H$ vs. deflection $\bar{\delta} = \delta/L$ curve, normalized deformed shapes ($\bar{r} = r/L$, $\bar{z} = z/L$) and normalized pressure $\bar{p} = pL/H$ vs. volume $\bar{V} = V/(\pi L^3)$ curve. For each material, the deformed shape corresponds to the value of maximum pressure on the compressible curves.

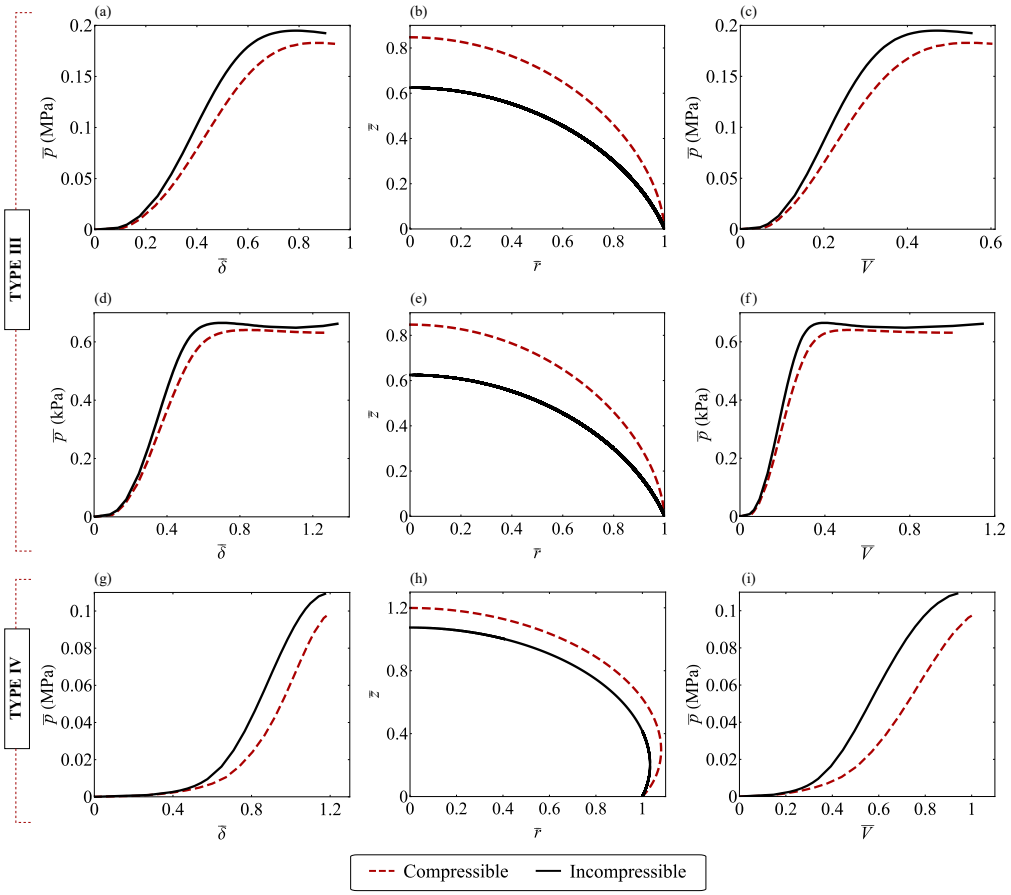

Figure 6.5: Inflation of a circular flat membrane. The results are shown for (a)-(c) foam, (d)-(f) hydrogel, (g)-(i) auxetic foam, in terms of normalized pressure $\bar{p} = pL/H$ vs. deflection $\bar{\delta} = \delta/L$ curve, normalized deformed shapes ($\bar{r} = r/L$, $\bar{z} = z/L$) and normalized pressure $\bar{p} = pL/H$ vs. volume $\bar{V} = V/(\pi L^3)$ curve. For each material, the deformed shape corresponds to the value of maximum pressure on the compressible curves.

shape corresponding to a given value of pressure can be of much interest, for instance in problems of contact mechanics. In particular, Figs. 6.4(h) and 6.4(m) display the deformed shapes for EPDM and NBR corresponding to the value of maximum pressure of the compressible model. Despite the limited error in terms of pressure, a significant discrepancy in the deformed shape occurs when a wrong assumption on the compressibility of the material is made. This result means that significant errors in the prediction of the deformed shapes can be expected when modeling type II materials with the assumption of incompressibility, especially at large deformations.

In other cases, the inflation may be performed in volume control. Hence, the third column of Figs. 6.4 and 6.5 shows the pressure vs. volume curves. It is evident a direct correspondence between the pressure vs. volume curves and the pressure vs. deflection curves for all the materials considered. Figures 6.4(i) and 6.4(n) show that for a given volume the error in pressure between compressible and incompressible models is limited. Hence, in case of inflation in volume control, the assumption of incompressibility remains acceptable for type II materials.

Regarding materials of type III and IV, the predictions of the compressible model differ substantially from those of the incompressible one, as shown in Fig. 6.5. Since these materials exhibit a marked compressibility even in the range of small strains, both pressure vs. deflection and pressure vs. volume curves deviate at low values of $\bar{\delta}$ and $\bar{V}$. Relative differences up to 13% are observed in the maximum pressure and 44% in the deflection. Significant errors are committed in volume control as well. As expected, for these materials the assumption of incompressibility is unacceptable.

6.3.2 Infinite thin-walled cylindrical tubes

The pressure vs. deflection curves for infinite thin-walled cylindrical tubes are computed by solving Eq. (6.17) and Eq.(6.20) respectively for compressible and incompressible models. Figure 6.6 shows the result for each material considered. Since the results refer to the uniform solution, the deformed shape of the tube is simply a homogeneous lateral expansion, described by parameter $\lambda_{2,\infty}$. Hence, the only difference between incompressible and compressible models is in the inflating pressure.

In case of materials of type I, slight discrepancies between the compressible and incompressible models appear only for large deformations, when the materials start to show small volume changes (see Fig. 6.1(d)). For materials of type II the impact of compressibility increases and no neglegible discrepancies between compressible and incompressible models are found. Again, in case of EPDM the error is located near the limit pressure, whereas for NBR it remains constant with the increase of deformation.

For materials of type III and IV compressibility significantly affects the pressure curve and errors occur also for moderate deformations. Again, when the material exhibits a limit pressure point, the error between compressible and incompressible models concentrates in that area.

As the inflation increases, the tube reaches a critical stretch $\lambda_{2,c}$ that triggers the bifurcated state and the appearance of a bulge. This point is crucial for practical applications and is determined by Eq. (6.18). Fu et al. [133] showed for incompress-

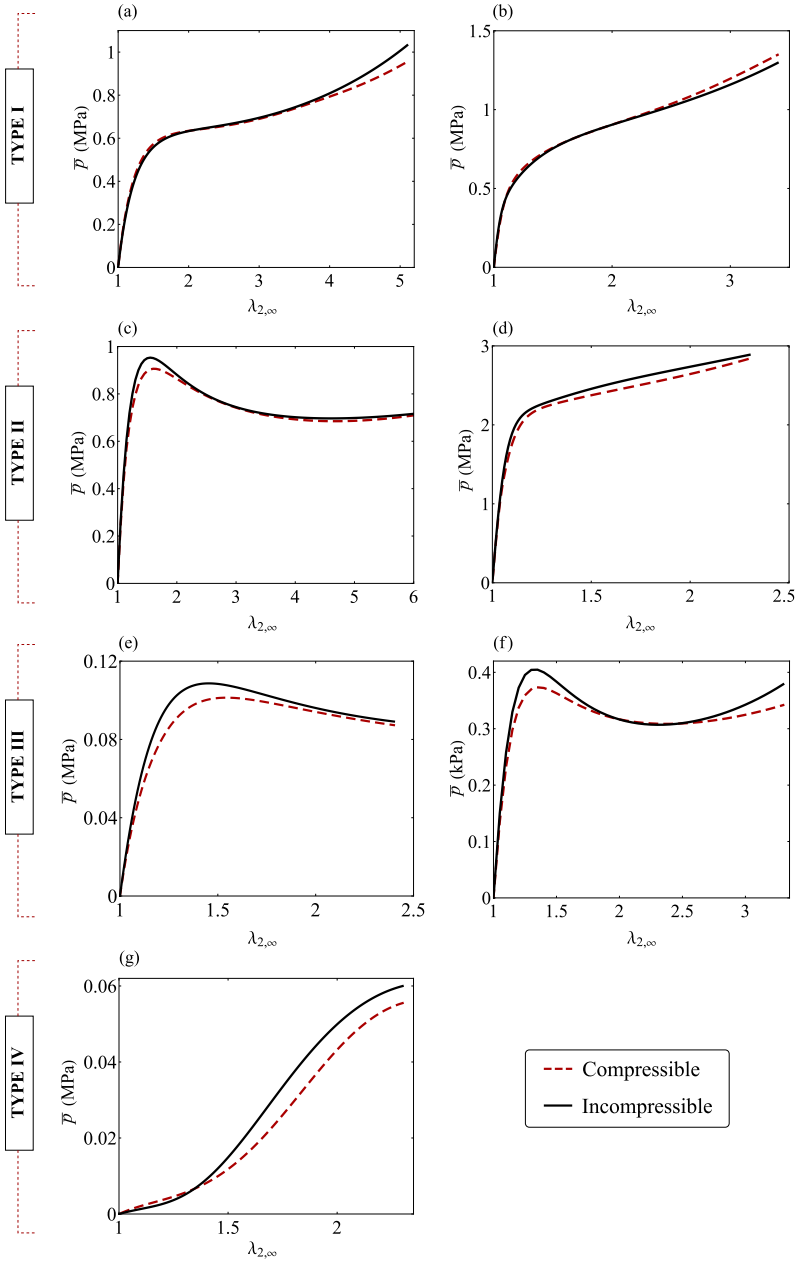

Figure 6.6: Uniform inflation of an infinite thin-walled cylindrical tube. The results are shown for (a) NR, (b) silicone, (c) EPDM, (d) NBR, (e) foam, (f) hydrogel and (g) auxetic foam. The curves are represented in terms of normalized pressure $\bar{p} = pL/H$ vs. uniform stretch $\lambda_{2,\infty} = r_\infty/L$.

Table 6.1: Inflation of thin-walled cylindrical tubes: critical stretch at bifurcation $\lambda_{2,c}$ and stretch corresponding to limit pressure $\lambda_{2,p_{max}}$. When $\lambda_{2,c}$ is reached, the uniform solution shifts to the bifurcated state.

		Type I		Type II		Type III		Type IV
		NR	Silicone	EPDM	NBR	Foam	Hydrogel	Auxetic foam
Compressible	$\lambda_{2,c}$	1.60	1.68	1.48	1.45	1.46	1.33	2.33
	$\lambda_{2,p_{max}}$	/	/	1.61	/	1.54	1.36	2.41
Incompressible	$\lambda_{2,c}$	1.63	1.70	1.45	1.52	1.39	1.30	2.15
	$\lambda_{2,p_{max}}$	/	/	1.55	/	1.45	1.32	2.45

ible materials that, if $(\partial^2 W/\partial\lambda_1^2)^{(\infty)} > 0$, bifurcation can take place only when the inflating pressure is increasing. Since the sign of $(\partial^2 W/\partial\lambda_1^2)^{(\infty)}$ does not depend on the volumetric part of the SED, this result holds also for compressible materials. Therefore, the study of the onset of bifurcation is of interest, since it always takes place before the limit pressure is attained. The stretch that triggers bifurcation is defined as critical stretch, and its values computed by Eq. (6.18) are reported in in Tab. 6.1 for compressible and incompressible models and for all the materials considered. Table 6.1 shows also the stretches corresponding to the limit pressure. Note that when the material exhibits a limit pressure (EPDM, foam, gel and auxetic foam), the critical stretch of the compressible model is always greater than the critical stretch of the incompressible model. On the contrary, when the material response is monotonic, the opposite happens. Ultimately, between compressible and incompressible models the bifurcation points only show slight quantitative variations without significant qualitative differences.

6.3.3 Thin-walled spherical balloons

The results of the inflation of a spherical balloon are obtained by solving Eqs. (6.24) and (6.26) for compressible and incompressible models respectively, and are displayed in Fig. 6.7. Among the three problems considered, it can be noticed that the spherical balloon exhibits the greatest discrepancies between the incompressible and compressible models. This is particularly evident for materials of type III and IV, for which the compressibility is more pronounced. Differences up to 18% in the maximum value of internal pressure are observed (see Fig. 6.7(f)).

An interpretation to the above results can be provided by considering the different strain and stress states in each problem. In the inflation of a spherical balloon, the principal stretches λ_1 and λ_2 are equal to each other and the body is under equibiaxial tension. Among the three problems considered, this stress state differs the most from the one in simple tension, where the parameters of both compressible and incompressible models were calibrated to obtain the same response. Thus, in this problem compressible and incompressible models show the greatest differences. On the other hand, in the uniform inflation of a cylindrical tube, λ_2 increases whereas λ_1 remains always equal to 1. The principal stress T_1 is much smaller than T_2 and this condition is relatively similar to the stress state in simple tension. For

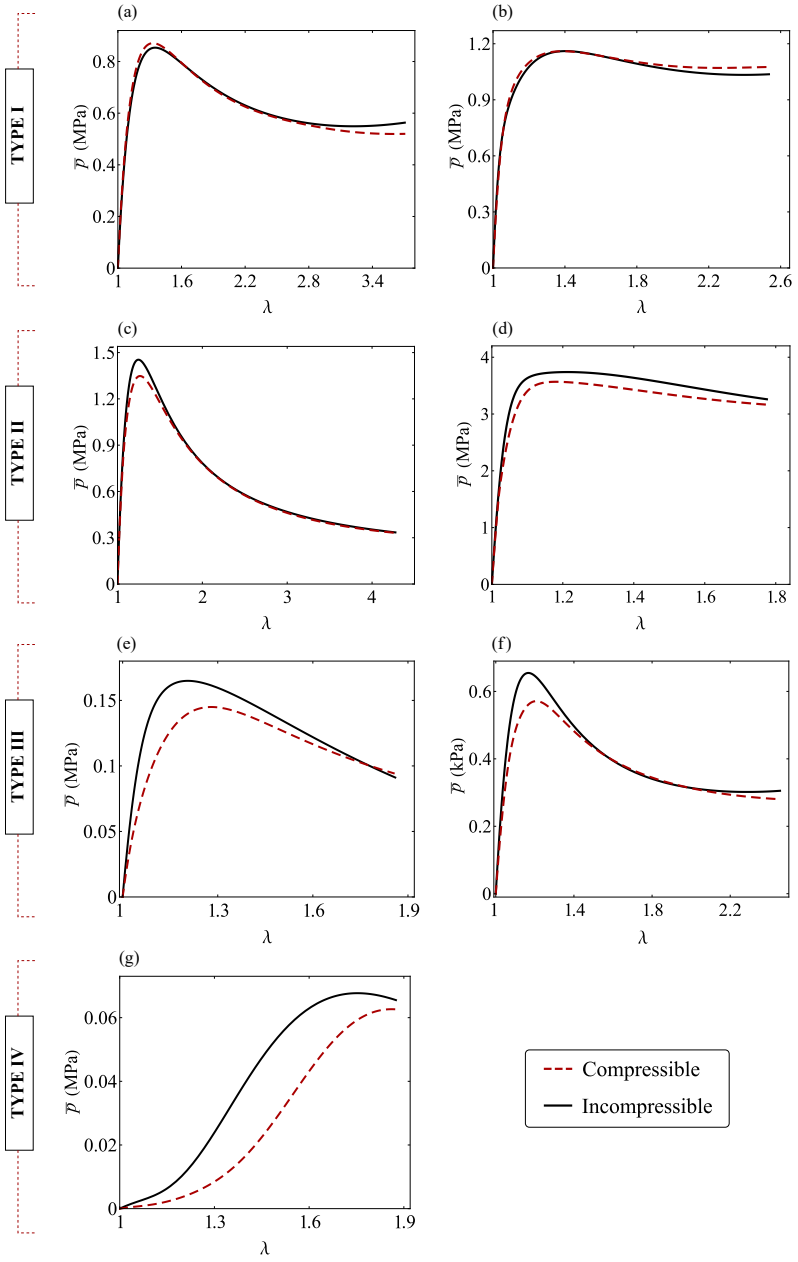

Figure 6.7: Inflation of a thin-walled spherical balloon. The results are shown for (a) NR, (b) silicone, (c) EPDM, (d) NBR, (e) foam, (f) hydrogel and (g) auxetic foam. The curves are represented in terms of normalized pressure $\bar{p} = pL/H$ vs. stretch $\lambda = r/L$.

this reason, since their parameters were calibrated to obtain the same uniaxial response, the compressible and incompressible solutions are more similar compared to the case of inflated balloons. Finally, the inflation of a circular flat membrane is an intermediate case. At the pole the stress state is equibiaxial with $\lambda_1 = \lambda_2$ and $T_1 = T_2$, but at the outer boundary $\lambda_2 = 1$ and the stress state is closer to the one in simple tension. Accordingly, the differences between compressible and incompressible models appear greater than those of the cylindrical tube, but lower than those of the spherical balloon.

6.4 Further considerations

In light of the results shown above, some further considerations on the effect of compressibility in inflated membranes can be drawn. As a general observation, a common trend of maximum discrepancy between compressible and incompressible models is observed around the limit point region. To provide an insight into this behavior, it is convenient to consider the inflation of a spherical balloon, where the principal stretches λ_1 and λ_2 are equal at every point, resulting in an equibiaxial stress state. Figure 6.8 shows the pressure vs. stretch, nominal stress vs. stretch and relative discrepancy between compressible and incompressible models in the pressure and stress curves of EPDM and NBR. As indicated by Figs. 6.8(c) and 6.8(f), the discrepancies between the two models in the pressure and stress curves are identical. In fact, considering Eq. (6.22) with $\sigma = s/(\lambda\lambda_3)$, $h = \lambda_3 H$ and $r = \lambda L$, the relation between the nominal stress and the pressure is

$$s = \frac{\lambda^2 L}{2H} p, \tag{6.27}$$

namely the pressure and the nominal stress are proportional by a factor independent of compressibility. The limit point region in the pressure curves aligns with the transition region between linear and nonlinear behavior in the stress vs. stretch curves. This specific region exhibits the major discrepancy between stress computed from compressible and incompressible models, thereby leading to a more pronounced discrepancy in the pressure curves. The marked discrepancy in nominal stress between compressible and incompressible models observed in this region can be explained by the high rate of change in stiffness specific to this area.

The inflation of cylindrical tubes and the inflation of circular membranes are increasingly complex problems. In particular, in the latter case the stresses vary at each point radially along the membrane. Discrepancies in the nominal stress between compressible and incompressible models are still primarily responsible for discrepancies in the pressure curves, but further phenomena like limit point instability now play an important role in the membrane response. Figure 6.9 compares the response of EPDM and NBR rubbers in the case of a circular membrane, showing the deformed shapes and the volume change along the radius for increasing values of deformation. In the case of EPDM, the pressure curve exhibits a limit point, where the discrepancy between compressible and incompressible models is maximum, followed by a softening branch, where the two models converge to the same curve. The

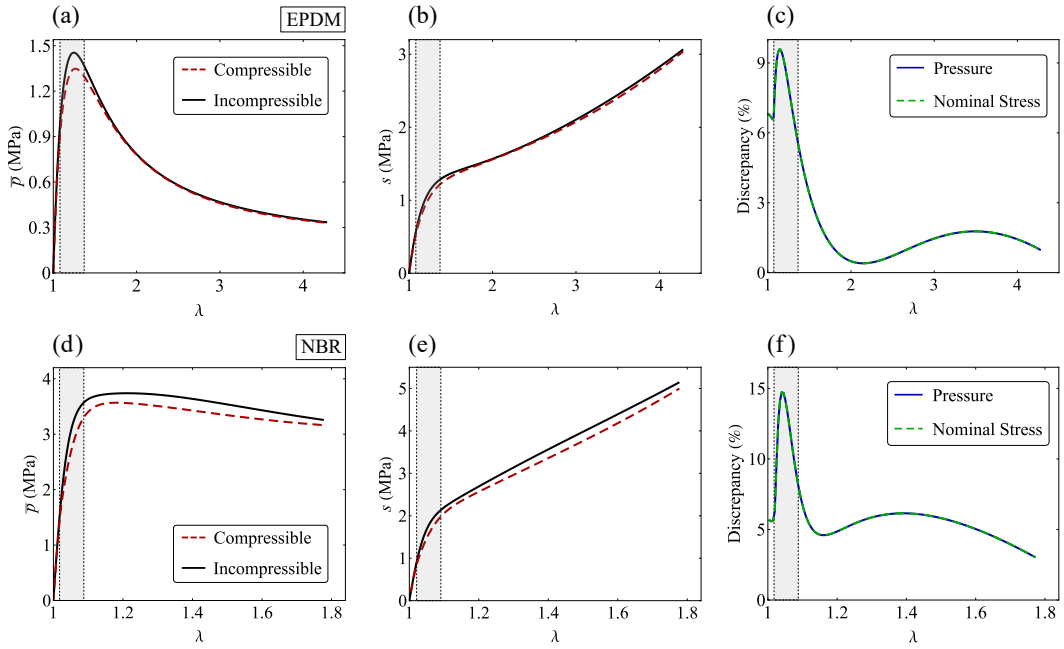

Figure 6.8: Comparison between EPDM and NBR inflated spherical balloons. Figs. (a), (b) and (c) respectively show pressure vs. stretch, nominal stress vs. stretch and relative discrepancy in pressure and stress curves between compressible and incompressible models for EPDM. Figs. (d), (e) and (f) depict the corresponding curves for NBR. For a spherical balloon, the stress state is equibiaxial and therefore the discrepancy in pressure curves and nominal stress curves coincides. Major discrepancies are observed near the limit point region in the pressure vs. stretch curves, which corresponds to the transition region between linear and nonlinear behavior in the stress vs. stretch curves.

limit point triggers an instability characterized by a lateral expansion, as indicated in Fig. 6.9(b). Figure 6.9(c) shows how, after the limit point, the change in volume starts to decrease at the outer boundary. Therefore, as the deformation increases, in the outer region compressibility has less effect since the change in volume reduces. On the contrary, in the case of NBR the limit point is not reached. The pressure is monotonic and the volume change continues to increase in the entire domain of the membrane (see Fig. 6.9(f)). Accordingly, the relative discrepancy between compressible and incompressible models slightly increases as the deformation increases. In conclusion, when limit point instability occurs, the effect of compressibility tends to reduce along the unstable softening branch.

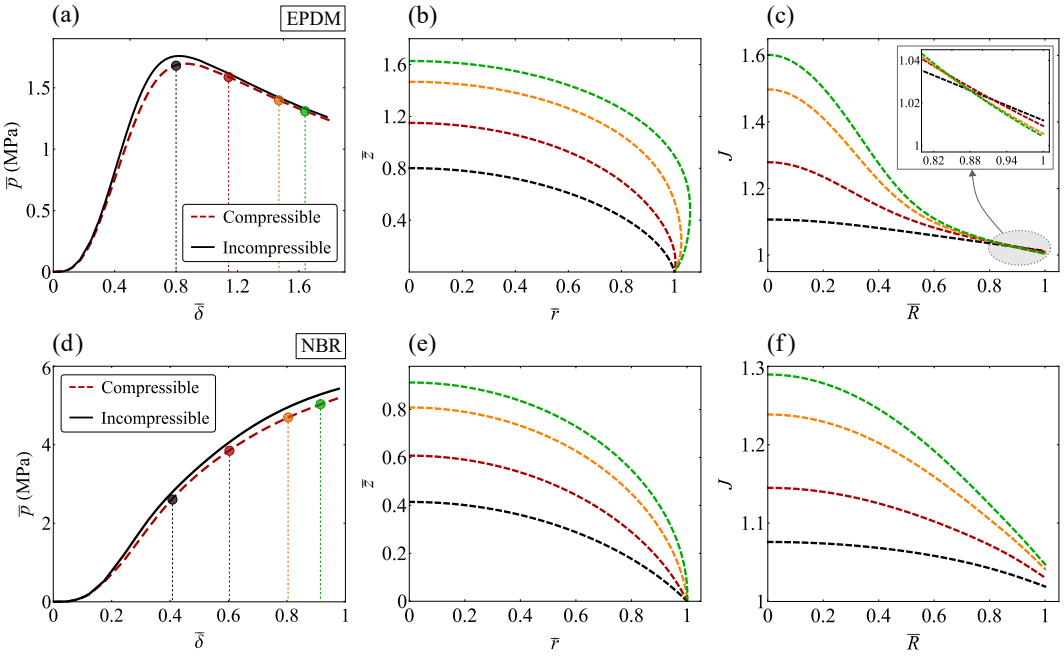

Figure 6.9: Comparison between EPDM and NBR inflated circular membranes. Figs. (a), (b) and (c) respectively show pressure vs. deflection curves, deformed shapes and volume changes in the domain for EPDM, while Figs. (d), (e) and (f) depict the corresponding curves for NBR. In the case of EPDM, the $\bar{p}$ vs. $\bar{\delta}$ curve exhibits a limit point that triggers an unstable softening branch. Correspondingly, the deformed shape shows lateral expansion, and the volume change starts to decrease at the outer boundary of the domain. In the case of NBR, the $\bar{p}$ vs. $\bar{\delta}$ curve is monotonic, and the change in volume increases with deformation throughout the domain.

7 Conclusions

This thesis presented a comprehensive investigation of the mechanics of inflatable elastic membranes. Mechanical problems of elastic membranes are characterized by high geometrical and material nonlinearities, leading to a mathematical complexity which requires the use of numerical approaches. The development of analytical solutions and refined mathematical models for the response of rubber-like and soft materials are the main developments of this thesis.

In Chapter 3 an analytical solution for the inflation of circular membranes described by a Mooney-Rivlin material was proposed. The proposed solution derives from the combination of a simplified analytical model adjusted by a refining fitting procedure to the exact numerical solution of the problem. The simplified model captures the essential features of the phenomenon, whereas the fitting process extends the accuracy and validity of the proposed solution to large deformations and wide range of material parameters of practical interest. The final analytical formula to compute the pressure vs. deflection curves represents a practical tool for designing and predicting the performance of inflated circular membranes. The proposed solution was then extended to compressible Mooney-Rivlin materials. In Chapter 4 the case of circular membranes with an initial pre-stretch was considered, and a second parametrical fitting to the numerical solution was performed in order to extend the analytical formula to the case of pre-stretched membranes. Experimental bulge tests were conducted on membranes in both unstretched and prestretched conditions. The proposed solution was employed for the calibration of material parameters based on the bulge tests, proving its efficacy as a tool for material characterization under biaxial stress states.

At large deformations, the Mooney-Rivlin model encounters limitations in accurately depicting volumetric deformations and the hardening behavior typical of elastomers. For this reason, subsequently the thesis focused on the calibration of an accurate strain energy function for large deformations of rubber-like materials. Experimental investigations, encompassing both simple tension and bulk tests, revealed how some class of elastomers can experience significant volume changes when large deformations are involved. From these experimental data the complete volumetric curve in shrinkage and expansion was derived. Following the split of the strain energy function into its volumetric and deviatoric parts, an original volumetric SED was proposed in Chapter 5. Contrary to the existing volumetric formulations, the proposed SED offers the following main advantages:

- Being tailored for elastomers, the proposed SED is capable of predicting accurately the volumetric response of these materials at large deformations;
- It respects all the criteria of physical plausibility and it offers a total independent control of shrinkage and expansion.

- The formulation allows defining not only different parameters for shrinkage and expansion, but also different response functions. In this way, different response functions can be used when dealing with different materials.

Successively, the Yeoh-Fleming model was chosen as the most effective formulation and selected as deviatoric part of the SED. A final fitting of the combined SED on the experimental data determined the model parameters and proved the effectiveness of the proposed formulation in describing both shape and volume deformations of elastomers.

Finally, in Chapter 6 the proposed SED was used to study the effect of compressibility on the mechanics of inflatable membranes. In addition to the elastomers analysed in Chapter 5, the response of soft materials like polymeric foam, gel and auxetic foam was studied. These materials are compressible even in the range of small strains and are encountering increasing applications in modern technologies. The solutions of three benchmark problems of inflatable membranes were extended to compressible materials and significant effects of compressibility were observed in the limit pressure and deformed shapes.

In light of these developments, the emerging future prospects are the following:

- The response of membranes made of compressible materials was based on material parameters calibrated on uniaxial tests. Experimental bulge tests on circular membranes and cylindrical tubes made of compressible materials can be carried out in the future, in order to characterize the materials under a biaxial stress state and to obtain information on the actual deformed shapes and changes in volume.

- The problems analysed and the responses observed in this thesis can serve as foundation for the study of more complex systems and practical applications where compressibility can open new developments. For instance, in problems of contact mechanics the deformed shape assumed by the membrane is of great interest and it may be significantly affected by material compressibility.

A Equilibrium solutions for simple tension and bulk test in nonlinear elasticity

In this appendix, the solutions to the equilibrium problems in simple tension and bulk test are derived.

A.1 Simple tension

Consider a homogeneous, isotropic and hyperelastic solid described by a stored energy function $W(I_1, I_2, I_3)$. Define a Cartesian reference system x, y, z, where x is the longitudinal axis of the sample. In simple tension, uniaxial tractions are uniformly distributed on the basis of the solid and act in the x direction. In this case, the two lateral principal stresses are identically zero ($s_y = s_z = 0$). As a consequence of isotropy, the lateral stretches are equal to each other ($\lambda_y = \lambda_z$).

The equilibrium solution for a compressible hyperelastic solid under simple tension is given by [138]

$$\frac{\partial W}{\partial I_1} + \left(\lambda_x^2 + \lambda_y^2\right) \frac{\partial W}{\partial I_2} + \lambda_x^2 \lambda_y^2 \frac{\partial W}{\partial I_3} = 0, \tag{A.1}$$

$$s_x = 2\lambda_x \left(\frac{\partial W}{\partial I_1} + 2\lambda_y^2 \frac{\partial W}{\partial I_2} + \lambda_y^4 \frac{\partial W}{\partial I_3} \right). \tag{A.2}$$

From the first implicit equation, the lateral stretch λ_y can be determined for a given longitudinal stretch λ_x. The nominal stress s_x is computed from the second equation and the true stress can be derived as $\sigma_x = s_x/\lambda_y^2$.

For an incompressible material, the condition $J = 1$ gives the following relation between lateral and longitudinal stretches: $\lambda_y = 1/\sqrt{\lambda_x}$. The equilibrium solution reads

$$s_x = 2\left(1 - \frac{1}{\lambda_x^3}\right)\left(\lambda_x \frac{\partial W}{\partial I_1} + \frac{\partial W}{\partial I_2}\right). \tag{A.3}$$

In case of strain energy written as a function of the principal stretches, $W = \tilde{W}(\lambda_1, \lambda_2, \lambda_3)$, the nominal stresses for an incompressible material are computed as $s_i = \partial \tilde{W}/\partial \lambda_i - p\lambda_i^{-1}$, with $i = 1, 2, 3$.
In simple tension we have that $\tilde{W}(\lambda_x, 1/\sqrt{\lambda_x}, 1/\sqrt{\lambda_x}) = \hat{W}(\lambda_x)$ and the equilibrium reduces to

$$s_x = \frac{\partial \hat{W}}{\partial \lambda_x}. \tag{A.4}$$

A.2 Bulk test

For the case of the bulk test, the lateral deformations are constrained, and thus $\lambda_y = \lambda_z = 1$ and $\lambda_x = J$. The equilibrium equations in the longitudinal and lateral directions read respectively:

$$s_x = \sigma_x = 2J\left(\frac{\partial W}{\partial I_1} + 2\frac{\partial W}{\partial I_2} + \frac{\partial W}{\partial I_3}\right), \tag{A.5}$$

$$s_y = 2\frac{\partial W}{\partial I_1} + 2\left(1 + J^2\right)\frac{\partial W}{\partial I_2} + 2J^2\frac{\partial W}{\partial I_3}. \tag{A.6}$$

Making explicit the deviatoric and volumetric parts of the energy function, $W = W_d(\bar{I}_1, \bar{I}_2) + W_h(J)$, Eq. (A.5) is written as follows

$$\sigma_x = 2J\left(\frac{\partial W_d}{\partial I_1} + 2\frac{\partial W_d}{\partial I_2} + \frac{\partial W_d}{\partial I_3}\right) + \frac{\partial W_h}{\partial J}. \tag{A.7}$$

The first and second addends are respectively the deviatoric and volumetric contributions to the stress σ_x in the bulk test. In the following, it is shown that for rubber-like materials the deviatoric contribution, named σ_d for convenience, can be neglected.

Recalling the definition of the deviatoric strain invariants given in Eq. (5.3) and using the chain rule to compute the derivatives, the first addend of Eq. (A.7) becomes

$$\sigma_d = \frac{4}{3}\left(\frac{\partial W_d}{\partial \bar{I}_1}J^{2/3} + \frac{\partial W_d}{\partial \bar{I}_2}\right)\left(J^2 - 1\right)J^{-7/3}. \tag{A.8}$$

Convexity of the stored energy function requires that $\partial W_d/\partial \bar{I}_1 > 0$ and $\partial W_d/\partial \bar{I}_2 > 0$ [139]. Therefore, since in the bulk test $J \leq 1$, we have that

$$|\sigma_d| \leq \left|\frac{4}{3}\left(\frac{\partial W_d}{\partial \bar{I}_1} + \frac{\partial W_d}{\partial \bar{I}_2}\right)\left(J^2 - 1\right)J^{-7/3}\right|. \tag{A.9}$$

The solution in simple shear for incompressible materials [140] is $\sigma_{12} = \tilde{\mu}\gamma$, being γ the amount of shear, σ_{12} the Cauchy stress and $\tilde{\mu} = 2\left(\partial W_d/\partial \bar{I}_1 + \partial W_d/\partial \bar{I}_2\right)$. The quantity $\tilde{\mu}$ tends to the infinitesimal shear modulus μ in the range of small strains and can be interpreted as a secant shear modulus in nonlinear elasticity. Equation (A.9) is rewritten as

$$|\sigma_d| \leq \frac{2\,(J+1)}{3J^{7/3}}\tilde{\mu}\,|(J-1)|\,. \tag{A.10}$$

Regarding the volumetric contribution $\sigma_h = \partial W_h/\partial J$, we introduce the secant bulk modulus $\tilde{\kappa}$ and write

$$|\sigma_h| = \tilde{\kappa}\,|(J-1)|\,. \tag{A.11}$$

The experiments presented in Section 5.1 and in previous literature (see, e.g., [71,95,96,141]) show that elastomers exhibit a hardening trend during volume shrinkage. Namely, the secant bulk modulus in shrinkage is initially equal to κ and then increases as J decreases. From Eqs. (A.10) and (A.11) we conclude the following:

$$\frac{t_d}{t_h} \leq \frac{2\,(J+1)}{3J^{7/3}}\frac{\tilde{\mu}}{\tilde{\kappa}}. \tag{A.12}$$

The multiplying factor $2(J+1)/(3J^{7/3})$ increases as J decreases. However, in the bulk test, the J values of interest for rubbers are between 0.8 and 1. This range covers widely the values of pressure applied in real applications. When $J < 0.8$ the applied pressure becomes extremely large and, from a practical point of view, this is of no interest With that said, the value of the multiplying factor for $J = 0.8$ is very close to 2. Hence, in the range $J \in [0.8, 1]$ it results

$$\frac{\sigma_d}{\sigma_h} \leq \frac{2\tilde{\mu}}{\tilde{\kappa}}. \tag{A.13}$$

For rubber-like materials $\tilde{\mu} << \tilde{\kappa}$ and therefore the deviatoric contribution σ_d to the stress σ_x in the bulk test can be neglected. Hence, from Eq. (A.7) we obtain

$$s_x = \sigma_x \approx \frac{\partial W_h}{\partial J}. \tag{A.14}$$

It is worth mentioning that Horgan and Murphy [142] obtained the same result, but considering nearly incompressible elastomers. They reported that for infinitesimal volume changes σ_d is approximated by the linearization $\beta\,(J-1)$, where β is a constant of the order of μ. Since $\partial W_h/\partial J$ is approximated by $\kappa\,(J-1)$ and $\mu << \kappa$, the deviatoric contribution can be neglected and Eq. (A.14) is obtained. This result is extended here to the case of large volumetric deformations.

B Tables of fitted parameters

Tables B.1, B.2, B.3, B.4 and B.5 respectively list the parameters obtained from the fitting described in Sections 5.2.2, 5.3, 5.4, 5.5.2 and 6.1.2.

Table B.1: Parameters obtained by fitting the current volumetric SED formulations to the experimental data in Fig. 5.7. If applicable, the units are in MPa.

Formulation	EPDM		NBR	
	$J < 1$	$J \geq 1$	$J < 1$	$J \geq 1$
Doll [101]	$\alpha = 0.01$ $\beta = 25.25$	$\alpha = 3.46$ $\beta = 517.12$	$\alpha = 0.01$ $\beta = 35.58$	$\alpha = 5.67$ $\beta = 395.96$
Montella [105]	$\kappa_2 = 160750$ $\beta_1 = 0.125$ $\beta_2 = 0.125$ $m = 4$	$\kappa_2 = 6.02$ $\beta_1 = 0.125$ $\beta_2 = 5.01$ $m = 22.44$	$\kappa_2 = 302305$ $\beta_1 = 0.125$ $\beta_2 = 0.125$ $m = 4$	$\kappa_2 = 11.8$ $\beta_1 = 0.125$ $\beta_2 = 4.17$ $m = 14.15$
Moerman [88]	$J_2 = 0.881$ $s_2 = 0.194$ $q_2 = 0$	$J_1 = 2.85$ $s_1 = 0.585$ $q_1 = 0.987$	$J_2 = 0.902$ $s_2 = 0.095$ $q_2 = 0$	$J_1 = 9.982$ $s_1 = 0.721$ $q_1 = 0.972$
	NR		Silicone	
	$J < 1$	$J \geq 1$	$J < 1$	$J \geq 1$
Doll [101]	$\alpha = 0.01$ $\beta = 18.86$	$\alpha = 9.91$ $\beta = 172.44$	$\alpha = 0.01$ $\beta = 9.97$	$\alpha = 12.77$ $\beta = 331.77$
Montella [105]	$\kappa_2 = 113343$ $\beta_1 = 0.125$ $\beta_2 = 0.125$ $m = 4$	$\kappa_2 = 17.93$ $\beta_1 = 0.125$ $\beta_2 = 7.34$ $m = 10.61$	$\kappa_2 = 31223$ $\beta_1 = 0.125$ $\beta_2 = 0.125$ $m = 4$	$\kappa_2 = 15.18$ $\beta_1 = 0.125$ $\beta_2 = 7.53$ $m = 9.95$
Moerman [88]	$J_2 = 0.869$ $s_2 = 0.098$ $q_2 = 0$	$J_1 = 9.99$ $s_1 = 2.69$ $q_1 = 0.891$	$J_2 = 0.816$ $s_2 = 0.1$ $q_2 = 0$	$J_1 = 9.55$ $s_1 = 1.65$ $q_1 = 0.931$

Table B.2: Parameters obtained by fitting the proposed volumetric SED to the experimental data in Fig. 5.5.

Formulation	EPDM	NBR	NR	Silicone
Proposed SED, Eq. (5.16)	$\alpha_1 = 81.07$ $\alpha_2 = 5.1$ $\alpha_3 = 84.80$ $\beta_1 = 2.23$ $\beta_2 = 9.05$ $\beta_3 = 6.88 \times 10^{-4}$ $q = 0.974$	$\alpha_1 = 83.33$ $\alpha_2 = 8.03$ $\alpha_3 = 89.69$ $\beta_1 = 4.18$ $\beta_2 = 14.03$ $\beta_3 = 13.76 \times 10^{-4}$ $q = 0.953$	$\alpha_1 = 92.59$ $\alpha_2 = 4.99$ $\alpha_3 = 95.47$ $\beta_1 = 7.09$ $\beta_2 = 69.25$ $\beta_3 = 13.14 \times 10^{-4}$ $q = 0.723$	$\alpha_1 = 32.26$ $\alpha_2 = 4.51$ $\alpha_3 = 34.12$ $\beta_1 = 5.03$ $\beta_2 = 68.86$ $\beta_3 = 1 \times 10^{-4}$ $q = 0.461$

Table B.3: Parameters obtained by fitting the current deviatoric SED formulations to the experimental data in simple tension. If applicable, the units are in MPa.

Formulation	EPDM	NBR	NR	Silicone
Gent [60]	$\mu = 0.68$ $J_m = 198$	$\mu = 3.08$ $J_m = 145$	$\mu = 0.63$ $J_m = 61.64$	$\mu = 0.91$ $J_m = 32.52$
Gent-Gent [118]	$C_1 = 0.28$ $C_2 = 1.68$ $J_m = 202.3$	$C_1 = 0.55$ $C_2 = 5.43$ $J_m = 6.78$	$C_1 = 0.30$ $C_2 = 0.22$ $J_m = 57.61$	$C_1 = 0.44$ $C_2 = 0.16$ $J_m = 29.89$
Yeoh [59]	$C_{10} = 0.01$ $C_{20} = 0.09$ $C_{30} = -9.1 \times 10^{-6}$	$C_{10} = 0.01$ $C_{20} = 0.35$ $C_{30} = -1.76 \times 10^{-4}$	$C_{10} = 0.19$ $C_{20} = 0.033$ $C_{30} = 8.89 \times 10^{-5}$	$C_{10} = 0.29$ $C_{20} = 0.04$ $C_{30} = 4.34 \times 10^{-4}$
Carroll [119]	$A = 0.27$ $B = 2.84 \times 10^{-7}$ $C = 1.74$	$A = 0.12$ $B = 6.82 \times 10^{-4}$ $C = 7.85$	$A = 0.37$ $B = 2.10 \times 10^{-6}$ $C = -0.26$	$A = 0.52$ $B = 1.91 \times 10^{-5}$ $C = -0.28$
Ogden [58]	$\mu_1 = 2.62$ $\mu_2 = 0.26$ $\alpha_1 = 3.1 \times 10^{-3}$ $\alpha_2 = 2.99$	$\mu_1 = 0.017$ $\mu_2 = 8.49$ $\alpha_1 = 9.26$ $\alpha_2 = 0.011$	$\mu_1 = 1.4$ $\mu_2 = 0.02$ $\alpha_1 = 1.75$ $\alpha_2 = 4.94$	$\mu_1 = 0.6$ $\mu_2 = 1.49$ $\alpha_1 = 3.43$ $\alpha_2 = 1.1 \times 10^{-3}$
Yeoh-Fleming [61]	$A = 0.29$ $B = 7 \times 10^{-3}$ $C_{10} = 0.44$ $I_m = 1.49$	$A = 1.28$ $B = 2.16 \times 10^{-3}$ $C_{10} = 2.74$ $I_m = 2.94$	$A = 0.27$ $B = 0.078$ $C_{10} = 0.09$ $I_m = 0.02$	$A = 0.43$ $B = 1.72 \times 10^{-3}$ $C_{10} = 0.49$ $I_m = 2.96$

Table B.4: Parameters obtained by fitting the combined formulation to the experimental data. The deviatoric part W_d of the SED is expressed by the Yeoh-Fleming model [61], while the volumetric part W_h is defined by the proposed model, given in Eq. (5.16). The calibrated parameters of W_h are those reported in Tab. B.2 and are repeated here for the convenience of the reader. If applicable, the units are in MPa.

SED	EPDM	NBR	NR	Silicone
W_d	$A = 0.313$ $B = 0.03$ $C_{10} = 0.373$ $I_m = 1.3$	$A = 1.31$ $B = 7.82 \times 10^{-3}$ $C_{10} = 2.59$ $I_m = 2.93$	$A = 0.258$ $B = 0.074$ $C_{10} = 0.121$ $I_m = 0.628$	$A = 0.417$ $B = 4.32 \times 10^{-3}$ $C_{10} = 0.397$ $I_m = 2.92$
W_h	$\alpha_1 = 81.07$ $\alpha_2 = 5.1$ $\alpha_3 = 84.80$ $\beta_1 = 2.23$ $\beta_2 = 9.05$ $\beta_3 = 6.88 \times 10^{-4}$ $q = 0.974$	$\alpha_1 = 83.33$ $\alpha_2 = 8.03$ $\alpha_3 = 89.69$ $\beta_1 = 4.18$ $\beta_2 = 14.03$ $\beta_3 = 13.76 \times 10^{-4}$ $q = 0.953$	$\alpha_1 = 92.59$ $\alpha_2 = 4.99$ $\alpha_3 = 95.47$ $\beta_1 = 7.09$ $\beta_2 = 69.25$ $\beta_3 = 13.14 \times 10^{-4}$ $q = 0.723$	$\alpha_1 = 32.26$ $\alpha_2 = 4.51$ $\alpha_3 = 34.12$ $\beta_1 = 5.03$ $\beta_2 = 68.86$ $\beta_3 = 1 \times 10^{-4}$ $q = 0.461$

Table B.5: Optimal parameters for both incompressible and compressible models for materials of type III and IV. The fitting is performed on the stress vs. stretch data in simple tension. If applicable, the units are in kPa.

		Foam	Hydrogel	Auxetic Foam
Incompr.	A	33	0.089	-147
	B	0.001	0.0377	-1.026
	C_{10}	60	0.34	149
	I_m	2.13	2.48	1.32
Compr.	A	51.6	0.137	-258
	B	0.0101	0.0187	-1.088
	C_{10}	65	0.373	270
	I_m	2.50	2.714	2.45
	κ	595.6	2.7	1.9
	β_1	2.34	7.08	4.58
	β_2	31.7	17.22	2.18
	β_3	0.321	0.0764	0.0954
	q	0.327	0.751	0.65

C Mathematical requirements for the proposed volumetric SED

In this appendix, the validity criteria that the proposed volumetric SED must fulfill for its physical plausibility are derived. For the sake of clarity, recall that the proposed formulation is

$$W_h(J) = \kappa\left[H(1-J)\,\Psi_c + H(J-1)\,\Psi_t\right], \tag{C.1}$$

where H is the Heaviside step function defined in Eq. (5.17), and Ψ_c and Ψ_t are

$$\begin{aligned}\Psi_c(J) = \frac{1}{\alpha_1+\alpha_2-\alpha_3}\Bigg[&\left(J + \frac{J^{\alpha_1+1}}{\alpha_1+1} + \frac{J^{-(\alpha_2-1)}}{\alpha_2-1} - \frac{J^{\alpha_3+1}}{\alpha_3+1}\right)\\ &-\left(1 + \frac{1}{\alpha_1+1} + \frac{1}{\alpha_2-1} - \frac{1}{\alpha_3+1}\right)\Bigg],\end{aligned} \tag{C.2}$$

$$\Psi_t(J) = (1-q)\left[\frac{\beta_2 e^{\beta_1(J-1)} + \beta_1 e^{-\beta_2(J-1)}}{\beta_1\beta_2(\beta_1+\beta_2)} - \frac{1}{\beta_1\beta_2}\right] + q\beta_3^2 \ln\left(\cosh\left(\frac{J-1}{\beta_3}\right)\right). \tag{C.3}$$

The hydrostatic stress is computed as

$$\sigma_h(J) = \frac{dW_h(J)}{dJ} = \kappa\left[H(1-J)\,\psi_c + H(J-1)\,\psi_t\right] \tag{C.4}$$

where

$$\psi_c(J) = \frac{d\Psi_c(J)}{dJ} = \frac{1 + (J^{\alpha_1} - J^{-\alpha_2} - J^{\alpha_3})}{\alpha_1+\alpha_2-\alpha_3}, \tag{C.5}$$

$$\psi_t(J) = \frac{d\Psi_t(J)}{dJ} = (1-q)\frac{\left(e^{\beta_1(J-1)} - e^{-\beta_2(J-1)}\right)}{\beta_1+\beta_2} + q\beta_3 \tanh\left(\frac{J-1}{\beta_3}\right). \tag{C.6}$$

The tangent modulus is computed as the second derivative of the energy with respect to J, namely

$$\frac{d^2W_h(J)}{dJ^2} = \kappa\left[H(1-J)\frac{d\psi_c}{dJ} + H(J-1)\frac{d\psi_t}{dJ}\right]. \tag{C.7}$$

For volume shrinkage ($J<1$) the tangent modulus reduces to

$$\frac{d^2W_h(J)}{dJ^2} = \kappa\frac{d\psi_c}{dJ} = \kappa\frac{\left(\alpha_1 J^{\alpha_1-1} + \alpha_2 J^{-\alpha_2-1} - \alpha_3 J^{\alpha_3-1}\right)}{\alpha_1+\alpha_2-\alpha_3}, \tag{C.8}$$

whereas for volume expansion ($J>1$) its expression is

$$\frac{d^2W_h(J)}{dJ^2} = \kappa\frac{d\psi_t}{dJ} = \kappa\left[(1-q)\frac{\beta_1 e^{\beta_1(J-1)} + \beta_2 e^{-\beta_2(J-1)}}{\beta_1+\beta_2} + q\,\mathrm{sech}^2\left(\frac{J-1}{\beta_3}\right)\right]. \tag{C.9}$$

The ten criteria for physical plausibility are reported in Tab. 5.2. Criteria I and II impose that the energy and the stress must vanish in the reference state ($J = 1$). These conditions are satisfied because Eqs. (C.1) and (C.4) evaluated for $J = 1$ give $W_h(1) = 0$ and $\sigma_h(1) = 0$. Criterion III requires the energy to be positive in the entire J domain. Provided that $\min W_h(J) = W_h(1) = 0$, the above condition is ensured by verifying the convexity of $W_h(J)$, which will be discussed in the following (criterion IX). Criterion IV states that the tangent modulus d^2W_h/dJ^2 computed for $J = 1$ must be equal to the bulk modulus κ, for consistency with linear elasticity. Equation (C.7) evaluated in $J = 1$ satisfies this requirement.

Criteria V, VI, VII and VIII impose conditions on the behaviors of W_h and σ_h for $J \to 0$ and $J \to +\infty$. We remark that the Heaviside step function allows to decouple the responses in shrinkage and expansion. Therefore, it is sufficient to study the functions Ψ_c, ψ_c, Ψ_t and ψ_t to determine the behaviors of W_h and σ_h at the boundaries of the domain. To ensure that an infinite energy is required to reduce to zero the volume of a solid (criterion V), the following limit must be satisfied:

$$\lim_{J\to 0} \Psi_c(J) = +\infty, \tag{C.10}$$

with Ψ_c expressed by Eq. (C.2). This happens with the following conditions on α_1, α_2 and α_3:

$$\begin{cases} \alpha_1 > -1,\ \alpha_1 + \alpha_2 - \alpha_3 > 0 \\ \alpha_2 > 1,\ \alpha_3 \neq -1 \quad \text{or} \quad \alpha_3 < -1,\ \alpha_2 \neq 1 \end{cases} \tag{C.11}$$

The energy remains unchanged when parameters α_2 and α_3 are swapped and changed in sign. Thus, the case $\alpha_3 < -1,\ \alpha_2 \neq 1$ is equivalent to the case $\alpha_2 > 1,\ \alpha_3 \neq -1$ and describes the same behavior. Therefore we only consider the condition $\alpha_2 > 1,\ \alpha_3 \neq -1$. An infinite negative stress is necessary to reduce the volume to zero (criterion VI), namely

$$\lim_{J\to 0} \psi_c(J) = -\infty, \tag{C.12}$$

with ψ_c given by Eq. (C.5). The following conditions are necessary to fulfill the above equation:

$$\begin{cases} \alpha_1 > 0,\ \alpha_1 + \alpha_2 - \alpha_3 > 0 \\ \alpha_2 > 0 \quad \text{or} \quad \alpha_3 < 0 \end{cases} \tag{C.13}$$

Similarly to the energy, the hydrostatic stress remains unchanged when α_2 and α_3 are swapped and changed in sign. Hence, condition $\alpha_2 > 0$ is equivalent to condition $\alpha_3 < 0$, thus we limit to the case $\alpha_2 > 0$. In addition, from a mathematical standpoint when $\alpha_2 > 0$ parameter α_3 can assume any real value. However, if $\alpha_3 < 0$ the term $-J^{\alpha_3}$ behaves the same as $-J^{-\alpha_2}$ and goes to infinity when $J \to 0$. As explained in Section 5.3, we are instead interested in a term that contributes to the variation of stiffness in the region of small to moderate shrinkage, without affecting the response for large shrinkage. This behavior is obtained assuming $\alpha_3 > 0$, therefore we restrict our attention to this case. Considering the restrictions on both energy and stress, the overall constraints in shrinkage are

$$\alpha_1 > 0,\ \alpha_2 > 1,\ \alpha_3 > 0,\ \alpha_1 + \alpha_2 - \alpha_3 > 0. \tag{C.14}$$

An infinite energy is required to infinitely expand the volume of a solid (criterion VII), therefore

$$\lim_{J\to+\infty} \Psi_t(J) = +\infty, \tag{C.15}$$

with Ψ_t expressed by Eq. (C.3). Parameter q has the boundaries $0 \leq q \leq 1$. In addition, the functions involved with parameter β_3 are even, thus we consider only $\beta_3 > 0$. The above limit is satisfied if $\beta_1 > 0$ and $\beta_2 > 0$, or $\beta_1 < 0$ and $\beta_2 < 0$, or $\beta_1 < 0$ and $\beta_2 > 0$. When β_1 and β_2 have the same sign, function Ψ_t does not vary if they are both positive or negative. Thus, we discard the case in which $\beta_1 < 0$ and $\beta_2 < 0$. Criterion VIII states that an infinite positive stress is necessary to infinitely expand a volume, thus

$$\lim_{J\to+\infty} \psi_t(J) = +\infty, \tag{C.16}$$

with ψ_t expressed by Eq. (C.6). This limit is satisfied if $\beta_1 > 0$ and $\beta_2 > 0$.

Criterion IX imposes the condition of policonvexity of the volumetric part of the SED, namely the tangent modulus d^2W_h/dJ^2 must be positive in the entire domain. For $J > 1$, this is true if $\beta_1 > 0$ and $\beta_2 > 0$. For $J < 1$, the tangent modulus is always positive if $\alpha_1 + \alpha_2 - \alpha_3 > 0$. Finally, criterion X is guaranteed by the Heaviside step function (or its smooth approximation), which provides independent control of the responses in shrinkage and expansion.

In summary, the parameters of the proposed volumetric SED must satisfy the following constraints:

$$\begin{cases} \beta_1 > 0,\ \beta_2 > 0,\ \beta_3 > 0,\ 0 \leq q \leq 1 \\ \alpha_1 > 0,\ \alpha_2 > 1,\ \alpha_3 > 0,\ \alpha_1 + \alpha_2 - \alpha_3 > 0 \end{cases} \tag{C.17}$$

Bibliography

[1] L. R. G. Treloar. Strains in an inflated rubber sheet, and the mechanism of bursting. *Rubber Chemistry and Technology*, 17(4):957–967, 1944.

[2] J. E. Adkins and R. S. Rivlin. Large elastic deformations of isotropic materials ix. the deformation of thin shells. *Philosophical Transactions of the Royal Society of London. Series A, Mathematical and Physical Sciences*, 244(888):505–531, 1952.

[3] A. E. Green and J. E. Adkins. Large elastic deformations and non-linear continuum mechanics. *(No Title)*, 1960.

[4] A. H. Corneliussen and R. Shield. Finite deformation of elastic membranes with application to the stability of an inflated and extended tube. *Archive for Rational Mechanics and Analysis*, 7:273–304, 1961.

[5] O. Starkova and A. Aniskevich. Poisson's ratio and the incompressibility relation for various strain measures with the example of a silica-filled SBR rubber in uniaxial tension tests. *Polymer Testing*, 29(3):310–318, 2010.

[6] H. P. Kugler, R. G. Stacer, and C. Steimle. Direct measurement of Poisson's ratio in elastomers. *Rubber Chemistry and Technology*, 63(4):473–487, 1990.

[7] Z. Liu, W. Hong, Z. Suo, S. Swaddiwudhipong, and Y. Zhang. Modeling and simulation of buckling of polymeric membrane thin film gel. *Computational Materials Science*, 49(1):S60–S64, 2010.

[8] Z. Pientka, P. Pokorný, and K. Belafi-Bako. Closed-cell polymeric foam for hydrogen separation and storage. *Journal of Membrane Science*, 304(1-2):82–87, 2007.

[9] W. H. Yang and W. W. Feng. On axisymmetrical deformations of nonlinear membranes. *Journal of Applied Mechanics*, 37(4):1002–1011, 1970.

[10] B. Gorissen, E. Milana, A. Baeyens, E. Broeders, J. Christiaens, K. Collin, D. Reynaerts, and M. De Volder. Hardware sequencing of inflatable nonlinear actuators for autonomous soft robots. *Advanced Materials*, 31(3):1804598, 2019.

[11] L. Chen, W. Chen, Y. Xue, M. Zhang, X. Chen, X. Cao, Z. Zhang, G. Li, and T. Li. Investigation of the state transition and moving boundary in a pneumatic–hydraulic coupled dielectric elastomer actuator. *Journal of Applied Mechanics*, 86(3):031004, 2019.

[12] J. Walker, T. Zidek, C. Harbel, S. Yoon, F. S. Strickland, S. Kumar, and M. Shin. Soft robotics: a review of recent developments of pneumatic soft actuators. In *Actuators*, volume 9, page 3. Multidisciplinary Digital Publishing Institute, 2020.

[13] N. Goulbourne, E. Mockensturm, and M. Frecker. A nonlinear model for dielectric elastomer membranes. *Journal of Applied Mechanics*, 72(6):899–906, 2005.

[14] J. W. Fox and N. C. Goulbourne. On the dynamic electromechanical loading of dielectric elastomer membranes. *Journal of the Mechanics and Physics of Solids*, 56(8):2669–2686, 2008.

[15] H. Wang. Viscoelastic analysis of a spring-connected dielectric elastomer actuator undergoing large inhomogeneous deformation. *International Journal of Mechanical Sciences*, 136:17–23, 2018.

[16] T. Hiruta, N. Hosoya, S. Maeda, and I. Kajiwara. Experimental validation of vibration control in membrane structures using dielectric elastomer actuators in a vacuum environment. *International Journal of Mechanical Sciences*, 191:106049, 2021.

[17] Y.-X. Xie, J.-C. Liu, and Y. Fu. Bifurcation of a dielectric elastomer balloon under pressurized inflation and electric actuation. *International Journal of Solids and Structures*, 78:182–188, 2016.

[18] W. Cheng, M. J. Campolongo, S. J. Tan, and D. Luo. Freestanding ultrathin nano-membranes via self-assembly. *Nano Today*, 4(6):482–493, 2009.

[19] A. Pacheco-Sanjuán and R. Batra. Accuracy of föppl–von karman membrane theory for determining elastic constants of monolayer graphene. *International Journal of Mechanical Sciences*, 163:105154, 2019.

[20] A. Wineman, D. Wilson, and J. W. Melvin. Material identification of soft tissue using membrane inflation. *Journal of Biomechanics*, 12(11):841–850, 1979.

[21] E. R. Serina, E. Mockensturm, C. D. Mote Jr, and D. Rempel. A structural model of the forced compression of the fingertip pulp. *Journal of Biomechanics*, 31(7):639–646, 1998.

[22] M. Gil Pérez, T. H.-K. Kang, I. Sin, and S. D. Kim. Nonlinear analysis and design of membrane fabric structures: Modeling procedure and case studies. *Journal of Structural Engineering*, 142(11):05016001, 2016.

[23] R. Glaser. Multi-objective characterization of an inflatable space structure with a quasi-static experimental deflation and finite element analysis. *International Journal of Mechanical Sciences*, 205:106614, 2021.

[24] R. Courant and D. Hilbert. Methods of mathematical physics (interscience publ., new york and london), vol. 1. *vol*, 2:830, 1962.

[25] M. X. Liu, C. G. Wang, and X. D. Li. Rigid-flexible contact analysis of an inflated membrane balloon with various contact conditions. *International Journal of Solids and Structures*, 144:218–229, 2018.

[26] A. Patil, A. DasGupta, and A. Eriksson. Contact mechanics of a circular membrane inflated against a deformable substrate. *International Journal of Solids and Structures*, 67:250–262, 2015.

[27] K. Upadhyay, G. Subhash, and D. Spearot. Thermodynamics-based stability criteria for constitutive equations of isotropic hyperelastic solids. *Journal of the Mechanics and Physics of Solids*, 124:115–142, 2019.

[28] M. Sasso, G. Palmieri, G. Chiappini, and D. Amodio. Characterization of hyperelastic rubber-like materials by biaxial and uniaxial stretching tests based on optical methods. *Polymer Testing*, 27(8):995–1004, 2008.

[29] N. Kumar and V. V. Rao. Hyperelastic Mooney-Rivlin model: Determination and physical interpretation of material constants. *Parameters*, 2(10):01, 2016.

[30] R. Rivlin and A. G. Thomas. Rupture of rubber. i. characteristic energy for tearing. *Journal of polymer science*, 10(3):291–318, 1953.

[31] R. S. Rivlin and D. Saunders. Large elastic deformations of isotropic materials vii. experiments on the deformation of rubber. *Philosophical Transactions of the Royal Society of London. Series A, Mathematical and Physical Sciences*, 243(865):251–288, 1951.

[32] L. Lanzoni and A. M. Tarantino. A simple nonlinear model to simulate the localized necking and neck propagation. *International Journal of Non-Linear Mechanics*, 84:94–104, 2016.

[33] A. M. Tarantino. Thin hyperelastic sheets of compressible material: field equations, airy stress function and an application in fracture mechanics. *Journal of elasticity*, 44(1):37–59, 1996.

[34] A. M. Tarantino. Crack propagation in finite elastodynamics. *Mathematics and Mechanics of Solids*, 10(6):577–601, 2005.

[35] A. M. Tarantino and A. Nobili. Finite homogeneous deformations of symmetrically loaded compressible membranes. *Zeitschrift für angewandte Mathematik und Physik*, 58:659–678, 2007.

[36] P. G. Ciarlet and G. Geymonat. Sur les lois de comportement en élasticité non linéaire compressible. *CR Acad Sci Paris Sér II*, 295:423–426, 1982.

[37] M. H. Sadd. *Continuum Mechanics Modeling of Material Behavior*. Academic Press, 2018.

[38] M. Pelliciari and A. M. Tarantino. Equilibrium and stability of anisotropic hyperelastic graphene membranes. *Journal of Elasticity*, 144:169–195, 2021.

[39] M. Pelliciari, S. Sirotti, A. Aloisio, and A. M. Tarantino. Analytical, numerical and experimental study of the finite inflation of circular membranes. *International Journal of Mechanical Sciences*, 226:107383, 2022.

[40] A. P. S. Selvadurai. Deflections of a rubber membrane. *Journal of the Mechanics and Physics of Solids*, 54(6):1093–1119, 2006.

[41] G. Marckmann and E. Verron. Comparison of hyperelastic models for rubber-like materials. *Rubber chemistry and technology*, 79(5):835–858, 2006.

[42] R. M. Soares and P. B. Gonçalves. Large-amplitude nonlinear vibrations of a Mooney–Rivlin rectangular membrane. *Journal of Sound and Vibration*, 333(13):2920–2935, 2014.

[43] T. Gopesh and J. Friend. Facile analytical extraction of the hyperelastic constants for the two-parameter Mooney–Rivlin model from experiments on soft polymers. *Soft Robotics*, 8(4):365–370, 2021.

[44] V. P. W. Shim, L. M. Yang, C. T. Lim, and P. H. Law. A visco-hyperelastic constitutive model to characterize both tensile and compressive behavior of rubber. *Journal of Applied Polymer Science*, 92(1):523–531, 2004.

[45] M. Pelliciari and A. M. Tarantino. A nonlinear molecular mechanics model for graphene subjected to large in-plane deformations. *International Journal of Engineering Science*, 167:103527, 2021.

[46] L. Lanzoni and A. M. Tarantino. Finite anticlastic bending of hyperelastic solids and beams. *Journal of Elasticity*, 131(2):137–170, 2018.

[47] M. Pelliciari and A. M. Tarantino. Equilibrium paths for von mises trusses in finite elasticity. *Journal of Elasticity*, 138(2):145–168, 2020.

[48] J. Yuan, X. Liu, H. Xia, and Y. Huang. Analytical solutions for inflation of pre-stretched elastomeric circular membranes under uniform pressure. *Theoretical and Applied Mechanics Letters*, page 100243, 2021.

[49] X. Yang, L. Yu, and R. Long. Contact mechanics of inflated circular membrane under large deformation: Analytical solutions. *International Journal of Solids and Structures*, 233:111222, 2021.

[50] H. O. Foster. Very large deformations of axially symmetrical membranes made of neo-Hookean materials. *International Journal of Engineering Science*, 5(1):95–117, 1967.

[51] W. B. Fichter. *Some solutions for the large deflections of uniformly loaded circular membranes*, volume 3658. National Aeronautics and Space Administration, Langley Research Center, 1997.

[52] D. Pamplona and D. Mota. Numerical and experimental analysis of inflating a circular hyperelastic membrane over a rigid and elastic foundation. *International Journal of Mechanical Sciences*, 65(1):18–23, 2012.

[53] F. Jourdan, J. Vasquez-Villegas, R. A. R. E. Anwar, S. Le Floc'h, and C. Wagner-Kocher. Semi-analytical model for stretch ratio determination in inflation test for isotropic membranes. *Mechanics Research Communications*, 127:104033, 2023.

[54] G. Machado, D. Favier, and G. Chagnon. Membrane curvatures and stress-strain full fields of axisymmetric bulge tests from 3d-dic measurements. theory and validation on virtual and experimental results. *Experimental mechanics*, 52:865–880, 2012.

[55] K. Suleman and F. Bosi. Finite strain elastoplastic bulging of circular diaphragms. *International Journal of Solids and Structures*, 267:112148, 2023.

[56] D. Steck, J. Qu, S. B. Kordmahale, D. Tscharnuter, A. Muliana, and J. Kameoka. Mechanical responses of Ecoflex silicone rubber: Compressible and incompressible behaviors. *Journal of Applied Polymer Science*, 136(5):47025, 2019.

[57] M. Pelliciari, S. Sirotti, and A. M. Tarantino. A strain energy function for large deformations of compressible elastomers. *Journal of the Mechanics and Physics of Solids*, 176:105308, 2023.

[58] R. W. Ogden. Large deformation isotropic elasticity–on the correlation of theory and experiment for incompressible rubberlike solids. *Proceedings of the Royal Society of London. A. Mathematical and Physical Sciences*, 326(1567):565–584, 1972.

[59] O. H. Yeoh. Characterization of elastic properties of carbon-black-filled rubber vulcanizates. *Rubber Chemistry and Technology*, 63(5):792–805, 1990.

[60] A. N. Gent. A new constitutive relation for rubber. *Rubber Chemistry and Technology*, 69(1):59–61, 1996.

[61] O. H. Yeoh and P. D. Fleming. A new attempt to reconcile the statistical and phenomenological theories of rubber elasticity. *Journal of Polymer Science Part B: Polymer Physics*, 35(12):1919–1931, 1997.

[62] H. Vaughan. Pressurising a prestretched membrane to form a paraboloid. *International Journal of Engineering Science*, 18(1):99–107, 1980.

[63] S. Akbari and H. R. Shea. An array of 100 μm$\times$ 100 μm dielectric elastomer actuators with 80% strain for tissue engineering applications. *Sensors and Actuators A: Physical*, 186:236–241, 2012.

[64] A. Saini, D. Ahmad, and K. Patra. Electromechanical performance analysis of inflated dielectric elastomer membrane for micro pump applications. In *Electroactive Polymer Actuators and Devices (EAPAD) 2016*, volume 9798, pages 180–186. SPIE, 2016.

[65] J. Charrier, S. Shrivastava, and R. Wu. Free and constrained inflation of elastic membranes in relation to thermoforming—axisymmetric problems. *The Journal of Strain Analysis for Engineering Design*, 22(2):115–125, 1987.

[66] Y. Guo, L. Liu, Y. Liu, and J. Leng. Review of dielectric elastomer actuators and their applications in soft robots. *Advanced Intelligent Systems*, 3(10):2000282, 2021.

[67] S. Sirotti, M. Pelliciari, A. Aloisio, and A. M. Tarantino. Analytical pressure–deflection curves for the inflation of pre-stretched circular membranes. *European Journal of Mechanics-A/Solids*, 97:104831, 2023.

[68] M. Amabili, P. Balasubramanian, I. D. Breslavsky, G. Ferrari, R. Garziera, and K. Riabova. Experimental and numerical study on vibrations and static deflection of a thin hyperelastic plate. *Journal of sound and vibration*, 385:81–92, 2016.

[69] J. Fox and N. Goulbourne. Electric field-induced surface transformations and experimental dynamic characteristics of dielectric elastomer membranes. *Journal of the Mechanics and Physics of Solids*, 57(8):1417–1435, 2009.

[70] R. W. Warfield, J. E. Cuevas, and F. R. Barnet. Single specimen determination of Young's and bulk moduli of polymers. *Rheologica Acta*, 9:439–446, 1970.

[71] M. C. Boyce and E. M. Arruda. Constitutive models of rubber elasticity: a review. *Rubber Chemistry and Technology*, 73(3):504–523, 2000.

[72] P. H. Mott, J. R. Dorgan, and C. M. Roland. The bulk modulus and Poisson's ratio of "incompressible" materials. *Journal of Sound and Vibration*, 312(4-5):572–575, 2008.

[73] H. Khajehsaeid, J. Arghavani, and R. Naghdabadi. A hyperelastic constitutive model for rubber-like materials. *European Journal of Mechanics-A/Solids*, 38:144–151, 2013.

[74] C. O. Horgan. The remarkable Gent constitutive model for hyperelastic materials. *International Journal of Non-Linear Mechanics*, 68:9–16, 2015.

[75] Y. Zhang, K. Yu, K. H. Lee, K. Li, H. Du, and Q. Wang. Mechanics of stretchy elastomer lattices. *Journal of the Mechanics and Physics of Solids*, 159:104782, 2022.

[76] F. Armero. On the locking and stability of finite elements in finite deformation plane strain problems. *Computers & Structures*, 75(3):261–290, 2000.

[77] U. Heisserer, S. Hartmann, A. Düster, and Z. Yosibash. On volumetric locking-free behaviour of p-version finite elements under finite deformations. *Communications in Numerical Methods in Engineering*, 24(11):1019–1032, 2008.

[78] P. J. Blatz and W. L. Ko. Application of finite elastic theory to the deformation of rubbery materials. *Transactions of the Society of Rheology*, 6(1):223–252, 1962.

[79] M. Levinson and I. W. Burgess. A comparison of some simple constitutive relations for slightly compressible rubber-like materials. *International Journal of Mechanical Sciences*, 13(6):563–572, 1971.

[80] J. E. Bischoff, E. M. Arruda, and K. Grosh. A new constitutive model for the compressibility of elastomers at finite deformations. *Rubber Chemistry and Technology*, 74(4):541–559, 2001.

[81] C. O. Horgan and G. Saccomandi. Constitutive models for compressible nonlinearly elastic materials with limiting chain extensibility. *Journal of Elasticity*, 77:123–138, 2004.

[82] X. Peng, L. Han, and L. Li. A consistently compressible Mooney-Rivlin model for the vulcanized rubber based on the Penn's experimental data. *Polymer Engineering & Science*, 61(9):2287–2294, 2021.

[83] T. H. Lengyel, Y. Qi, P. Schiavone, and R. Long. Interface crack between a compressible elastomer and a rigid substrate with finite slippage. *Journal of the Mechanics and Physics of Solids*, 90:142–159, 2016.

[84] J. Li, D. Mayau, and V. Lagarrigue. A constitutive model dealing with damage due to cavity growth and the Mullins effect in rubber-like materials under triaxial loading. *Journal of the Mechanics and Physics of Solids*, 56(3):953–973, 2008.

[85] C. M. Landis, R. Huang, and J. W. Hutchinson. Formation of surface wrinkles and creases in constrained dielectric elastomers subject to electromechanical loading. *Journal of the Mechanics and Physics of Solids*, 167:105023, 2022.

[86] P. Angeli, G. Russo, and A. Paschini. Carbon fiber-reinforced rectangular isolators with compressible elastomer: Analytical solution for compression and bending. *International Journal of Solids and Structures*, 50(22-23):3519–3527, 2013.

[87] C. Sansour. On the physical assumptions underlying the volumetric-isochoric split and the case of anisotropy. *European Journal of Mechanics-A/Solids*, 27(1):28–39, 2008.

[88] K. M. Moerman, B. Fereidoonnezhad, and J. P. McGarry. Novel hyperelastic models for large volumetric deformations. *International Journal of Solids and Structures*, 193:474–491, 2020.

[89] R. W. Ogden, G. Saccomandi, and I. Sgura. Fitting hyperelastic models to experimental data. *Computational Mechanics*, 34:484–502, 2004.

[90] P. Steinmann, M. Hossain, and G. Possart. Hyperelastic models for rubber-like materials: consistent tangent operators and suitability for Treloar's data. *Archive of Applied Mechanics*, 82:1183–1217, 2012.

[91] M. Destrade, G. Saccomandi, and I. Sgura. Methodical fitting for mathematical models of rubber-like materials. *Proceedings of the Royal Society A: Mathematical, Physical and Engineering Sciences*, 473(2198):20160811, 2017.

[92] L. A. Mihai and A. Goriely. How to characterize a nonlinear elastic material? A review on nonlinear constitutive parameters in isotropic finite elasticity. *Proceedings of the Royal Society A: Mathematical, Physical and Engineering Sciences*, 473(2207):20170607, 2017.

[93] V. Singh and V. Racherla. Deformation behavior of fluid-filled porous elastomers: Analytical estimates and validation. *Journal of the Mechanics and Physics of Solids*, 163:104835, 2022.

[94] Y. Zhou, Y. Chen, and L. Jin. Three-dimensional postbuckling analysis of thick hyperelastic tubes. *Journal of the Mechanics and Physics of Solids*, page 105202, 2023.

[95] L. H. Adams and R. E. Gibson. The compressibility of rubber. *Rubber Chemistry and Technology*, 3(4):555–562, 1930.

[96] P. W. Bridgman. The compression of sixty-one solid substances to 25,000 kg/cm^2, determined by a new rapid method. In *Proc. Am. Acad. Arts Sci*, volume 76, page 24, 1945.

[97] J. Blaber, B. Adair, and A. Antoniou. Ncorr: open-source 2D digital image correlation matlab software. *Experimental Mechanics*, 55(6):1105–1122, 2015.

[98] Q. Zheng, N. Mashiwa, and T. Furushima. Evaluation of large plastic deformation for metals by a non-contacting technique using digital image correlation with laser speckles. *Materials & Design*, 191:108626, 2020.

[99] M. R. Gurvich and T. S. Fleischman. A simple approach to characterize finite compressibility of elastomers. *Rubber Chemistry and Technology*, 76(4):912–922, 2003.

[100] B. Omnès, S. Thuillier, P. Pilvin, Y. Grohens, and S. Gillet. Effective properties of carbon black filled natural rubber: Experiments and modeling. *Composites Part A: Applied Science and Manufacturing*, 39(7):1141–1149, 2008.

[101] S. Doll and K. Schweizerhof. On the development of volumetric strain energy functions. *Journal of Applied Mechanics*, 67(1):17–21, 2000.

[102] R. W. Ogden. *Non-linear elastic deformations*. Courier Corporation, 1997.

[103] H. Hencky. The elastic behavior of vulcanized rubber. *Rubber Chemistry and Technology*, 6(2):217–224, 1933.

[104] J. C. Simo. A framework for finite strain elastoplasticity based on maximum plastic dissipation and the multiplicative decomposition: Part I. Continuum formulation. *Computer Methods in Applied Mechanics and Engineering*, 66(2):199–219, 1988.

[105] G. Montella, S. Govindjee, and P. Neff. The exponentiated Hencky strain energy in modeling tire derived material for moderately large deformations. *Journal of Engineering Materials and Technology*, 138(3):031008, 2016.

[106] P. Neff, J. Lankeit, I. D. Ghiba, R. Martin, and D. Steigmann. The exponentiated Hencky-logarithmic strain energy. Part II: coercivity, planar polyconvexity and existence of minimizers. *Zeitschrift für angewandte Mathematik und Physik*, 66:1671–1693, 2015.

[107] R. Hill. Aspects of invariance in solid mechanics. *Advances in Applied Mechanics*, 18:1–75, 1979.

[108] C. O. Horgan and J. G. Murphy. On the volumetric part of strain-energy functions used in the constitutive modeling of slightly compressible solid rubbers. *International Journal of Solids and Structures*, 46(16):3078–3085, 2009.

[109] E. Bardy, J. Mollendorf, and D. Pendergast. Thermal conductivity and compressive strain of foam neoprene insulation under hydrostatic pressure. *Journal of Physics D: Applied Physics*, 38(20):3832, 2005.

[110] M. T. Petre, A. Erdemir, and P. R. Cavanagh. Determination of elastomeric foam parameters for simulations of complex loading. *Computer Methods in Biomechanics and Biomedical Engineering*, 9(4):231–242, 2006.

[111] Y. J. Liang, J. S. McQuien, and E. V. Iarve. Implementation of the regularized extended finite element method in Abaqus framework for fracture modeling in laminated composites. *Engineering Fracture Mechanics*, 230:106989, 2020.

[112] A. Iliev, N. Kyurkchiev, and S. Markov. On the approximation of the step function by some sigmoid functions. *Mathematics and Computers in Simulation*, 133:223–234, 2017.

[113] S. V. Alyukov. Approximation of step functions in problems of mathematical modeling. *Mathematical Models and Computer Simulations*, 3:661–669, 2011.

[114] S. Markov, N. Kyurkchiev, A. Iliev, and A. Rahnev. On the approximation of the generalized cut functions of degree p+1 by smooth hyper-log-logistic function. *Dynamic Systems and Applications*, 27(4):715–728, 2018.

[115] R. S. Rivlin and D. W. Saunders. *Large elastic deformations of isotropic materials: VII. Experiments on the deformation of rubber*. Springer, 1997.

[116] L. Treloar. The elasticity of a network of long-chain molecules–II. *Transactions of the Faraday Society*, 39:241–246, 1943.

[117] R. S. Rivlin. Large elastic deformations of isotropic materials IV. Further developments of the general theory. *Philosophical Transactions of the Royal Society of London. Series A, Mathematical and Physical Sciences*, 241(835):379–397, 1948.

[118] E. Pucci and G. Saccomandi. A note on the Gent model for rubber-like materials. *Rubber Chemistry and Technology*, 75(5):839–852, 2002.

[119] M. M. Carroll. A strain energy function for vulcanized rubbers. *Journal of Elasticity*, 103:173–187, 2011.

[120] H. Dal, K. Açıkgöz, and Y. Badienia. On the performance of isotropic hyperelastic constitutive models for rubber-like materials: A state of the art review. *Applied Mechanics Reviews*, 73(2), 2021.

[121] S. Madireddy, B. Sista, and K. Vemaganti. A bayesian approach to selecting hyperelastic constitutive models of soft tissue. *Computer Methods in Applied Mechanics and Engineering*, 291:102–122, 2015.

[122] G. Puglisi and G. Saccomandi. Multi-scale modelling of rubber-like materials and soft tissues: an appraisal. *Proceedings of the Royal Society A: Mathematical, Physical and Engineering Sciences*, 472(2187):20160060, 2016.

[123] W. Hong, X. Zhao, J. Zhou, and Z. Suo. A theory of coupled diffusion and large deformation in polymeric gels. *Journal of the Mechanics and Physics of Solids*, 56(5):1779–1793, 2008.

[124] Z. Ding, Z. Liu, J. Hu, S. Swaddiwudhipong, and Z. Yang. Inhomogeneous large deformation study of temperature-sensitive hydrogel. *International Journal of Solids and Structures*, 50(16-17):2610–2619, 2013.

[125] M. Ahearne, Y. Yang, A. J. El Haj, K. Y. Then, and K. K. Liu. Characterizing the viscoelastic properties of thin hydrogel-based constructs for tissue engineering applications. *Journal of the Royal Society Interface*, 2(5):455–463, 2005.

[126] M. Rampf, O. Speck, T. Speck, and R. H. Luchsinger. Self-repairing membranes for inflatable structures inspired by a rapid wound sealing process of climbing plants. *Journal of Bionic Engineering*, 8(3):242–250, 2011.

[127] E. Elele, Y. Shen, J. Tang, Q. Lei, B. Khusid, G. Tkacik, and C. Carbrello. Mechanical properties of polymeric microfiltration membranes. *Journal of membrane science*, 591:117351, 2019.

[128] N. Firouzi and K. K. Żur. On the generalized nonlinear mechanics of compressible, incompressible, isotropic, and anisotropic hyperelastic membranes. *International Journal of Solids and Structures*, 264:112088, 2023.

[129] D. T. Chung, C. O. Horgan, and R. Abeyaratne. The finite deformation of internally pressurized hollow cylinders and spheres for a class of compressible elastic materials. *International Journal of Solids and Structures*, 22(12):1557–1570, 1986.

[130] A. P. S. Selvadurai and A. P. Suvorov. On the inflation of poro-hyperelastic annuli. *Journal of the Mechanics and Physics of Solids*, 107:229–252, 2017.

[131] K. Urayama, T. Takigawa, and T. Masuda. Poisson's ratio of poly (vinyl alcohol) gels. *Macromolecules*, 26(12):3092–3096, 1993.

[132] J. B. Choi and R. S. Lakes. Non-linear properties of polymer cellular materials with a negative poisson's ratio. *Journal of Materials Science*, 27:4678–4684, 1992.

[133] Y. Fu, S. Pearce, and K. K. Liu. Post-bifurcation analysis of a thin-walled hyperelastic tube under inflation. *International Journal of Non-Linear Mechanics*, 43(8):697–706, 2008.

[134] D. Haughton. Elastic membranes. *London Mathematical Society Lecture Note Series*, pages 233–267, 2001.

[135] A. C. Pipkin. Integration of an equation in membrane theory. *Zeitschrift für angewandte Mathematik und Physik ZAMP*, 19:818–819, 1968.

[136] A. Anssari-Benam, A. Bucchi, and G. Saccomandi. Modelling the inflation and elastic instabilities of rubber-like spherical and cylindrical shells using a new generalised neo-Hookean strain energy function. *Journal of Elasticity*, 151(1):15–45, 2022.

[137] D. Haughton and R. Ogden. On the incremental equations in non-linear elasticity – II. Bifurcation of pressurized spherical shells. *Journal of the Mechanics and Physics of Solids*, 26(2):111–138, 1978.

[138] L. Lanzoni and A. M. Tarantino. Equilibrium configurations and stability of a damaged body under uniaxial tractions. *Zeitschrift für angewandte Mathematik und Physik*, 66(1):171–190, 2015.

[139] P. G. Ciarlet. *Mathematical elasticity: Three-dimensional elasticity, vol. I.* North-Holland Publishing Co., Amsterdam, 1988.

[140] C. O. Horgan and J. G. Murphy. Simple shearing of incompressible and slightly compressible isotropic nonlinearly elastic materials. *Journal of Elasticity*, 98:205–221, 2010.

[141] L. A. Wood and G. M. Martin. Compressibility of natural rubber at pressures below 500 kg/cm^2. *Journal of Research of the National Bureau of Standards. Section A, Physics and Chemistry*, 68(3):259, 1964.

[142] C. O. Horgan and J. G. Murphy. Constitutive modeling for moderate deformations of slightly compressible rubber. *Journal of Rheology*, 53(1):153–168, 2009.